M. Reich

A new diagnostic for edge ion temperatures at ASDEX Upgrade with lithium-beam charge exchange recombination spectroscopy

A new diagnostic for ASDEX Upgrade edge ion temperatures by lithium-beam charge exchange recombination spectroscopy

Der Fakultät für Physik
der Ludwig-Maximilians-Universität München
zur Erlangung des akademischen Grades eines
Doktors der Naturwissenschaften (Dr. rer. nat.)
vorgelegte Dissertation

von

Dipl. Phys. Matthias Reich

aus Hirschau

22. Dezember 2004

Erstgutachter: Prof. Dr. Hartmut Zohm

Zweitgutachter: Prof. Dr. Harald Lesch

Tag der mündlichen Prüfung: 18.3.2005

Für Silke

Diese Dissertation behandelt die Messung von Ionentemperaturen am Rand eines magnetisch eingeschlossenen Fusionsplasmas am Tokamak „ASDEX Upgrade", betrieben vom Max-Planck-Institut für Plasmaphysik in Garching.

Das am weitesten fortgeschrittene Konzept des toroidalen Magnetfeldeinschlusses ist der Tokamak. Das „H-Mode"-Plasmaregime, Standardszenario des geplanten Großexperiments ITER, ist charakterisiert durch eine Randtransportbarriere, die noch nicht vollständig von der Theorie erklärt werden kann. Experimentell gemessene Ionentemperaturprofile am Plasmarand helfen dabei, Modelle für diese Barrieren zu testen und neu zu entwickeln. In der Arbeit wird die Theorie des Plasmatransports als theoretischer Hintergrund und für die Motivation der Notwendigkeit der neuen Diagnostik diskutiert. In diesem Zusammenhang wird auch das Standardmodell einer Instabilität des Plasmarandes, genannt „edge localized mode" (ELM), die in der H-Mode beobachtet wird, kurz beschrieben.

Der Kern der Arbeit behandelt die Implementierung einer neuen Diagnostik für Ionentemperaturmessungen mit hoher räumlicher Auflösung am Plasmarand, die Inbetriebnahme derselben und die Validierung der ermittelten Messdaten. Die Linienstrahlung, die nach Ladungsaustauschprozessen zwischen schnellen Lithiumatomen und vollständig ionisierten Verunreinigungsionen (C^{6+}, He^{2+}) entsteht, wird mit einem Detektorsystem aus Spektrometern und schnellen CCD-Kameras beobachtet. Aufgrund des schmalen Lithiumstrahls (1 cm) und der eng gestaffelten Lichtleiteranordnung für die Beobachtung (6 mm) wurde eine bisher nicht erreichte räumliche Auflösung für Ionentemperaturmessungen in allen Standardplasmen des Tokamaks „ASDEX Upgrade" erzielt. Die spektrale Breite der Linienstrahlung (He II bei 468.5 nm und C VI bei 529.0 nm) enthält Informationen über die lokale Ionentemperatur aus der thermischen Dopplerverbreiterung, welche der dominierende Mechanismus für die Linienverbreiterung ist. Der Beitrag zur Linienstrahlung, der aus lokalem Ladungsaustausch mit Lithium hervorgeht, wird mit Hilfe von Ablenkplatten, die den Strahl ein- und ausschalten, durch die Differenz aus Gesamtintensität und Hintergrund ermittelt. Durch Anpassen einer Gaußschen Modellfunktion an die so ermittelte lokale Linienstrahlung, kann die Linienbreite gemessen und direkt in eine Temperatur umgerechnet werden. Die Verunreinigungen, an denen gemessen wird, gleichen ihre Temperatur schnell genug an das Hauptplasma an, so dass lokal identische Temperaturen für alle Ionensorten angenommen werden können. Systematische Fehler durch nicht-thermische Verbreiterungseffekte (Zeeman-Verbreiterung und stoßinduziertes Mischen des Augangszustands) werden durch Modellrechnungen für die beteiligten atomaren Prozesse berücksichtigt. Die Zeitauflösung der Diagnostik ist nicht ausreichend, um ELM-Instabilitäten zeitlich aufzulösen. Die Messung zwischen ELMs ist jedoch möglich, wenn die ELM-Frequenz niedrig genug ist.

L-Mode Plasmen mit und ohne Zusatzheizung können zuverlässig diagnostiziert werden. Die Zeitauflösung hängt von der Strahlintensität und der Plasmadichte ab und kann bei optimalen Bedingungen bis zu 100 ms betragen. Es wurde gezeigt, dass durch Zugabe

von Helium in geringen Mengen das Signal-zu-Rausch Verhältnis verbessert werden kann. Ergebnisse aus L-Mode Plasmen mit Elektronenheizung zeigen, dass sich Ionentemperaturen am Rand erheblich von den Elektronentemperaturen unterscheiden können. Für die Validierung der neuen Messungen wurden Vergleiche mit Daten bereits in Betrieb befindlicher Diagnostiken vorgenommen. Messungen in neutralstrahl-geheizten L-Mode und H-Mode Plasmen stimmen mit den Messwerten einer ähnlichen Diagnostik, die die Heizstrahlen für den Ladungsaustausch benutzt, im Bereich, in dem sich beide Diagnostiken überlappen, überein. Sie können daher kombiniert werden, um ein komplettes Ionentemperaturprofil über den gesamten Plasmaradius zu erhalten. Als eine erste Anwendung wurden mit Hilfe von Modellrechnungen Randtransportkoeffizienten für ein ohmsches Plasma ermittelt.

Am Tokamak ASDEX Upgrade wurde eine neue Diagnostik zur Messung von Ionentemperaturen am Rand von magnetisch eingeschlossenen Fusionsplasmen in Betrieb genommen. Die Ergebnisse tragen wesentlich zum besseren Verständnis von Transportvorgängen im Plasma bei.

This thesis work investigates the measurement of ion temperatures at the edge of a magnetically confined plasma used for fusion research at the ASDEX Upgrade tokamak operated by Max-Planck-Institut für Plasmaphysik in Garching.

The tokamak is the most advanced concept in toroidal magnetic confinement fusion. The H-mode plasma regime, default scenario of the next step experiment ITER, is characterized by an edge transport barrier, which is not yet fully explained by theory. Experimentally measured edge ion temperature profiles will help to test and develop models for these barriers. Transport theory on a basic level is introduced as background and motivation for the new diagnostic. The standard model for an edge plasma instability named "edge localized mode" (ELM) observed in H-mode is described.

The implementation of a new diagnostic for ion temperature measurements with high spatial resolution in the plasma edge region, its commissioning and the validation of the measurements comprises the main part of this work. The emission of line radiation induced by charge exchange processes between lithium atoms injected by a beam source and fully ionized impurities (C^{6+}, He^{2+}) is observed with a detection system consisting of spectrometers and fast cameras. Due to the narrow beam (1 cm) and closely staggered optical fibers (6 mm), unprecedented spatial resolution of edge ion temperatures in all major plasma regimes of the ASDEX Upgrade tokamak was achieved. The spectral width of the line radiation (He II at 468.5 nm and C VI at 529.0 nm) contains information about the local ion temperature from thermal Doppler-broadening, which is the dominant broadening mechanism for these lines. The charge-exchange contribution to the total line radiation locally generated by the lithium is determined by gating the beam. Fitting a Gaussian model function to the local line radiation results in absolute line widths which can be directly converted into a temperature. The equilibration of impurities with the main plasma is fast enough that the assumption of nearly identical temperatures as the main plasma is justified. Corrections for systematic line broadening effects from collisional mixing and Zeeman broadening are incorporated by model calculations using existing routines for the involved atomic physics. Time resolution of the diagnostic is still not sufficient to resolve ELM events, but measuring between ELMs is possible if their frequency is low.

L-mode plasmas with and without additional heating can be reliably diagnosed with a time resolution depending on the lithium beam intensity and plasma density, in best cases down to 100 ms. It was shown that diagnostic He puffing can be used to enhance the signal-to-noise ratio. Results from L-mode plasmas with electron heating show that ion temperatures can be significantly different from electron temperatures at the edge. For the verification of the new ion temperatures, comparison with data from already established diagnostics was done. In neutral beam heated L-mode and various H-mode plasmas the ion temperatures agree with those from a similar diagnostic measuring in the core using heating beams where both diagnostics overlap. They can be combined to form a complete ion temperature profile over the whole plasma radius. In a first application, transport coefficients have been determined by interpretative modeling for an ohmic plasma.

In summary, a new method for measuring ion temperatures in the edge of a magnetically confined fusion plasma has been established. The results provide an important input to further understanding of transport in these plasmas.

Parts of this dissertation were published in:

M. Reich, E. Wolfrum, J. Schweinzer, H. Ehmler, L. D. Horton, J. Neuhauser, ASDEX Upgrade Team, (2004), *Lithium Beam Charge Exchange Diagnostic for Edge Ion Temperature Measurements at the ASDEX Upgrade Tokamak*, Plasma Physics and Controlled Fusion 46(5), 797-808.

M. Reich, E. Wolfrum, L. D. Horton, J. Schweinzer, J. Neuhauser, ASDEX Upgrade Team, (2004) *Edge Ion Temperature Measurements at ASDEX Upgrade*, in: Europhysics Conference Abstracts (CD-ROM, Proc. of the 31st EPS Conference on Plasma Physics, London, 2004), (Ed.) Pick, A. M. (EPS, Geneva), Vol. 28G, P-4.118.

G. D. Conway, B. Scott, J. Schirmer, M. Reich, A. Kendl, ASDEX Upgrade Team, (2004) *Direct Measurement of Zonal Flows and Geodesic Acoustic Mode (GAM) Oscillations in ASDEX Upgrade Using Doppler Reflectometry*, in: Europhysics Conference Abstracts (CD-ROM, Proc. of the 31st EPS Conference on Plasma Physics, London, 2004), (Ed.) Pick, A. M. (EPS, Geneva), Vol. 28G, P-4.124.

L. D. Horton, A. V. Chankin, Y. P. Chen, G. D. Conway, D. P. Coster, T. Eich, B. Kurzan, J. Neuhauser, I. Nunes, M. Reich, S. Saarelma, J. Schirmer, J. Schweinzer, E. Wolfrum, ASDEX Upgrade Team, (2005), *Characterisation of the H-mode Edge Barrier at ASDEX Upgrade*, in: Proc. of the 20th IAEA Conference Fusion Energy (CD-Rom), Vilamoura, Portugal, November 2004 (IAEA, Vienna), Vol. 0, IAEA-CN-116/EX/P3-4.

W. Suttrop, M. Maraschek, G. D. Conway, H.-U. Fahrbach, L. Fattorini, G. Haas, L. D. Horton, S. Klose, T. Kurki-Suonio, C. F. Maggi, P. J. McCarthy, H. Meister, A. Mück, R. Neu, I. Nunes, Th. Pütterich, M. Reich, A. C. C. Sips, ASDEX Upgrade Team, (2003), *ELM-free Stationary H-mode Plasmas in ASDEX Upgrade*, in: Europhysics Conference Abstracts (CD-ROM, Proc. of the 30th EPS Conference on Controlled Fusion and Plasma Physics, St. Petersburg, 2003), (Ed.) Koch, R., Lebedev, S. (EPS, Geneva), Vol. 27A, P-1.125.

W. Suttrop, M. Maraschek, G. D. Conway, H.-U. Fahrbach, G. Haas, L. D. Horton, T. Kurki-Suonio, C. J. Lasnier, A. W. Leonard, C. F. Maggi, H. Meister, A. Mück, R. Neu, I. Nunes, Th. Pütterich, M. Reich, A. C. C. Sips, ASDEX Upgrade Team, (2003), *ELM-free Stationary H-mode Plasma in the ASDEX Upgrade Tokamak*, Plasma Physics and Controlled Fusion 45(8), 1399-1416.

W. Suttrop, G. D. Conway, L. Fattorini, L. D. Horton, T. Kurki-Suonio, C. F. Maggi, M. Maraschek, H. Meister, R. Neu, Th. Pütterich, M. Reich, A. C. C. Sips, ASDEX Upgrade Team, (2004), *Study of Quiescent H-mode Plasmas in ASDEX Upgrade*, Plasma Physics and Controlled Fusion 46(5A), A151-A156.

x

Contents

1 Introduction

1.1 Nuclear fusion as an energy source

Nuclear fusion is slowly but steadily gaining interest as a potential solution to the earth's energy problem. As economically developing countries, like China and India, continue to consume increasing amounts of energy, the basic supply of energy will become one of the major issues worldwide in the near future.

Fusion power, the energy source with the advantage of an abundant fuel supply and the absence of greenhouse gas emission, is about to take a major step forward with ITER[1]. This is an ambitious international research project, whose "mission is to demonstrate the scientific and technological feasibility of fusion energy for peaceful purposes." [1]. This project will advance the effort to produce clean, safe, renewable, economical and commercially available fusion energy in the second half of this century.

The basis for fusion energy are nuclear fusion reactions between light elements, such as the hydrogen isotopes deuterium and tritium. In order to fuse particles, their nuclei need to overcome the repulsive Coulomb force. A simple colliding beam setup is unsuitable for this purpose due to the high cross section of elastic collisions compared to the fusion reaction cross section (at relevant energies $\sigma_{Coulomb}/\sigma_{fusion} \geq 50$). The solution is to confine the particles long enough in a thermalized plasma with high temperature so that a sufficient rate of fusion reactions compensates losses due to other processes. The most interesting fusion reaction (see Figure 1.1) is:

$$^2_1 D + ^3_1 T \longrightarrow ^4_2 He + ^1_0 n + 17.6 \ MeV \tag{1.1}$$

as it has the highest cross section at a center-of-mass energy of only about 65 keV [2]. Because of the high energy tail of a thermal velocity distribution, the relevant rate coefficient $\langle \sigma v \rangle$ is close to its maximum already at a temperature[2] $T \geq 10$ keV. At such temperatures atoms separate into ions and electrons. The resulting ionized gas is called a plasma. Movement of its charged particles constitute electric currents and can be influenced by magnetic fields because of the Lorentz force $\vec{F}_L = Ze\vec{v} \times \vec{B}$ (Z being the ionization state, e the elementary charge, $\vec{B}$ the magnetic field). They gyrate around field lines with a gyro-radius $\rho = mv_\perp(ZeB)^{-1}$ (m is the mass) while moving

---

[1]ITER: International Thermonuclear Experimental Reactor

[2]In high temperature plasma physics, temperatures are given in energy units, thus 1 eV$\approx$11400 K
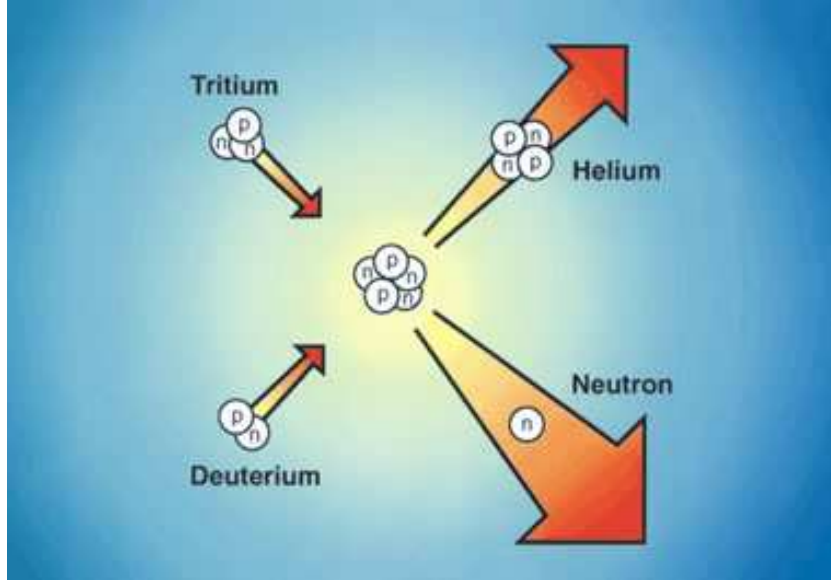
Figure 1.1: Deuterium and tritium collide in a fusion reaction to produce helium while releasing a neutron. The net energy gain of 17.6 MeV is released as kinetic energy distributed between the two end products.

freely parallel to the field. This is utilized to confine plasmas magnetically. A toroidal topology for the field has been most successful for keeping the particles bound because of the avoidance of end losses by closing the surfaces formed by magnetic field lines. The geometry of the torus is characterized by the major radius R and the minor radius r. The plasma shape is typically elongated vertically but the horizontal distance from the plasma center (magnetic axis) to the edge is still referred to as minor radius.

Without an additional poloidal field component, magnetic confinement in the toroidal chamber would not be possible. The topology of the torus leads to a gradient in the toroidal magnetic field, which creates a $\vec{B} \times \nabla \vec{B}$ drift separating ions and electrons. The resulting electric field interacts with the toroidal magnetic field to create an outward directed $\vec{E} \times \vec{B}$ drift on both ions and electrons, which destroys the confinement. The additional poloidal field component winds the field lines around the toroidal plasma column so that the particles on a specific field line spend part of their time on the low field side drifting away from the center and the other time on the high field side drifting towards the center of the plasma, keeping their radial position on average [2] (see Figure 1.2).

1.2 The tokamak

The most advanced toroidal magnetic confinement principle is the tokamak (tokamak is an abbreviation from the Russian expression for toroidal chamber with magnetic field).
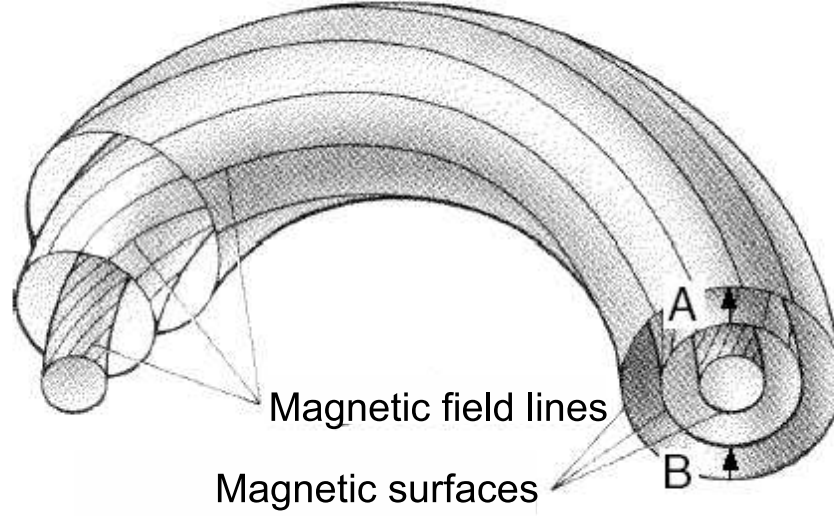
Figure 1.2: Nested magnetic surfaces with bent magnetic field lines. Positions A and B indicate the particle drifts which are opposite to each other depending on the position relative to the center.

A comprehensive overview can be found in [3]. The tokamak is characterized by an ohmic transformer coil that induces a plasma current I_p (see Figure 1.3) which provides the required poloidal magnetic field. The stellarator, which generates all fields externally, is an alternative, nonaxisymmetric toroidal magnetic confinement device (see e.g. [4]), but not further discussed here.

The induced current heats the plasma resistively and provides the first step towards reaching fusion relevant temperatures. However, this heating method is not sufficient on its own, due to an adverse temperature dependence of the resistivity ξ ($\xi \propto T^{-3/2}$ [5]). At ASDEX Upgrade[3], additional heating is achieved [6] by means of wave heating (ion and electron cyclotron resonance heating, ICRH and ECRH) and neutral beam injection (NBI), which transfers kinetic energy of injected particles (H or D) to the plasma by collisions.

The helical configuration of field lines leads to the formation of magnetic surfaces which are nested inside each other (see Figure 1.2). The particle mobility along field lines is very high and the heat conductivity κ is several orders of magnitude higher parallel to the field than perpendicular to it (see also Section 2.3.2). Therefore, toroidal symmetry as well as fast equilibration of plasma properties in the poloidal direction on the magnetic surfaces are typically assumed. The average field line geometry on a given surface is described by the so-called safety factor q. Rational values of q give rise to macroscopic

---

[3]ASDEX Upgrade = Successor to ASDEX (Axial Symmetric Divertor EXperiment, fusion research facility near Garching bei München, Germany), see also Appendix B
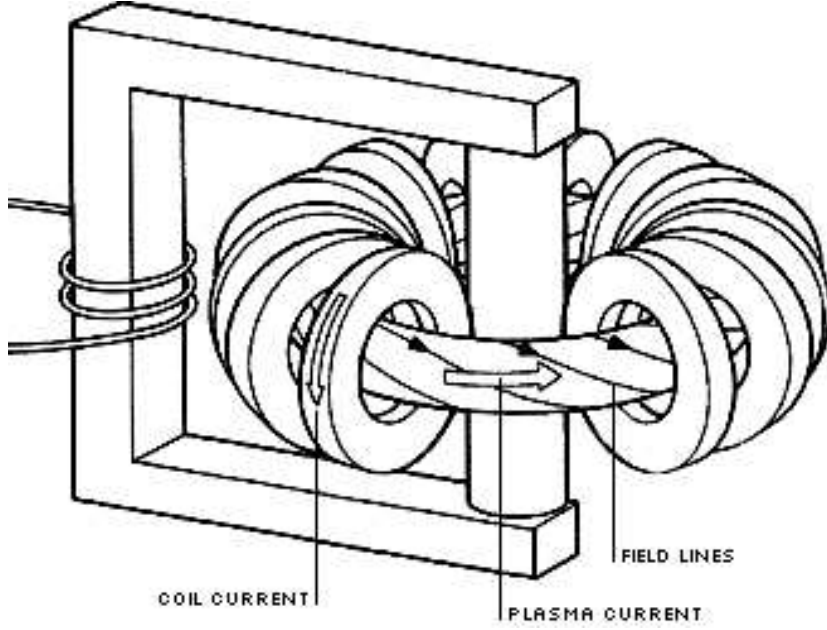
Figure 1.3: Schematic picture of a tokamak: Toroidal field coils produce the main toroidal field, while the transformer induced plasma current adds a poloidal field component. Magnetic field lines are helically wound and form magnetic surfaces.

instabilities. Its definition is [3]:

$$q = \frac{1}{2\pi} \oint \frac{1}{R} \frac{B_t}{B_p} ds \tag{1.2}$$

where the integration is over a single poloidal circuit around the flux surface (B_t and B_p are the toroidal and poloidal field components). A value of $q = b/d$ means that a field line on the corresponding surface needs b toroidal loops until d poloidal rotations are completed. In a conventional tokamak scenario, q is $\gtrsim 1$ in the center and rises monotonically to a value of 3-6 at the edge of the plasma, the exact value depending on total plasma current and magnetic field.

The ASDEX Upgrade tokamak was designed with additional coils producing a magnetic divertor configuration [7]. They create a magnetic X-point that defines the last closed magnetic surface without wall contact, which is called separatrix. The open field lines outside the separatrix form the scrape-off layer (SOL). They are intersected by target plates, which are placed away from the main chamber in order to keep sputtered impurities from entering the plasma. Figure 1.4 shows a cross-section of an ASDEX Upgrade H-mode plasma explaining some key features and showing schematic radial profiles of temperature and density.

1.3 Progress towards realizing a fusion power plant

In order to run a fusion reactor in such a tokamak configuration, losses from particle transport, convective and conductive heat transport perpendicular to the field and radiation (line radiation and Bremsstrahlung) must be compensated by the fusion reaction's energy release. Temperatures of about 15 keV and densities $n \geq 1 \cdot 10^{20}$ m^{-3} will be sufficient for reaching high fusion rates. An important figure of merit for the quality of the confinement is the energy confinement time $\tau_E = W_{plasma}/P_{heat,auxiliary}$. The Lawson criterion includes realistic estimates for the losses and conversion efficiencies and predicts "break-even" (where the auxiliary heating power equals the total fusion power, i.e. fusion gain Q=1) for $n\tau_E \gtrsim 6 \cdot 10^{19} sm^{-3}$ at $T = 15 - 20$ keV. "Ignition" ($Q \to \infty$) occurs when heating by fusion-born alpha particles which carry 1/5 of the released energy compensates all losses and the plasma energy is self-sustained without external heating.

The H-mode (high confinement mode) is a plasma regime at conditions compatible with a future reactor. It was identified 20 years ago at ASDEX [8] and is now extensively studied and developed further at ASDEX Upgrade and many other fusion experiments worldwide. It is the reference scenario for the planned international tokamak experiment ITER [9]. The confinement of

Figure 1.4: Schematic cross-section of the ASDEX Upgrade reactor with magnetic surfaces (dashed lines). (a) core plasma, (b) pedestal top in temperature and density, (c) last closed magnetic surface, also called separatrix, (d) magnetic X-point, (e) scrape-off layer (SOL), (f) divertor region.

the H-mode crucially depends on the good thermal insulation at the edge, which manifests itself in the so-called pedestal observed in radial profiles of density and temperature (compare with Figure 1.4, (b)). Simulations of the core plasma predict that the ITER design value for a fusion gain of $Q = 10$ can be achieved, if the ion temperature at
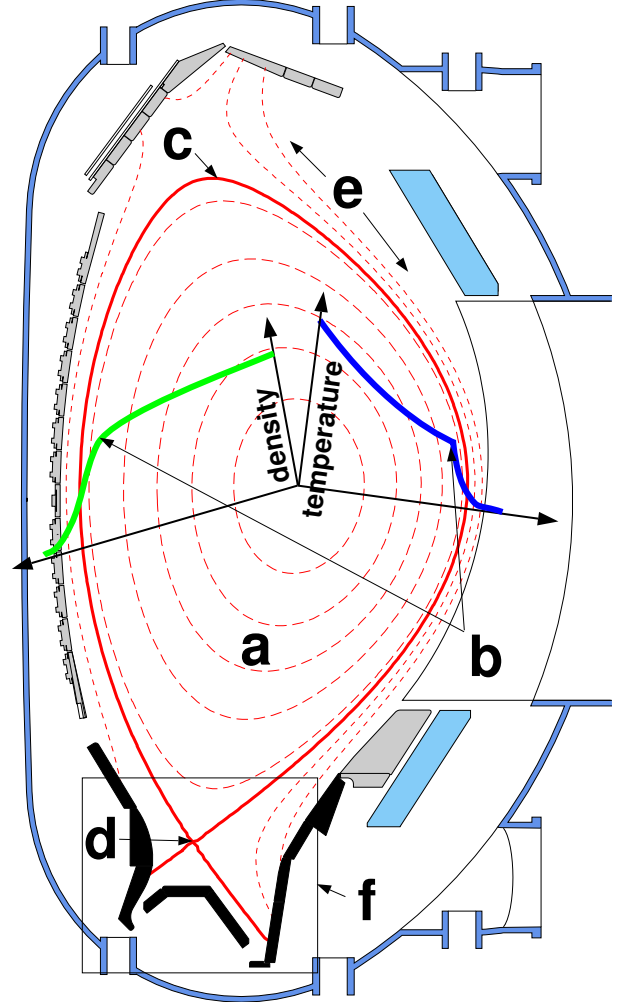
the pedestal top reaches about 4 keV [10]. The physics behind the formation of the barrier, however, and the remaining particle and energy transport through it are still not understood despite considerable effort [11]. Empirical scaling laws based on linear regression are used instead to extrapolate to reactor-size experiments. Whether or not results in present machines indeed extrapolate to ITER can only be verified when the underlying physics are qualitatively and quantitatively understood.

In order to advance theoretical understanding of H-mode edge plasmas, accurate profiles with spatial resolution below 1 cm for all relevant properties are necessary. While electron temperatures and densities are routinely available from Thomson scattering of laser light on free electrons [12], edge ion temperatures are not available to the required accuracy in most machines. For specific exploration of the edge region, ion temperature measurements with sufficient spatial resolution to cross-check models based on the local ion temperature or the ion-temperature gradient are indispensable.

1.4 Contents of this work

This work was aimed at realizing edge ion temperature measurements with sufficient radial resolution at ASDEX Upgrade by means of charge exchange recombination spectroscopy (CXRS) using a diagnostic lithium beam. In Chapter 2, the need for accurate edge ion temperature measurements is explained by summarizing some questions in tokamak theory which cannot be verified without this experimental data. It presents the H-mode, the default plasma scenario for ITER, and outlines not fully understood issues about this plasma regime, thus motivating the diagnostic extension.

Data from existing diagnostics were used to compare to and combine with the Li-beam CXRS measurements. Brief descriptions of the diagnostics used for that purpose are given in Chapter 3. A procedure with the necessary steps to construct the best possible density and temperature profiles for detailed investigations and modeling is also explained there. The principle and the implementation of the new diagnostic is described in Chapter 4. The lithium beam is a standard tool for electron density measurements at ASDEX Upgrade and the extension to also use it for determining accurate edge ion temperatures comprises the main part of this work. The comparison of newly acquired measurements to data of already existing diagnostics serves mainly as a validation of the new diagnostic.

Chapter 5 shows exemplary measurements with the lithium beam edge ion temperature diagnostic in pure ohmic plasmas, auxiliary heated low confinement (L-mode), high confinement (H-mode) and quiescent high confinement (QH-mode) plasmas. It also contains an empirical characterization of electron heated plasmas and first results from edge plasma modeling which makes use of the newly available ion temperature measurements. Chapter 6 summarizes the results.

2 Background and motivation

2.1 Scaling of energy confinement time

In order to sustain thermonuclear reactions, it is important to maintain the plasma stored energy $W = \int \frac{3}{2}(n_e T_e + n_i T_i)d^3x$ (n_e, n_i being the density of electrons and ions). In stationary conditions (dW/dt=0), the power loss rate of $P_L = W/\tau_E$ is compensated by total plasma heating, hence the definition of energy confinement time (compare with Chapter 1). The needed heating power, together with the integrated plasma energy, provides the means of experimentally measuring the confinement time, which characterizes on a global scale the energy transport in the plasma.

Without any plasma turbulence or instabilities, τ_E would be solely determined by collisional and radiative losses and could in principle be calculated. However, it is found that in present machines the transport is usually due to gradient driven turbulence (described later in more detail). Therefore, in the absence of good theoretical understanding of confinement, empirical methods and scaling laws derived using statistics are applied to predict the dependence of the confinement time on the relevant parameters. Using the acquired information, key parameters (such as current or magnetic field) can be identified and global performance optimized.

Scaling laws are often based on operational and engineering parameters such as I_p, B, R or r. However, in order to extrapolate to future devices, a dimensionless approach is advocated. Normalized variables (e.g. normalized gyro-radius $\rho^* = \rho/a$, $a = r_{separatrix}$) are needed in order to catch the underlying mechanisms that govern confinement from the physics point of view. This puts certain constraints on the functional dependence [3], which depend on the exact theory. The ITER scaling laws satisfy the Kadomtsev constraints [13] at least approximately. Figure 2.1 shows the empirical multi-machine scaling of global energy confinement time of H-mode plasmas for ITER.

2.2 Plasma regimes

2.2.1 Ohmic and auxiliary heated L-mode plasmas

In order to sustain a plasma in a magnetic confinement device, energy losses through convective and conductive heat transport and radiation must be compensated. At low
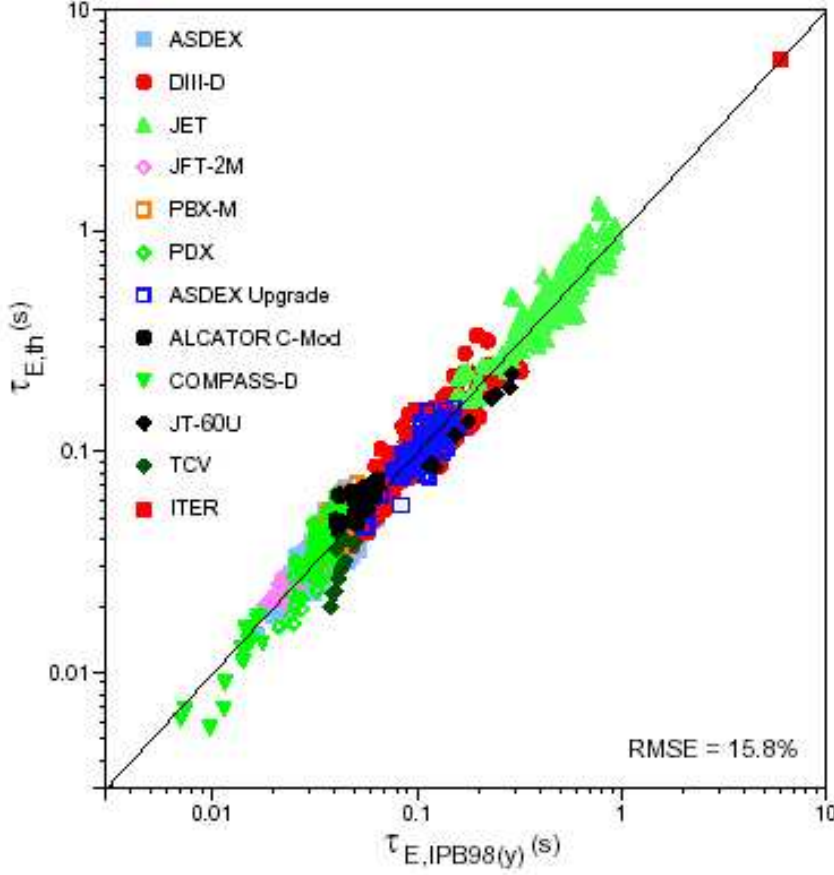
Figure 2.1: Comparison of H-mode thermal energy confinement time, as measured by different facilities, with the empirical scaling for data from the ITER H-mode database version DB3 (Source: [14]). The expected value for ITER dimensions is plotted in the top right corner.

tokamak temperatures, resistivity leads to substantial heating [3]. The typical amount of total ohmic heating power in ASDEX Upgrade plasmas is about 1 MW due to a plasma current of $I_p = 1$ MA and a transformer induced loop voltage of $U_{loop} = 1$ V. When temperatures are increased to fusion relevant levels, the ohmic heating power decreases because the plasma resistivity ζ is proportional to $T^{-3/2}$. Therefore auxiliary heating methods (e.g. electron cyclotron resonance heating (ECRH), ion cyclotron resonance heating (ICRH), neutral beam injection (NBI)) are needed. When such heating is applied, the plasma switches into a different mode of operation, the low confinement mode or L-mode. The name was adopted when experiments showed a reduced energy confinement compared to purely current heated "ohmic plasmas". The empirical scaling [3] shows $\tau_E \propto I_p R^{1.75} a^{-0.37} P^{-0.5}$. Most notable is the loss of confinement with added heating power P, which does not favorably extrapolate to an economically competitive fusion reactor.

2.2.2 H-mode plasmas

During neutral beam heating experiments on the ASDEX tokamak, it was discovered that when the NBI heating power exceeds a threshold, which dominantly depends on plasma density and magnetic field, there is a sharp transition into a different confinement regime [8]. This regime improves confinement times by about a factor of two over L-mode scaling. This gain reduces the necessary size of a future reactor significantly. Other heating methods were later found to trigger a transition at a similar power level. The plasma regime is called high confinement mode (H-mode). An early scaling law for the H-mode confinement time was $\tau_{E,thermal} \propto I_p^{1.06} R^{1.9} a^{-0.11} n^{0.17} B^{0.32} P^{-0.67}$ [3].

The H-mode's confinement improvement originates near the edge, where large radial gradients in density and temperature are observed after the transition. The pedestal top (see also Figure 3.1) marks the transition zone from steep to less steep gradients of the core plasma. Its exact radial position can be different for temperature and density profiles. Between the pedestal top and the separatrix a reduced level of particle and heat transport perpendicular to the field (an edge transport barrier) leads to the steep gradients.

A variety of theories exist for the creation of transport barriers in the plasma [15], but none of them are conclusive. The transition to the H-mode regime (called the L-H transition) is under investigation and many theories have been proposed [11]. Among other effects, the local ion temperature or the ion temperature gradient is predicted to play an important role in the access to enhanced edge confinement. The access to and the sustainment of H-mode with its edge transport barrier is directly linked to the question of transport across the pedestal region before and after the transition, so a close look at plasma transport in this narrow edge layer is necessary.

2.3 Transport in a magnetized plasma

2.3.1 Random walk process

The approximate magnitude of a diffusive transport process can be estimated by a random walk argument which results in a diffusion coefficient, D, derived from a characteristic step size and time step:

$$D \quad \propto \quad \frac{(\text{step size})^2}{\text{time step}} \tag{2.1}$$

The right order of magnitude of plasma transport processes can then be determined by using the right step size and time step. In collisional theories, the relevant time step is always a collision time between the participating species, the correct step size depends

on the particular type of transport.

Owing to the gyrating orbits of particles in a magnetic field, transport parallel and perpendicular to the field is strongly different. Applying the random walk argument, the step size parallel to the field is related to the mean free path, which is given by the thermal velocity v_{th} times the collision time τ_c, e.g. electrons at 100 eV and a density of $2 \cdot 10^{19} m^{-3}$ have a step size of $\Delta x = \lambda_{mfp} \approx 4.25$ m. The step size perpendicular to the field, however, is given by the Larmor radius and under the same conditions (and a field $B = 2$ T) is less than $2 \cdot 10^{-5}$ m for electrons and about 1 mm for deuterium ions. Since the step size enters quadratically and time steps are the same, parallel transport typically exceeds perpendicular transport by several orders of magnitude.

2.3.2 Tokamak edge transport and transport coefficients

The transport at the plasma edge of divertor tokamaks is influenced by presence of a separatrix [16] which causes a rapid change in the fluxes parallel to the magnetic field due to the intersection of field lines outside the separatrix with walls. This generates large parallel gradients and fluxes (e.g. electron heat flux $Q_{e,\parallel} \propto T_e^{5/2} \nabla_\parallel T_e$), which quickly drain particles and energy to the targets resulting in a rather narrow scrape-off layer. Clearly, an at least two-dimensional description is required for proper theoretical treatment. On magnetic surfaces, which are closed within the tokamak, the high parallel heat conductivity $\kappa_\parallel$ leads only to a rapid equilibration of temperature and density which makes a one-dimensional description sufficient due to practically constant properties parallel to the field. Since parallel transport is thus well described by classical collisional theory, all further references to transport will focus on transport perpendicular to the magnetic field.

Classical diffusive cross-field transport cannot explain the experimentally determined fluxes of energy and particles in tokamak experiments. A substantial body of theory exists for the description of the more complex collisional transport in a magnetized torus, referred to as "neoclassical transport" [17]. This theory correctly accounts for field curvature and for the enhanced transport due to trapped particles (described later in more detail) but the high level of transport in current fusion devices cannot be explained by this theory.

For the empirical calculation of local transport a transport equation which relates the observed particle fluxes Γ_j and heat fluxes Q_j to the gradients of electron density, ion and electron temperature by means of the transport matrix A_{ij}, is postulated:

$$(\Gamma, Q)_j \;=\; A_{ij} \nabla(n, T) + C_j f(n, T) \qquad (2.2)$$

The diagonal elements of the transport matrix provide the diffusive contribution, typically referred to as diffusion coefficient D and heat transport coefficient χ, which replaces the classical heat conductivity $\kappa_\perp$ ($\equiv n\chi$) for cross-field transport. In contrast to neoclassical theory, little is known a priori about the transport matrix in case of anomalous,

turbulent transport. Therefore, for simplicity, off-diagonal terms, specifically in the particle transport equation, are often not explicitly written but replaced by vn_e to account for convective contributions to the fluxes. A subset of the transport equations, in particular the equations for particle transport and heat transport (without convection) is:

$$\Gamma_{e,i} = -D\frac{dn_e}{dr} + vn_e \tag{2.3}$$

$$Q_e = -n\chi_e\frac{dT_e}{dr} \tag{2.4}$$

$$Q_i = -n\chi_i\frac{dT_i}{dr} \tag{2.5}$$

The momentum transport equations which are part of the full set are not of importance in this work and thus omitted. Within this formalism, transport coefficients can be both measured experimentally and calculated from equations based on theoretical models. The comparison is then as straightforward as possible. It is desirable to eventually calculate the coefficients from first principles and thus completely understand the underlying physics. Since a complete description encompasses a huge phase space (e.g. machine size: 1 m, electron gyro-radius: 10^{-5} m) even the largest computers cannot yet cope with all physics simultaneously. At the moment only experimental determination and theoretical approximations using certain simplifications are possible. For both cases, however, accurate ion temperature profile measurements are desired.

Transport times

From transport coefficients, in general, a typical "transport timescale" can be inferred by making an estimate about the length-scales involved. The gradients are providing the drive for transport, hence the density and temperature gradient lengths, defined by

$$L_n = \frac{n}{\nabla n} \tag{2.6}$$

$$L_T = \frac{T}{\nabla T} \tag{2.7}$$

are key quantities. With a given particle diffusion coefficient D or heat conduction coefficient χ, the transport times over a gradient length are then defined as:

$$\tau_{n,transp} = \frac{L_n^2}{D} \tag{2.8}$$

$$\tau_{T,transp} = \frac{L_T^2}{\chi} \tag{2.9}$$

As long as heat exchange times of the main plasma ions are smaller than the transport times, a local Maxwellian velocity distribution will be a good approximation and the definition of a local temperature is reasonable. This must in principle be checked on an individual basis and has been found to be valid for ASDEX Upgrade plasmas. In the following, the above-mentioned types of cross-field transport will be described in more detail.

2.3.3 Classical transport

While heat and momentum transport is usually dominated by the shortest relevant collision time and the largest step size, particles are only transported by collisions between unlike particles, such as electrons and ions. Due to inherent ambipolarity because of the momentum conservation, that type of transport proceeds at the smaller step size of the electrons. Total heat and momentum fluxes are sometimes subdivided into the "ion channel" and the "electron channel", since they are governed by respective like particle collisions, at least in the case of ions (larger gyro-radius than electrons).

In this classical picture, which is strictly valid only in cylindrical geometry, the ion particle, electron heat and particle cross-field transport have a diffusion coefficient $D, \kappa \propto \rho_e^2 / \tau_c$, where τ_c is the relevant collision time. Ion heat transport is described by the ion Larmor radius ρ_i as the step size. Collision times depend on temperature and are proportional to the square root of the colliding species' mass. Diffusion coefficients derived from this picture (excluding the trivial dependence on magnetic field ($\propto B^{-2}$)) are therefore:

$$\underline{\text{Cross-field Transport}} \quad \text{depends on}$$

$$\text{Electron and ion particle} \quad \tau_{ei},\, \rho_e \quad D \propto \left(\frac{m_e}{m_i}\right)\left(\frac{m_e}{T_e}\right)^{1/2} \tag{2.10}$$

$$\text{Electron heat} \quad \tau_e,\, \rho_e \quad \chi_e \propto \left(\frac{m_e}{T_e}\right)^{1/2} \tag{2.11}$$

$$\text{Ion heat} \quad \tau_i,\, \rho_i \quad \chi_i \propto \left(\frac{m_i}{T_i}\right)^{1/2} \tag{2.12}$$

2.3.4 Neoclassical transport

The collisional transport in toroidally confined plasmas is significantly different from the one in cylindrical geometry and therefore called neoclassical transport [17]. The level of neoclassical transport forms the lower limit of cross-field transport in a tokamak. While neoclassical theory is still being refined, most issues have been resolved and some are presented in the following.
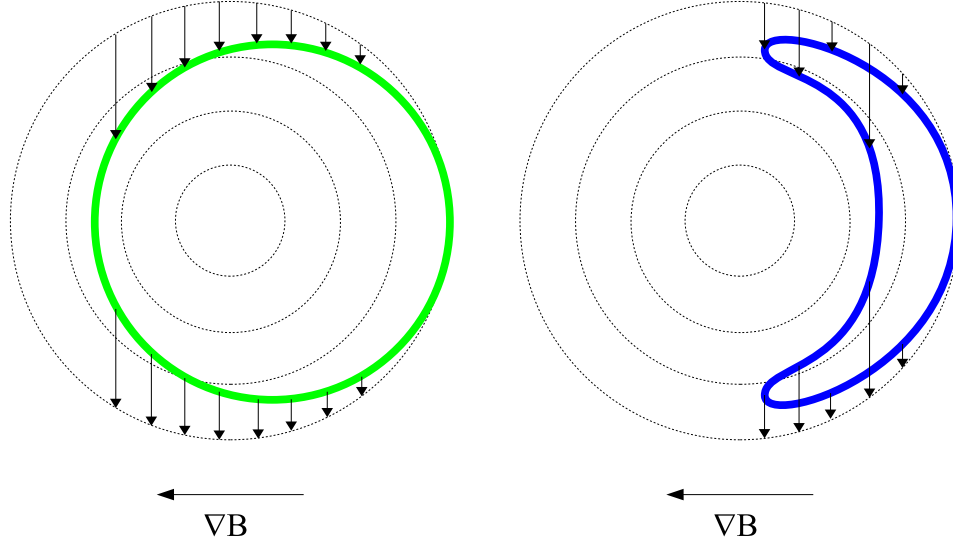
Figure 2.2: Schematic poloidal projection of passing (left) and trapped (right) charged particle orbits in a tokamak. Magnetic surfaces are indicated with dotted lines. The particles experience a vertical drift dependent upon their velocity parallel to the magnetic field.

In addition to the increase of the diffusive part by the Pfirsch-Schlüter factor [18], transport is enhanced due to trapped particles. Particles can become trapped on the outer side of the torus by the magnetic mirror formed as a result of the poloidal variation of the magnetic field. Particles with sufficiently large velocity parallel to the magnetic field do not become trapped and are referred to as passing particles (see Figure 2.2, left). Trapped particles travel on "banana orbits", which get their name from the poloidal projection of their guiding center[1] motion, which looks like a banana (see Figure 2.2, right). Using the random walk argument from above, the effective step size for particles on banana orbits is increased from the gyro-radius, ρ, to the banana width $w_b \propto q\sqrt{(R/r)}\rho$, therefore a larger transport due to collisions is expected. The exact amount depends on the fraction of trapped particles and on the number of collisions per banana bounce period. A more thorough discussion can be found in [19].

The dimensionless collisionality parameter

$$\nu^* = \frac{Rq}{\tau_e v_{th}} \tag{2.13}$$

distinguishes three different plasma transport regimes. When the collision time for the majority of particles is longer than the time to complete a full banana orbit which is the case for $\nu^* < (r/R)^{3/2}$, the transport is dominated by trapped particles and the plasma is said to be in the "banana regime". At high enough collisionality ($\nu^* > 1$), particles are constantly de-trapped by scattering in velocity space and the plasma is said

---

[1]Guiding center: gyro-orbit averaged center-of-mass of a gyrating particle.
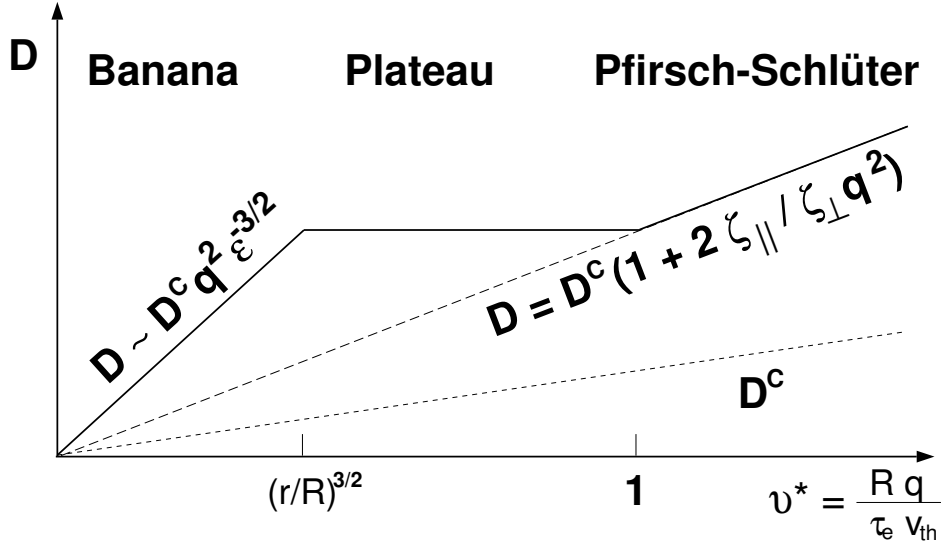
Figure 2.3: Schematic overview of transport regimes, defined by neoclassical theory. Simplified regime transitions happen at threshold values of the dimensionless collisionality parameter. The classical diffusion coefficient for a mono-energetic particle is included for comparison.

to be in the "Pfirsch-Schlüter regime" or simply the plasma is collisional. The plateau regime designates the region in collisionality space where neither the trapped particles nor the passing particles but slowly circulating particles are dominantly determining the collisional transport [3]. Figure 2.3 shows schematically the regime transitions and the resulting neoclassical particle diffusion coefficient D_{neo}.

Since the exact calculation of the neoclassical transport level is not straightforward, computer codes and simplifications with corrections for special cases are used to compare the coefficients to the experimentally measured ones. While D may approach neoclassical levels in the core, it is clearly anomalous at the edge by about the same factor as electron heat transport, which exceeds the neoclassical prediction by orders of magnitude ($\chi_{e,exp.} \approx 10^2 \chi_{e,neo}$). Ion heat transport is typically closest to the neoclassical values ($\chi_{i,exp.} \approx 1 - 10 \chi_{i,neo}$).

These numbers indicate that collisional transport, even with the neoclassical corrections, is not sufficient to explain the experimental heat and particle fluxes in fusion plasmas. The identification of processes that explain this "anomalous" part of the heat and particle fluxes is an active field of research.

2.3.5 Anomalous transport and turbulence

Tokamak transport in the L-mode regime is generally anomalous, a fact attributed to turbulent transport by large-scale turbulence and micro-instabilities. Turbulent fluctuations create radial correlations which effectively increase the step size in the random

walk analogy by a significant factor and thus drive higher fluxes.

After an H-mode is attained and the edge transport barrier formed, the level of fluctuations at the edge drops significantly in a broad frequency range but there is still significant anomalous transport across the barrier, at least in the electron channel. For this case it is generally accepted that "plasma transport across the magnetic field is largely controlled by low-frequency drift-wave fluctuations" [20].

One of the more prominent examples of drift-wave turbulence is the so-called ion temperature gradient (ITG) or η_i-mode ($\eta_i = L_n/L_{T_i}$). It is the most important instability with respect to ion thermal confinement in fusion plasmas and excited when L_{T_i} exceeds a critical value, which was successfully used to explain stiff core ion temperature profiles[2] as observed in ASDEX Upgrade H-mode plasma discharges [21]. While the necessity for accurate ion temperature profiles is already obvious from this short discussion, it is further emphasized in the following.

2.4 Edge transport barrier and L-H transition

As mentioned above, the ion temperature at the top of the pedestal provides the boundary condition from which the core profile can be directly determined under certain conditions. Under these conditions, higher pedestal temperatures translate directly into a higher plasma temperature in the center. It is therefore of great importance to better understand the particle and heat transport barriers that generate the pedestal. This requires knowledge of all relevant plasma properties to test existing or develop new models of the plasma edge region. One of the first theories about the L-H transition postulated an edge stabilization by enhanced radial electric fields due to ion orbit losses [22]. Since these orbit losses depend on collisionality ($\nu^* \propto 1/v_{th}$), the implicit dependence on ion temperature is obvious. T_i could indeed be a key parameter for triggering the L-H transition, experimental evidence was recently seen on JET[3] [23]. Qualitatively, the change of electric fields as postulated by the theory could already be confirmed by Doppler reflectometry measurements at ASDEX Upgrade [24]. Since the poloidal flow due to $\vec{E_r} \times \vec{B}$ shear strongly stabilizes the ITG mode and reduces the radial correlation length of large-scale turbulence, it is a promising theory to explain the L-H transition, at least in parts.

Testing of critical gradient models (such as the ITG mode) depends on the knowledge of ion temperature gradients. Threshold criteria need to be compared with experimentally measured gradients to identify the L-H transition onset as well as to identify which instabilities determine the height of the pedestal and the width of the barrier. For these investigations, edge ion temperature gradients must be measured with high enough accuracy to improve upon the currently used models, which usually assume $T_e \approx T_i$.

---

[2]Stiff T_i profile: Core T_i-profile determined by T_i at the pedestal due to fixed gradient length L_{T_i}

[3]JET: Joint European Torus, Culham, UK

2.4.1 Continuous transport across the edge barrier

While access to the H-mode is one important step towards a successful reactor grade experiment, it is also necessary to look at ways to keep a plasma in this favorable mode of operation while at the same time substituting the produced ash (helium) with new fuel (deuterium). A certain amount of transport needs to be maintained and controlled. Part of the fluxes are given by the irreducible neoclassical transport due to collisions, but additional transport due to effects related to edge instabilities also plays a role.

In order to determine the different (neoclassical, anomalous) contributions to the transport across the barrier, again, radial profile measurements of densities and temperatures are required. The gradients determine most of the drive for collisional transport and at the same time determine the onset level of micro-instabilities which can be compared to theoretical models.

When impurities (including the helium ash in a future reactor) are not removed from the plasma due to too low edge transport, impurity accumulation and eventually loss of confinement due to a radiative collapse of the plasma can occur.

2.4.2 Critical gradients and ELM transport

Low transport in the edge barrier region will typically steepen gradients of density and temperature to levels where magneto-hydrodynamic (MHD) stability limits are exceeded. At the edge, the most important threshold is that for the onset of ideal ballooning modes with a high mode number, which are a type of ideal[4] MHD-instability predicted to grow once a critical edge pressure gradient is exceeded. Then, instabilities can develop and generate high transport on very short timescales. The typical event is a so-called edge localized mode (ELM), which leads to a burst-like expulsion of particles and energy from the pedestal while relaxing the pressure gradient. In the standard model of an ELM, a pressure driven ballooning type instability puts a limit on the pressure gradient until the bootstrap current, also driven by the pressure gradient[5], becomes effective and triggers a peeling mode instability, finally resulting in a crash of edge pressure gradient and edge current. Figure 2.4 provides a schematic picture of the situation. The authors of the theory [25] thus call the ELM a radially localized, coupled peeling-ballooning mode.

The ELM itself contributes significantly to the transport of particles and energy across the separatrix. Typical ELMs reduce the global energy confinement by about 10-20% on average. The ELM is interesting in itself because of the high energy fluxes to the divertor, which are an important issue for the divertor target plate design [26]. It is also of interest to quantify the remaining transport between ELMs to gain insight into

---

[4]Ideal MHD: plasma resistivity $\rightarrow 0$.

[5]In the banana regime, there is a current contribution due to the enhanced diffusion (banana orbits) which scales as $j_b \propto -\frac{1}{B_p}\frac{dp}{dr}$ and is known as the bootstrap current [3].
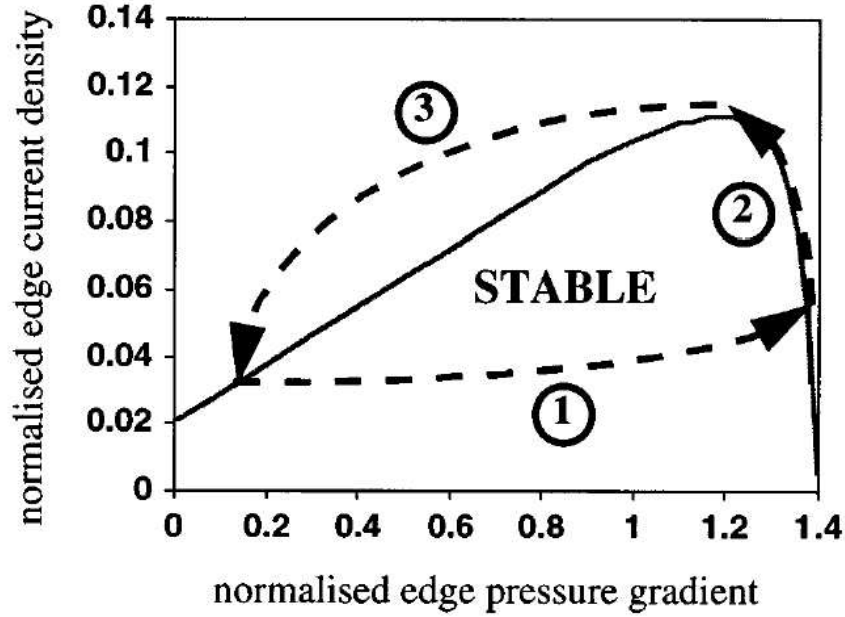
Figure 2.4: Plasma parameter evolution during ELM cycle (dashed curve) relative to edge MHD stability boundary (full curve): edge pressure gradient rises up to ballooning limit (1), which restricts further increase; edge current rises due to ohmic and bootstrap currents (2) up to top corner of stability boundary; plasma instability flushes out pressure, enhancing the instability and resulting in a crash of the edge pressure gradient and current (3), which is interpreted as the ELM crash. The cycle repeats with further heating (source: [25]).

the physics that leads to the crashes and insight into the transport through the edge barrier [27]. Whether ELMs can be controlled or completely avoided is an important issue for ITER.

Comprehensively understanding the edge plasma is not possible without accurate measurements of all relevant plasma properties. This includes information about edge ion temperatures and this work addresses the experimental means of obtaining these profiles.

3 Pedestal profiles

3.1 Introduction

The prevalent feature of the high confinement H-mode regime routinely obtained in divertor tokamaks is the so-called edge pedestal, which is clearly observed in one-dimensional temperature and electron density profiles (see Figure 3.1). As mentioned before, its formation is typically explained by a transport barrier just inside the separatrix, which results in the build-up of steep gradients. Further inside the plasma, where transport is higher, the profiles are flatter. Thus, the pedestal top is experimentally also understood as the transition zone from edge plasma to core plasma.

The top of the pedestal is the edge boundary of the plasma interior. Core transport theory has progressed to a point where it is able to predict quite accurately core plasma
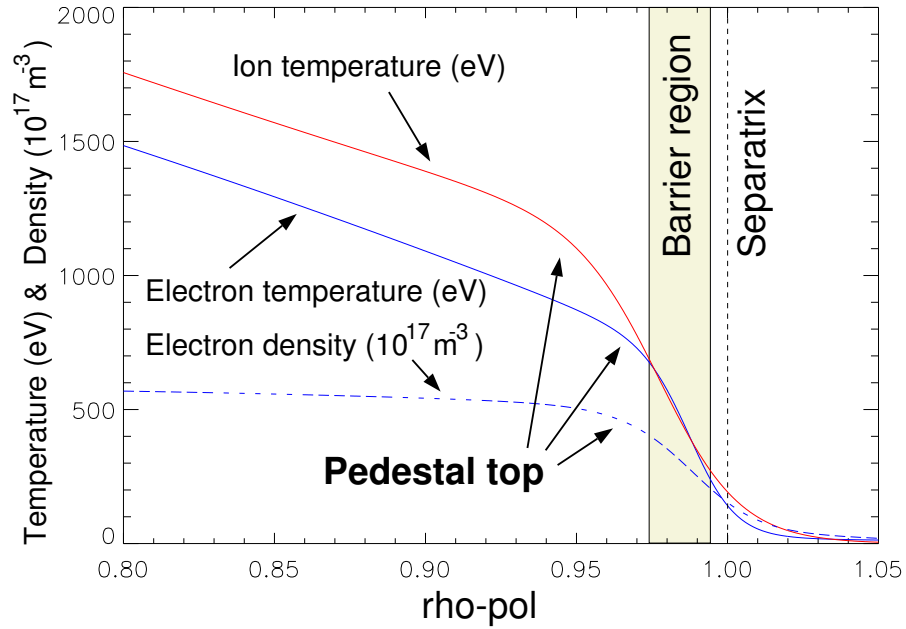

Figure 3.1: Fitted edge profiles of a typical ASDEX Upgrade H-mode plotted versus a normalized poloidal magnetic flux coordinate (plasma center at 0.0, separatrix at 1.0). A pedestal is observed in both temperature profiles and the electron density profiles separately.

behavior for given boundary conditions at the pedestal top [21] under a variety of conditions. It is essential to understand the physics that govern the parameters there in order to properly design a next step experiment. Highly specialized diagnostics are used at several divertor tokamaks to provide input for a better theoretical understanding of this region.

In the core plasma of ASDEX Upgrade, electron temperature and density are routinely measured with high temporal and moderate spatial resolution: $1\mu s < \Delta t < 8ms$, $1\ cm < \Delta r \lesssim 4\ cm$, depending on diagnostic settings. Ion temperatures are typically available with a resolution: $\Delta t \approx 50ms, \Delta r \approx 3 - 4\ cm$, when neutral heating beams are used. At the plasma edge, specialized instruments are required to achieve the spatial resolution ($\Delta r < 1$ cm) needed to resolve gradients with sufficient detail, but only available for electron temperature and density. However, ion temperature measurements are indispensable for benchmarking theoretical models that exist for the edge plasma, e.g. transport models [28] or theories for the L-H transition [29]. Presented in this chapter is a selection of the ASDEX Upgrade diagnostics, directly or indirectly used for cross checks with lithium beam ion temperatures. The three-letter abbreviations given in the titles of the following sections may be later used to reference these diagnostics. In addition, a tool ("AUGPED", created by L.D. Horton) is described which allows the combination of data from multiple diagnostics to create best possible profiles for a given discharge (also known as "shot" or "plasma shot"; each discharge is given a unique number, numbering is sequentially from #1 when the experiment was started to #19546 as of October 2004).
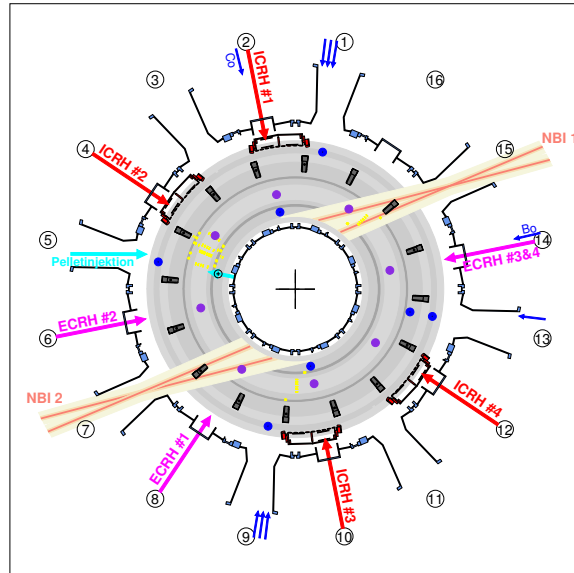

Figure 3.2: Toroidal cross section, overview of ASDEX Upgrade: Diagnostics and additional heating are distributed all around the torus, but the plasma is often described by just one-dimensional profiles of density and temperature.

Diagnostic hardware at ASDEX Upgrade is placed at different toroidal positions around the vessel due to space constraints (Figure 3.2). Toroidal symmetry, however, can be assumed because of rapid transport along field lines (compared to transport perpendicular to $\vec{B}$). Since the magnetic field lines form closed surfaces inside the separatrix, a transformation of position to a common coordinate related to the magnetic surfaces allows to use 1-dimensional profiles of temperatures and densities. In this way, a comparison of local properties becomes possible. This is described later (Section 3.5) in more detail. In the following, routinely available diagnostics at ASDEX Upgrade that were used for validation and comparison are briefly discussed.

3.2 Electron temperature measurements

3.2.1 Thomson scattering (YAG/YAR)

Standard laser scattering measurements at ASDEX Upgrade are based on Thomson scattering of monochromatic light on free electrons. The geometry is chosen in such a way that the wave vector $k = k_i - k_s$ (where subscript i denotes the incident and s the scattered radiation) satisfies $k\lambda_D \gg 1$ (λ_D is the Debye-shielding length) and thus the light is scattered on uncorrelated free electrons. Then, for a thermal velocity distribution, the scattered power has a Gaussian shape which determines the electron temperature of the scattering volume.

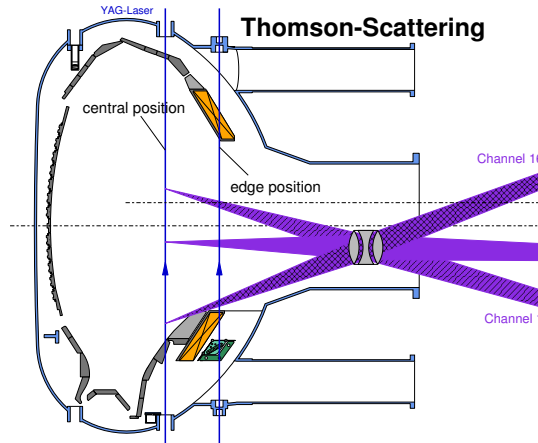**Figure 3.3:** Thomson scattering system at ASDEX Upgrade. In the central position, profiles of electron density and temperature are measured over the full plasma radius. In the edge position, radial coverage is swapped for enhanced radial resolution. Additional plasma shifts across the fixed laser paths allow high precision edge profile measurements.

ASDEX Upgrade is equipped with a Thomson system [30] featuring vertical laser beams,

which acquires a full radial profile ($\Delta R \approx 3 - 4\ cm$) every 8.3 ms. The abbreviation used for this "core" system is YAG. For special edge investigations, however, the system can be moved. In the edge setup (YAR), the six laser beams, each 2 mm wide, are launched vertically through the edge plasma, equally distributed in radial direction over a 15 mm wide interval. The scattered light is observed through a horizontal port in 16 vertically separated channels, delivering a radial resolution sufficient to resolve gradients with millimeter precision. To correct for misalignments, it is common practice to perform plasma shifts for improving the edge profiles by then possible laser-to-laser calibration. Pre-programmed plasma movement also helps to increase the observed radial range including the pedestal top while retaining the high resolution.

3.2.2 Electron Cyclotron Emission (ECE)

The ECE diagnostic determines electron temperatures by radiometry of electron cyclotron emission from the fusion plasma. Hot electrons in the plasma gyrate around field lines with cyclotron frequency $\omega_c = \frac{eB}{m_e}$, where e is the elementary charge, B the magnetic field, and m_e the electron mass.

At the second harmonic of the electron cyclotron frequency, the plasma usually emits locally like a blackbody source as long as optical thickness is sufficiently high. Then the intensity of the cyclotron radiation is a direct measure of (electron) temperature. Since the magnetic field (and consequently the emission frequency $f = 2\pi\omega_c$) depends on the radius, the power spectrum represents a radial electron temperature profile.

The dependence of the spatial location of the measured data on the magnetic field inherently makes this diagnostic depend on the magnetic equilibrium reconstruction and therefore susceptible to misalignment due to equilibrium problems (see also later).

A specific advantage is the high time resolution. Its usefulness in the edge region, however, is restricted when steep gradients, typically seen in the H-mode regime, are involved. The observation in that case is a higher apparent temperature compared to the real electron temperature measured by e.g. the Thomson scattering system. This is explained by shine-through of radiation from a different radial position [31].

Another problem appears for low density plasmas. In case of finite optical depth the apparent temperature represents only a lower limit for the actual electron temperature. For the low-density experiments described in Section 5.2.1, discharges with similar configuration, identical plasma current, density and magnetic field where both Thomson scattering edge data and ECE measurements are available, were analyzed and good agreement between the data of both diagnostics is seen. This gives confidence in the measured ECE temperature profile even for rather low density plasmas.

3.3 Electron density measurements

3.3.1 Interferometry (DCN)

An important method for electron density measurements is the widely used laser interferometry [32]. At ASDEX Upgrade, a far-infrared laser interferometer is used for measuring the line integrated electron densities along several horizontal and vertical lines of sight. The conversion of line integrated data into profile information, however, requires deconvolution algorithms and is, especially at the edge, affected by reliance on separate diagnostics. Its data is in this work mainly used as an additional consistency check for the profiles of electron density measured by profile diagnostics.

3.3.2 Lithium beam (LID)

A routinely used method for measuring electron densities in the edge region of fusion plasmas is the application of lithium beam impact excitation spectroscopy (Li-IXS) [33]. The method is based on the observation of Li I radiation ($Li(2p) \rightarrow Li(2s)$ at $\lambda = 670.8\ nm$) from neutral lithium atoms injected with an energy of 15-100 keV into the plasma.

For such a beam, light emission profiles can be modeled including electron impact excitation, ionization and charge exchange processes. A system of coupled linear differential equations

$$\frac{dN_i}{dz} = \sum_{j=1}^{t} \{n_e(z)G_{ij}(T_e(z)) + H_{ij}\}N_j(z)$$

(with $N_i(z=0) = \delta_{1i}$, z is the beam coordinate, N_i occupation in the i-th energy level, t number of treated energy levels, G_{ij} and H_{ij} cover the excitation and de-excitation processes in the plasma, T_e is the electron temperature) describes the beam composition (populations in the excited states of Li) sufficiently well to reproduce measured emission profiles by varying the electron density profile in the process. In ASDEX Upgrade the time resolution is usually restricted to several milliseconds for one profile due to insufficient signal-to-noise ratio. The spatial resolution of about 5 mm is determined by the fiber optics used to transfer the emitted light to the photomultipliers for acquisition of the emission profile.

3.3.3 Thomson scattering (YAG/YAR)

The dependence of the scattered power on the electron density n_e is calculated theoretically and given by:

$$P_s/P_i = r_e^2 sin^2(\theta)n_e l S(k_F, \omega)d\omega$$

where r_e is the classical electron radius, l is the interaction length and S(k,ω) is Gaussian for a thermal plasma. This ratio is therefore directly proportional to the electron density and the Thomson system is able to measure electron densities of the same scattering volume as electron temperatures. The necessary absolute intensity calibration is done regularly at ASDEX Upgrade with Raman scattering from nitrogen gas.

Since both temperature and density are measured simultaneously at identical positions, the Thomson scattering system is specifically suited for electron pressure measurements ($p_e \propto n_e T_e$) while being independent of mapping procedures described in section 3.5.

3.4 Ion temperature measurements

3.4.1 Neutral particle analyzer (NPA)

A non-local method of determining ion temperature profiles of a fusion plasma is the analysis of energy spectra of the naturally occurring neutral particle fluxes. Due to the nature of the charge exchange process, escaping deuterium atoms carry information (energy, momentum) about the main plasma ions at the instant of the charge exchange collision. Their T_i-dependent energy distribution, which is assumed to be Maxwellian everywhere, is measured with neutral particle analyzers. At ASDEX Upgrade a multi-channel gas-cell analyzer is used for high energy neutrals (1 keV - 20 keV), while the low energy particles, especially important for the edge region, are detected by a time-of-flight spectroscopy system labeled LENA (low energy neutrals analyzer) [34]. By using a parametrization for the T_i-profile and additional plasma parameters from other diagnostics, the measured fluxes can be simulated using a Monte-Carlo neutral particle code [35]. The T_i parameters that define the profile are then varied until the calculated particle fluxes agree with the measured particle fluxes. This is done with a least squares fit method. The result is the best estimate for the actual ion temperature profile from this data. Since the inversion algorithm introduces a large uncertainty in the positioning of the steep gradient zone and because a strong influence could arise from a potential high energy tail in the ion distribution function, the method is not accurate enough, by itself, to determine T_i-profiles in the edge region [36], but can be used for consistency checks.

3.4.2 Charge exchange with neutral heating beams (CES)

A local measurement of ion temperatures exists for the core plasma, but only in discharges with neutral beam heating. It is based on analogous processes as the edge diagnostic described in Chapter 4, but the electron donors for the charge exchange recombination are the H/D-atoms from the neutral heating beams.

The captured electrons cause light emission of a Doppler-broadened spectral line. The assumption of a Maxwellian velocity distribution of the impurity ions allows the direct calculation of the corresponding temperature. The data is collected using fibre-arrays and spectrometers with CCD-cameras. The core CES at ASDEX Upgrade was not designed to explore the pedestal region in any detail but provides reliable ion temperature profiles of the core plasma.

The outermost radial channels typically measure near the steep gradient region. There, the model for the neutral beam and its geometry plays an important role, since the beam is large compared to the plasma temperature and density scale lengths. Furthermore, the separation of passive emission from active charge exchange emission is no longer possible due to the reduced difference in their temperatures. This effect is enhanced in the core system which is optimized for high throughput for the central measurements so that it has poorer spectral resolution than, for instance, the edge lithium beam system. An estimate for the outer channels is to ignore the passive signal in the fitting procedure. This assumption was confirmed experimentally with beam switching techniques and yields reasonable temperature (and density) values for all channels except the outermost one. In this last channel, the derived ion temperature and density are above reasonable values. It is possible that light from the core plasma is collected because of wall reflections. Since these effects have not yet been quantified, data from the outermost radial channel of the core system are omitted from all plots.

3.4.3 Edge charge exchange with lithium beam (LIT)

The diagnostic descriptions above show that electron temperature and density and ion temperature are measured with satisfactory detail in the core, but only the electron properties are available with sufficient accuracy in the edge plasma. The main purpose of this work is to improve this situation by providing sufficiently accurate edge ion temperatures in the steep gradient region together with a clear spatial correlation to the electron temperature as a basis for detailed theoretical analysis.

The experimental approach is to use a narrow, diagnostic neutral beam as a source for charge exchange recombination spectroscopy (CXRS) allowing local measurements with a spatial resolution of about 6 mm as described in Chapter 4.

3.5 Profile reconstruction procedure

The various measurements and diagnostic data are stored in data files (also called "shot files") together with their natural spatial coordinates. For some, these are geometric coordinates in real space, for others, like reflectometry, there is just one point of reference with real-space coordinates and the measurements are stored relative to that point

using a physical description for the distance from the reference point. The ECE has electron cyclotron frequency as its natural coordinate, which is related to real space via the spatial magnetic field B distribution as obtained by the plasma equilibrium (see next section).

When theoretical models are validated against experimental measurements, as much experimental data as is available is used to check the results. However, since different diagnostics use different natural coordinates with uncertainties and at the same time are distributed toroidally around the experiment (as shown in Figure 3.4), a common coordinate is necessary for both diagnostic cross-checks and simplification of the benchmarking of theoretical models with experimental measurements.
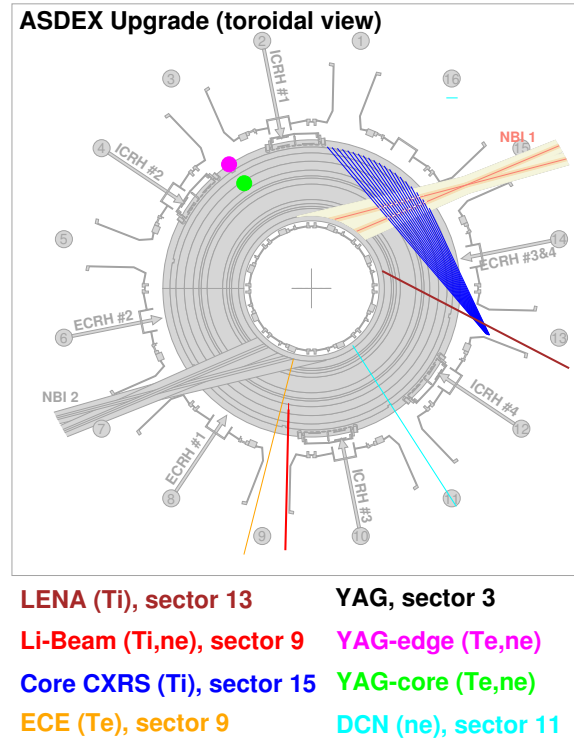
Figure 3.4: Toroidal cross section, overview of ASDEX Upgrade: Explicitly drawn are just the profile diagnostics used for cross-checks with the lithium beam edge ion temperature measurements (plotted in red, sector 9).

In the following, the generalized coordinates of normalized magnetic flux, used to describe plasmas in arbitrary magnetic configuration, are briefly discussed.

Equilibrium reconstruction and mapping

A comparison of the toroidally distributed diagnostics or complementary measurements for an improved description of the plasma profile is not possible without some simpli-

fications. The magnetohydrodynamic (MHD) theory, which uses a fluid description of the plasma, is used here for that purpose.

In an ideal MHD-equilibrium with zero net force on the plasma everywhere, the plasma pressure is balanced by the magnetic field, that is:

$$\vec{j} \times \vec{B} = \nabla p$$

Along the magnetic field lines, which wind helically around the torus and thus form closed magnetic surfaces of constant pressure ($\vec{B} \cdot \nabla p = 0$), the parallel energy and particle transport is orders of magnitude larger than the perpendicular transport. Therefore, any imbalance on such a surface is rapidly removed and plasma properties are assumed constant for all practical purposes. As such, they are only a function of the flux surface label. A common practical definition, in particular as an edge coordinate, because it is also defined outside the separatrix, is based on the poloidal magnetic flux per radian Ψ, which can be written explicitly as

$$\Psi = \frac{1}{2\pi} \int_0^R \oint_\Phi B_p d\Phi dR$$

where the integral is essentially a surface integral over the disk formed by a closed toroidal circuit on a flux surface. Using cylindrical coordinates (R,z,Φ) and assuming that the plasma is in ideal MHD-equilibrium, the poloidal flux function $\Psi(R, z)$ can be determined by numerically solving the Grad-Shafranov-Equation [37]

$$R\frac{\partial}{\partial R}\frac{1}{R}\frac{\partial \Psi}{\partial R} + \frac{\partial^2 \Psi}{\partial z^2} = -\mu_0 R^2 p'(\Psi) - f(\Psi)f'(\Psi)$$

Here $f = RB_\phi = \mu_0 I_{pol}/(2\pi)$, where I_{pol} is the poloidal current and $p'(\Psi)$ and $ff'(\Psi)$ are functions of Ψ. After Ψ is determined, the flux surfaces are simply defined by $\Psi(R, z) = const.$ and the poloidal field components are given by:

$$B_R = -\frac{1}{R}\frac{\partial \Psi}{\partial z}, \quad B_z = \frac{1}{R}\frac{\partial \Psi}{\partial R}$$

Further simplification is achieved by normalization of the flux to the total magnetic flux in the confined plasma region, that is, up to the separatrix. The coordinate used on most profile plots later on is $\rho_{pol} = \sqrt{\frac{\Psi - \Psi_0}{\Psi_s - \Psi_0}}$, where Ψ_0 is the flux at the magnetic axis and Ψ_s is the value of Ψ at the separatrix (last closed flux surface). The square root is introduced to transform the resulting coordinate, which is about proportional to a cylindrical volume, to a more linear behavior across the radius. The normalization is chosen so that $\rho_{pol} = 0.0$ at the magnetic axis and $\rho_{pol} = 1.0$ at the separatrix. The full solution of this boundary condition problem is done in a complex inversion process [37],

which is performed for each ASDEX Upgrade discharge.

With the definition of flux surfaces it becomes possible to assign each spatial data point with the respective natural coordinate its value of normalized magnetic flux. This process is called "mapping to flux surfaces". It is a one-way process, since two-dimensional information (height and major radius/magnetic field) is substituted by the one-dimensional coordinate called "normalized flux". While poloidal magnetic flux is also defined outside the separatrix, on the field lines intersected by walls, considerable gradients may occur parallel to $\vec{B}$. This has some implications for modeling, but won't be discussed in more detail.

3.6 Improvement of profile comparisons

The Thomson scattering system [12] measures simultaneously electron density and temperature at the plasma edge. The two lithium beam diagnostic systems determine electron density and ion temperatures on the same flux surfaces, but nearly 180 degrees away from Thomson in toroidal direction (compare with Figure 3.4). Using electron density as the common coordinate of the two diagnostics, it becomes possible to compare electron temperature (from Thomson scattering) and ion temperature (from lithium beam charge exchange) without the need for a mapping to flux surfaces.

Since the flux surface curvature in the outer midplane region (where both lithium beam and Thomson edge scattering collect their data) is low and the near vertical flux surfaces are rarely affected by equilibrium reconstruction problems, inconsistencies only occur, if the real space radial coordinates are displaced relative to each other. Such shifts ($\lesssim 1$ cm) do indeed occur due to diagnostic misalignments or vessel asymmetries, but this can be corrected for by applying adequate radial shifts before performing the mapping onto flux surfaces. Corrected profiles in the ρ_{pol} coordinate are determined by radially shifting the electron density profiles (together with the respective temperature profiles) of both diagnostics relative to each other until the mapped electron density profiles match. This is easier to do and achieves the same goal. Moreover, it can be applied also to diagnostics sharing measurement positions, if profile extrapolation or increased spatial resolution provided by a separate diagnostic is desired. The tool used for this diagnostic combination procedure at ASDEX Upgrade is AUGPED.

3.6.1 AUGPED

AUGPED is an IDL® based program written for the purpose of determining pedestal properties by applying a modified hyperbolic tangent fit (see below) to the combined data of several edge (and core) density and temperature diagnostics. AUGPED reads the data of many ASDEX Upgrade diagnostics (T_e, T_i, n_e) along with their natural coordinate. It also uses a selectable magnetic equilibrium and maps data to the common

coordinate, in general the normalized poloidal magnetic flux radius ρ_{pol}. It can do arbitrary radial shifts of each individual data set before applying the mapping. The profiles are always plotted with ρ_{pol}, but internally the program uses a real space coordinate on the outer midplane (unit: m) for the shifts. The shifts are there to improve the resultant global profile and are based on empirical knowledge of certain diagnostic peculiarities, mostly calibration errors of a diagnostic's absolute position. A lot of effort is spent to track down such systematic errors of diagnostics and AUGPED has been and still is a successful and appreciated tool for that purpose.

The left plot of Figure 3.5 shows the raw edge density data of the ohmic standard discharge (also used in Chapter 5) without any shifts applied. After fixing the position of one diagnostic (in this case: YAR at a nominal position of +6 mm) the shift of which is determined by an additional boundary condition (e.g. separatrix temperature), the other diagnostics can be aligned using AUGPED. The right plot of Figure 3.5 illustrates this showing the corrected profiles after the appropriate shifts have been applied. The temperature profiles (T_e for YAR and T_i for the lithium beam system) for this same discharge have been shifted with the same relative offsets as determined by the density comparison. The final result for temperatures can be seen in Figure 5.2 in Chapter 5.
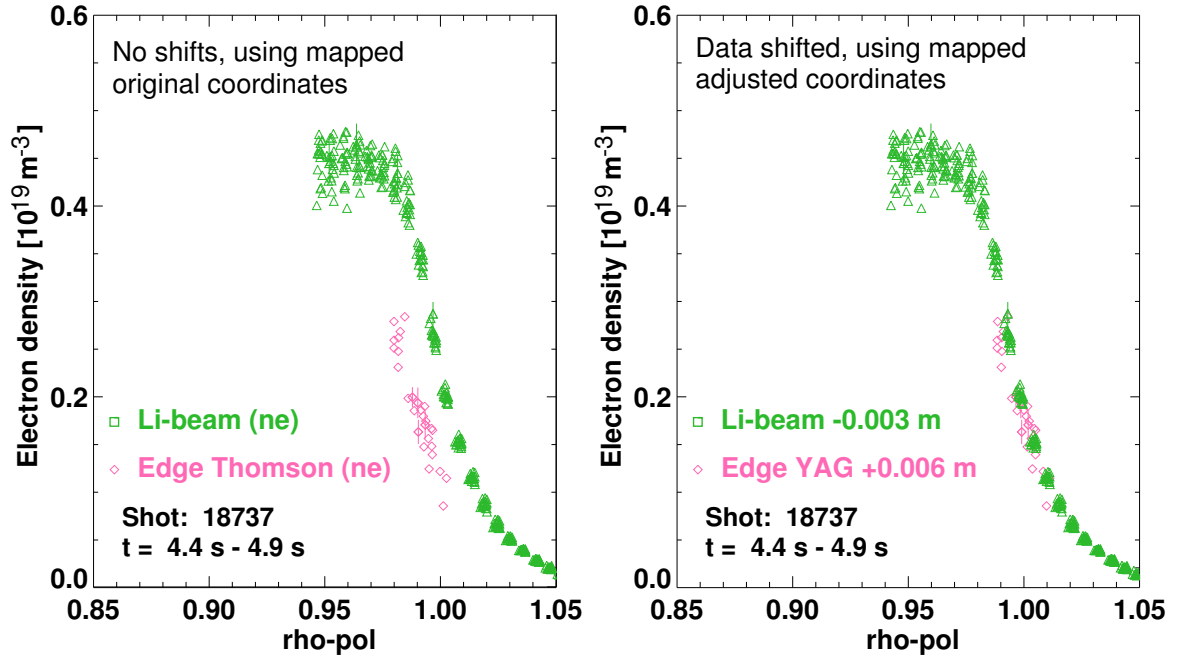
Figure 3.5: Unavoidable calibration errors or vessel asymmetries lead to radial offsets of measurements that are quite obvious, but need to be corrected for constructing globally consistent profiles. In the left figure, the data of LID and YAR measurements without any adjustments are shown with standard mapping to normalized poloidal flux applied. The right figure includes correction of +6 mm for YAR and -3 mm for LID, respectively, before mapping to ρ_{pol} is done.

The data are read based on shot number and time window with the possibility of synchronizing to ELM events. Since certain well diagnosed discharges are identically repeated for completing the diagnostic information (e.g. Thomson scattering at the edge and in the core plasma, different impurities for ion temperatures, etc.), an option is given to load data from different discharges and time windows as well. After the data are read, they are mapped using the specified equilibrium and displayed awaiting manual corrections. These involve the above mentioned radial shifts, but also exclusion of part of the data (because of a technical failure affecting only part of a diagnostic, e.g. a single laser of the Thomson system) and an option of not using a diagnostic at all (e.g. when a companion discharge with better calibrated data and thus smaller uncertainties exists). Once the data set is complete, the modified hyperbolic tangent:

$$F(x) \;=\; \frac{a_0 + a_1}{2} + \frac{a_1 - a_0}{2} \; \frac{\alpha_1(\xi) \, e^{\xi} - \alpha_2(\xi) \, e^{-\xi}}{e^{\xi} - e^{-\xi}} \tag{3.1}$$

where

$$\xi(x) \;=\; \frac{a_2 - x}{a_3} \tag{3.2}$$

$$\alpha_1(\xi) \;=\; 1 + a_4 \xi + a_5 \xi^2 + a_6 \xi^3 \tag{3.3}$$

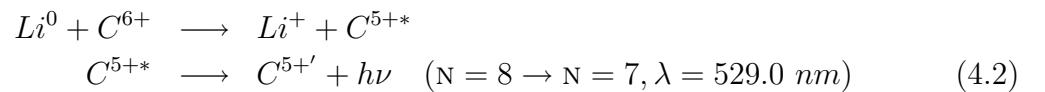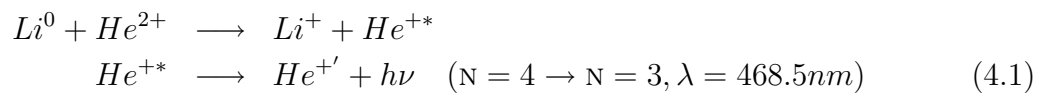$$\alpha_2(\xi) \;=\; 1 + a_7 \xi + a_8 \xi^2 + a_9 \xi^3 \tag{3.4}$$

adapted from [38], is fitted to the data and displayed on top of the raw data. The specific choice of the fitting function provides a good match to typical edge profiles and is also used for international inter-machine comparisons. Most of the plots presenting data and fitted profiles in Chapter 5 were created using AUGPED.

4 Lithium beam ion temperature measurements -
Experimental setup and method

Ion temperature measurements based on thermal Doppler-broadening of spectral line emission can in principle be accomplished in a fully non-perturbing way. However, the deconvolution of several line integrals leads to uncertainties about the exact location of the measured temperatures. In order to avoid these problems, local interaction with laser or particle beams is an appropriate measure. The intersection point of line-of-sight and beam can be accurately determined and thus reduces the positioning error considerably. Since the beam intensity is low, the resulting plasma perturbation is negligible. Moreover, chopping the beam allows simple and accurate background subtraction.

4.1 Charge exchange recombination spectroscopy (CXRS)

The method of CXRS [39], in this work using a lithium beam, is utilized to measure ion temperatures of fully stripped carbon and helium. All measurements are based on the following charge exchange reactions:

$$
\begin{aligned}
Li^0 + He^{2+} & \longrightarrow & Li^+ + He^{+*} & \\
He^{+*} & \longrightarrow & He^{+\prime} + h\nu & \quad (\text{N} = 4 \to \text{N} = 3, \lambda = 468.5nm) \quad (4.1) \\
Li^0 + C^{6+} & \longrightarrow & Li^+ + C^{5+*} & \\
C^{5+*} & \longrightarrow & C^{5+\prime} + h\nu & \quad (\text{N} = 8 \to \text{N} = 7, \lambda = 529.0\ nm) \quad (4.2)
\end{aligned}
$$

Carbon is chosen because it is one of the main low-Z impurities in ASDEX Upgrade due to the wall coverage with graphite tiles. Despite the ambitious tungsten wall program on ASDEX Upgrade, there are still large carbon sources in the vessel [40]. Furthermore, Li-C charge exchange cross sections for reactions involving visible line emissions (in particular C VI) are found to be rather high [41] in comparison to other potentially viable impurities. Since helium is used for inter-shot glow discharge cleaning, residual amounts of helium in the order of several percent can be expected in every discharge even without an external source. At this level, the dominating ion species is still deuterium but helium

becomes an important alternative to carbon for ion temperature measurements in most plasma scenarios. Other impurities like boron, oxygen or higher-Z noble gases are less abundant.

The dominant broadening mechanism for the observed spectral lines is the thermal ion motion and the corresponding statistical emission of Doppler shifted photons. Assuming a Maxwellian velocity distribution $f(v)$ where

$$f(v) \quad \propto \quad \exp\left(-\frac{mv^2}{2k_BT_i}\right) \tag{4.3}$$

the spectral intensity distribution $I(\lambda)$ forms a Gaussian with

$$I(\lambda) \quad \propto \quad \exp\left(-\frac{(\lambda-\lambda_0)^2}{2\varsigma^2}\right) \tag{4.4}$$

and therefore, assuming $\Delta\lambda/\lambda \approx v/c$, its width ς is related to the temperature as:

$$\varsigma \quad = \quad \lambda \cdot \left(\frac{k_BT_i}{mc^2}\right)^{\frac{1}{2}} \tag{4.5}$$

If the assumption of a Maxwellian velocity distribution of the light-emitting ions holds, the derived ion temperature depends only on the width of the measured Gaussian. Therefore this method is robust against photon flux variations because absolute intensity calibrations are not required.

4.1.1 Heat exchange between impurities and main plasma

Since the measurement of main plasma ion temperatures is desired, but the presented method measures ion temperatures of trace impurities, the usual assumption that the temperatures are similar needs to be justified. When a main plasma temperature is defined, the particles have assumed a Maxwellian velocity distribution. The relevant time scale for this is the heat exchange time (also called equipartition time) of a small sample with the background field ions. The calculation of the characteristic heat exchange time for two species (i and j) at different temperatures is done by calculating the energy transfer of a test particle and integrating over the whole distribution. The general formula [3] is

$$\tau_{EX}^{ij} = \frac{3\sqrt{2}\pi^{3/2}\varepsilon_0^2 m_i m_j}{n_j e^4 Z_i^2 Z_j^2 \ln\Lambda}\left(\frac{T_i}{m_i}+\frac{T_j}{m_j}\right)^{3/2} \tag{4.6}$$

with m being the mass, Z the ionization state, T the corresponding temperature — assuming a Maxwellian distribution for both species — and n the particle density. $\ln\Lambda$

is the density and temperature dependant Coulomb logarithm, which accounts for the many small angle collisions, which constitute the dominant contribution to the total scattering cross section in a fusion plasma.

Assuming an equilibrated background plasma (see also Section 2.3.2) and looking at the energy equilibration time between test particles or small samples of plasma at a different temperature with the background, one sees that $\tau_{EX}^{ij} \propto m_i/Z_i^2$. Using the timescale of D-D heat exchange, $\tau_{EX}^{D,D} \propto m_D$, as a reference, it is apparent that samples of helium $(m_{He}/Z_{He}^2 = 2m_D/(2Z_D)^2 = \frac{1}{2}\tau_{EX}^{D,D})$ or carbon $(m_C/Z_C^2 = 6m_D/(6Z_D)^2 = \frac{1}{6}\tau_{EX}^{D,D})$ equilibrate on shorter timescales with a given background distribution than deuterium itself. Unless impurity transport is strongly different from the background particle transport, the impurities will assume the background temperature earlier than the co-transported hot or cold deuterium particles.
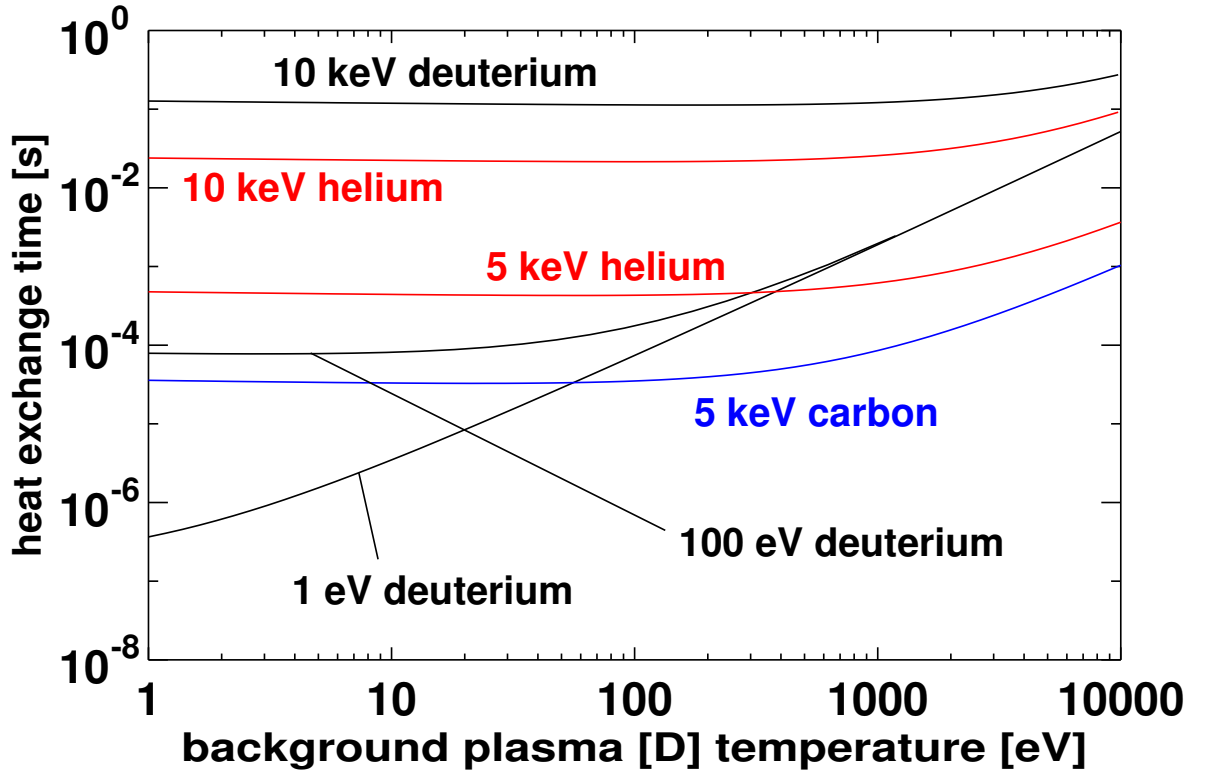

Figure 4.1: Heat exchange times from collisions at a density of $n = 10^{19}$ m^{-3} for deuterium (D$^+$), carbon(C^{6+}) and helium (He^{2+}). Unless impurity transport exceeds main plasma transport substantially, the impurity ions will equilibrate faster with the background than co-transported deuterium because $\tau_{EX} \propto m/Z^2$. Thus, the measured impurity temperature always reflects the main plasma temperature, if deuterium itself is equilibrated to a Maxwellian velocity distribution.

Figure 4.1 shows examples for the extreme cases, where heat exchange times have been

calculated with equation (4.6) using a background of deuterium and samples of deuterium, helium and carbon. The results are plotted versus the background temperature. The faster equilibration of impurities compared to deuterium is immediately obvious (deuterium at 10 keV, helium at 10 keV). The hypothesis that hot impurities could flow into cold background regions and falsify the measurements might only apply if the impurity ion transport is substantially higher than the main ion transport. Considering the low (compared to measurement times) absolute numbers, this impurity flux would have to persist during the whole measurement period and thus transfer a substantial amount of energy to the deuterium ions until a new equilibrium at higher temperature is established. Carbon is not critical in this respect due to the high Z, and helium transport in the core is observed to be rather low [42]. Problematic fluxes of hot helium ions are thus not expected, at least not for a not ignited plasma.

Another possible error source are cold impurity atoms penetrating from the SOL into the gradient zone. While the heat exchange times are short enough to equilibrate the particles, once they are ionized, a large neutral penetration and fast local ionization may lead to an impurity temperature below the main plasma temperature. The ionization time can be estimated from ionization rate coefficients S [43] and the local plasma parameters. Assuming $n = 3 \cdot 10^{19}$ m^{-3} and $T_e = 300$ eV, $\tau_{ion} = 1/(nS(T)) = 10^{-5}$ s. From equation (4.6) one gets $\tau_{EX}^{He,D} \approx 6 \cdot 10^{-5}$ s for helium at room temperature (≈ 0.05 eV), which could lead to the unfavorable situation of unequal temperatures. However, thermal helium with a velocity of about 1000 ms^{-1} does not penetrate far enough because the $He^0 \rightarrow He^+$ ionization rate is $\geq 10^{-14}$ m^3 s^{-1} for $T_e \geq 50$ eV and thus the penetration depth λ_p of neutral helium beyond the separatrix, where the typical electron density is $n_{sep} \approx 2 \cdot 10^{19}$ m^{-3}, amounts to $\lambda_p = v_{th}/(nS) \leq 1$ cm. In H-mode, where the gradient scale length can be of this order, the higher separatrix temperature (roughly 100 eV) and accordingly higher SOL values keep neutral helium away from closed flux surfaces.

Finally, transport processes could bring cold ionized helium into the gradient region, thus making the measurements arguable. Typical particle transport times for steep H-mode gradients with $L_n < 1$ cm are potentially of the same order as equilibration times due to high postulated diffusivities for He at the plasma edge. Since the steep gradients are typically accompanied by a transport barrier which reduces the diffusion coefficient D, appropriate numbers for D_{He} are difficult to estimate. Assuming $D_{He} \approx 1m^2/s$ as an upper limit, the transport time calculates to:

$$\tau_{transp} = \frac{L_n^2}{D} = \frac{(0.01\text{m})^2}{1\text{m}^2\text{s}^{-1}} = 10^{-4} \text{ s} \gtrsim \tau_{EX}^{He,D} \qquad (4.7)$$

The equilibration will therefore likely be fast enough to justify the assumption of $T_{He} = T_D$ even under H-mode conditions, but caution is necessary. Carbon is fully ionized only at higher temperatures and not subject to the edge penetration issue.

4.2 Experimental Setup

4.2.1 The Li-beam — a local source of charge exchange electrons

At ASDEX Upgrade, a neutral lithium beam [44] is used for edge plasma analysis (Figure 4.2). Its main parts are the emitter (tungsten surface coated with Li-doped β-eucryptite), which is heated ohmically to produce lithium ions, the accelerator, where the ions are collimated to a narrow, almost parallel beam, a charge exchange cell, where the fast ion beam is neutralized and deflection plates just in front of the neutralizer. The plates are used to chop the beam every 80 ms for a variable time of typically 15-25 ms by applying a voltage of about 1 keV, which prevents the beam from entering the plasma. The device is completely surrounded by iron plates acting as a shield against magnetic fields. The neutralizer can be operated with sodium at about 250°C and 80 % neutralization efficiency or potassium at about 170°C. With potassium, due to high total charge exchange cross sections, neutralization efficiency reaches almost 100 %. However, long-term operation with potassium was not possible due to arcing inside the device which seems to be catalyzed by chemical bonds of insulating material with vaporized potassium. The fast beam can be operated at up to 100 kV acceleration voltage and extracts a current of typically 2.4 mA at 40 kV from the emitter, which is the default setting for a reasonable compromise between sufficient beam penetration and a high neutralization efficiency.

The horizontal beam enters the plasma 32.6 cm above the tokamak midplane at a toroidal angle of 10 degrees. The length of the beam-plasma interaction region (about 5-15 cm), after which the beam intensity falls below the detection limit due to ionization of beam atoms, depends on the electron density. It is observed by two optic heads with a focusing lens in each. At the beam elevation they cover about 20 cm radially for access to edge data for various plasma geometries, with the exact observation region also depending on the plasma shape (see Figure 4.3).

One optic head (Li-IXS), consisting of 35 fibers, has a top down view of the plasma edge gradient region and is used for electron density measurements by means of impact excitation spectroscopy, recording $Li(2p) \rightarrow Li(2s)$ line emission ($\lambda = 670.8nm$) with filter-photomultipliers.

The second optic head, primarily used for the ion temperature measurements in this work, consists of an array of fibres (arranged in two adjacent rows, with a total of 55 operable lines-of-sight). It is directed mostly poloidal looking from below onto the beam axis with a spatial resolution of 6 mm. Its fibres for the visible light range end at a switchboard, where several optical diagnostics can be connected for plasma observation. The relative spatial coordinates of those two optics can be very well aligned by in-vessel calibration. Therefore, it is possible to measure simultaneously $T_i(r)$ and $n_e(r)$ at the same toroidal and poloidal position. This is helpful for comparing the measurements to other diagnostic data.
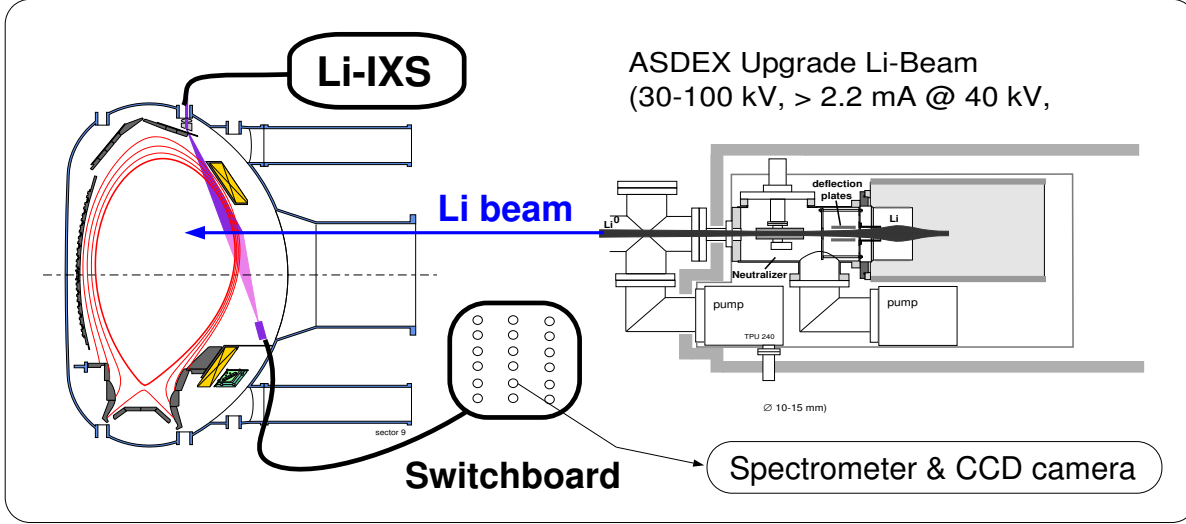
Figure 4.2: Schematic cross section of experimental setup at ASDEX Upgrade and the lithium beam injector (drawn at a different scale). The diagnostic lithium beam enters the plasma after extraction from a cathode, focussing and neutralization. The beam-plasma interaction region is observed by a Li-IXS (impact excitation spectroscopy) optic for electron density measurements and a second optic, connecting to a flexible switchboard, mainly used for CXRS edge ion temperature measurements.

4.2.2 High resolution spectrometers for spectral line analysis

Two independent detection systems presently use this switchboard to record the light observed by the optic head. One of these, also employed in [45], consists of a Czerny-Turner spectrometer (JOBIN YVON 750M, f=0.75m, 1200 g/mm grating) and a fast, back-illuminated frame-transfer CCD[1] camera (Roper Scientific MicroMax:512BFT), with 512×512 pixels. Its time resolution is restricted only by its readout time, which depends on the number of concurrently recorded channels (max. of 10 with 400 μm fibres) and the spectral window used. Exposure times down to 3 ms are possible by reducing the number of channels and spectral range. The CCD chip is Peltier-cooled to below $-45°$C and has a high photon quantum efficiency ($\approx$ 0.8) resulting in a low noise level.

The second system was originally based on a ProScan CCD camera with image intensifier, attached to an ACTON spectrometer (Czerny-Turner, f=0.75m, 1800 g/mm grating). Since the noise caused by the amplification prevents high quality data, the CCD of this system was upgraded to a Micromax system with identical features as the camera installed with the JOBIN spectrometer. The maximum number of channels on that system, however, is only 8 due to a slightly different spectrometer geometry.

In summary, with the current setup it is possible to measure with up to 18 simultaneous and independent ion temperature channels at a spatial resolution of 6 mm and a time
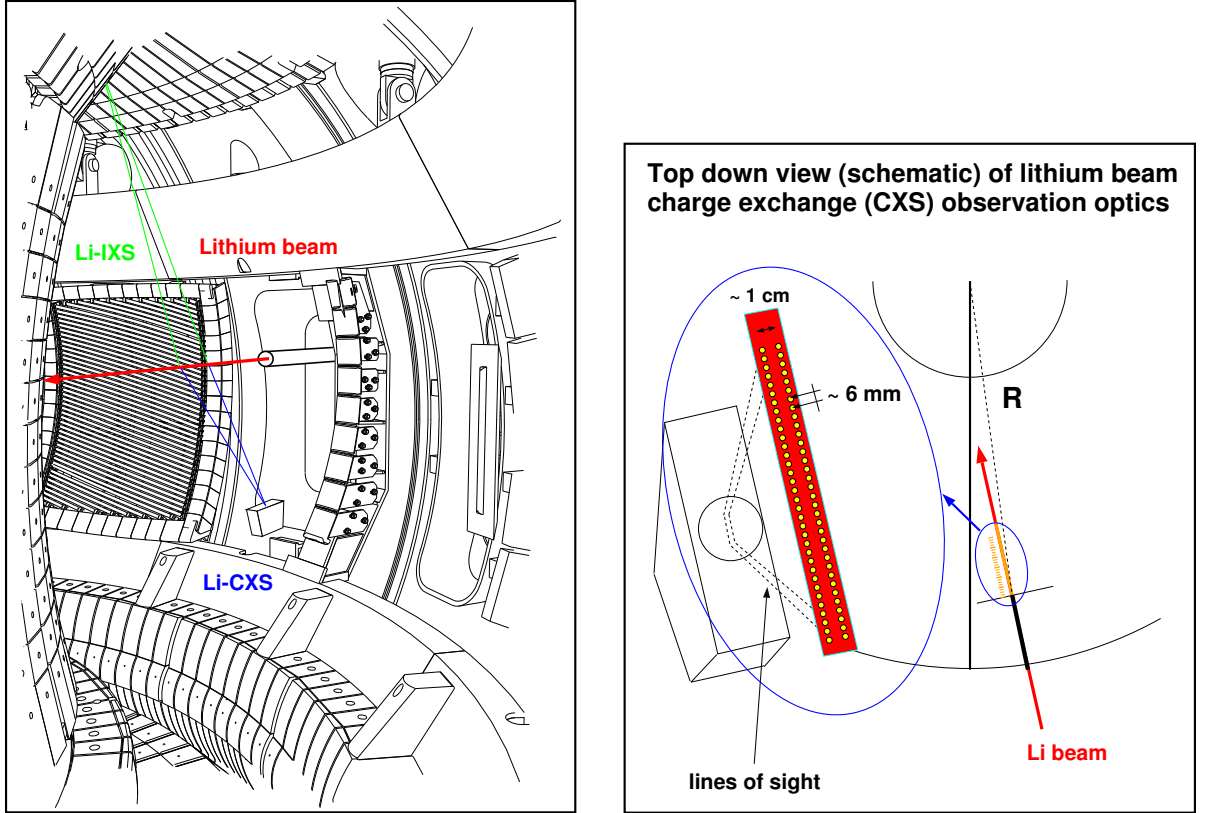
---

[1]CCD: charge coupled device

Figure 4.3: 3D view of ASDEX Upgrade vessel with schematic Li-beam and lines of sight for electron density measurement (by Li-IXS) and ion temperature measurements (Li-CXRS) (left). Crude sketch of CXRS observation optics with two rows of fibres with ≈ 6 mm resolution in radial (=beam) direction as seen from the top (right).

resolution of up to 100 ms. The time resolution is mainly determined by the chopper frequency and could be improved if the signal-to-noise ratio (SNR) were to be substantially increased, but this is limited by the achievable beam intensity.

4.3 Data processing

4.3.1 Background of utilized transitions

In all discharges, impurity line-radiation is clearly visible due to electron excitation, free electron recombination and charge exchange with neutral atoms. In fact, due to the limited lithium beam current, these background processes, integrated over the full line-of-sight, outshine the localized beam-induced charge exchange recombination radiation by far (in L-mode typically factors of 5-20 for the C VI line; about the same factors in
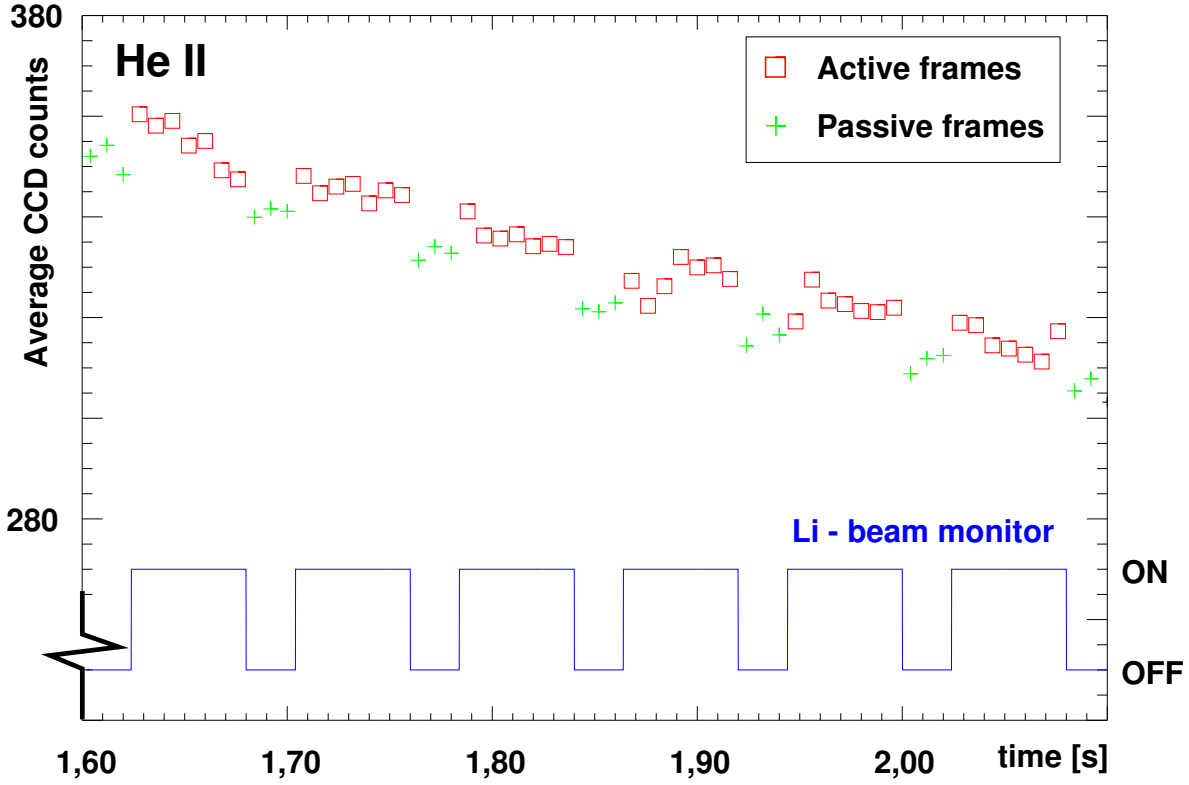
Figure 4.4: Time trace (with suppressed zero) of the (spectrally averaged) signal for the He II emission from an ohmic plasma (discharge #17799, single frame exposure time: 8 ms). Crosses indicate CCD frames with deflected beam ("passive signal", background) while rectangles show the signal of CCD frames with enabled lithium beam which includes charge exchange ("active signal"). The total signal level is decreasing with time, which may be caused by a decreasing He$^+$ concentration. The signal drift caused by background emission may even exceed the net charge exchange component.

the wings of the He II line and up to a factor of 70 near the central wavelength, mostly by radiation from a cold (< 50 eV) He^{1+} population) in the SOL.

The solution to deal with this is a periodic (every 80 ms) chopping of the diagnostic beam by applying a voltage of about 1 kV to lateral plates placed in front of the neutralizer which deflect the beam, effectively switching it off. Therefore the assumption of constant plasma conditions over at least 100 ms becomes necessary for the measurements. The signal during phases with deflected Li-beam ("beam off") is called "passive signal". The line shape and intensity of this background signal are strongly influenced by impurity density, electron density, flux of neutrals and other plasma parameters along the whole line-of-sight. Phases where lithium beam charge exchange emission is present as well ("beam on") are called "active signal". The spectra to be used for the localized

ion temperature measurements, i.e. the difference between "on" and "off", are referred to as "net signal" or "net spectra".

The spectrometer cameras are synchronized to the chopping and a series of active and passive frames are recorded in each discharge. Since the noise from the cameras on both passive and active signal is low due to cooling the chips to $-45°$C, photon statistics dominates the uncorrelated noise in each pixel. There is a second source of pixel noise, which is correlated over a range of pixels (affects the full spectral line), since it is induced by effects in the plasma: density fluctuations, plasma movement or impurity concentration changes.

The calculation of the net signal, which is done by subtracting an average passive spectrum (taken from the passive signal just before and just after the active phase) from the average active spectrum, involves the difference of large numbers with uncertainties $\propto \sqrt{N}$, where N is the number of measured photons. Moreover, since active and passive signal are not recorded simultaneously, but sequentially, the assumption of stationary plasma parameters during at least one chopping cycle induces further noise because fluctuations are present. In practice, there are cases where the global plasma parameters (e.g. T_e, n_e) are constant, but an influx or efflux of impurities changes the intensity of the background signal by a substantial amount with a slow time constant (see Figure 4.4). This is automatically corrected by the procedure described here. In H-modes, density fluctuations (e.g. from ELMs) are a source of strong correlated noise, especially for helium (Figure 4.9, right).

The empirical statistical error is directly measured by calculating the standard deviation from the mean in each pixel separately. While the bandwidth of the total uncertainty is correctly measured by this empirical sampling, the correlated part of the noise appears in the spectra as large error bars although the pixel-to-pixel scatter is comparatively low. The plotted net spectra always display error bars that include this correlated noise from the plasma fluctuations.

In summary, the proper removal of background radiation is done by calculating a net spectrum for each beam chopper cycle by averaging the signal from the passive phase before and after the relevant active phase and subtracting it from the averaged active signal. Depending on the plasma regime and lithium beam performance, a time integration of order seconds can be necessary to create spectra that reduce the uncertainty for the Gaussian width (determined from the standard deviation returned by the fit routine) below $\approx 10\%$ of the total width. This time integration is done by averaging all single net spectra in the full time interval and in the process determining the statistical error in each spatial (i) and each spectral (j) channel by standard error progression. The errors via the standard deviation from the mean σ_{ij} are passed on as weights $w_{ij} = 1/\sigma_{ij}^2$ for the fit routine.

4.3.2 Profile fitting

After the local net spectrum is calculated, its Gaussian width must be determined. The ratio of the spectral line width of this Li-beam induced net spectrum to the average passive spectrum and the total intensity of these signals can vary strongly from one spatial channel to the next, depending on the specific plasma regime as well as the impurity, as discussed in the next section. Therefore, a number of different approaches were tried.
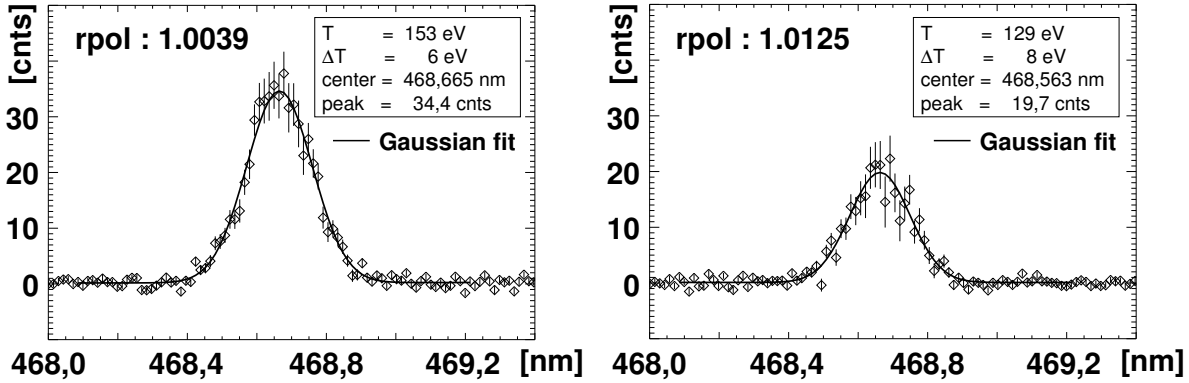

Figure 4.5: Net spectra are fitted with a Gaussian model to determine the line width which — after some corrections (see section 4.3.3) — is a direct measure of the radiating ion species' temperature. The uncertainty ΔT is calculated from the standard deviation of the weighted fit's result for the line width. Typical fits of He II spectra from an ohmic plasma discharge are shown.

- Standard least squares fit of a model function with a single Gauss on top of continuum $C(\lambda)$, which can be assumed constant or linear in λ.

$$I(\lambda) = A_0 \cdot \exp\left(-\frac{(\lambda - A_1)^2}{2A_2{}^2}\right) + C(\lambda) \tag{4.8}$$

$$C(\lambda) = B_0 + B_1\lambda + B_2\lambda^2 \tag{4.9}$$

The continuum usually vanishes and is included only for cases where strong impurity radiation from different spectral lines may create a tilted baseline because of fluctuations and this may influence the fit of the Gaussian, if not taken into account.

- The observed large standard deviation from a mean despite negligible pixel to pixel scatter has motivated a variation from the above procedure. Since the plasma fluctuations cause a collective scatter of the cold background region (narrow spectral region around the central wavelength), a procedure applying a direct correction

of this part of the net signal was attempted. A least squares fit uses the same model as above, but an additional correction for any remaining passive component is done iteratively by correlation analysis in the following way: Let $act(\lambda)$ be the active spectrum, $psv(\lambda)$ the passive spectrum and $net(\lambda) = act(\lambda) - \gamma \, psv(\lambda)$ the data to fit, where $\gamma = 1$ for the first iteration. $net(\lambda)$ is fitted to the designated model and $fit(\lambda)$ is acquired. γ is then subsequently adjusted by calculating a correlation coefficient between the remainder $rem(\lambda) = net(\lambda) - fit(\lambda)$ and the passive component $psv(\lambda)$.

$$Correl(rem, psv) = \frac{\int (rem(\lambda)psv(\lambda))}{\int (psv(\lambda)^2)} \tag{4.10}$$

The correlation function was chosen to calculate a normalized value for the similarity between remainder and passive signal. After each iteration, γ is adjusted to $\gamma = \gamma + \epsilon \cdot Correl(rem(\lambda), psv(\lambda))$, where ϵ is a variable parameter between 0 and 1, determining the desired rate of convergence. As soon as $Correl(rem, psv)$ drops below a predefined threshold, the routine is stopped. If the threshold is not reached within a certain number of iterations (typically 40), the process would usually run forever, jumping between two states not compatible with the set boundary conditions. In that case, the procedure is interrupted and the standard fit is applied.

- When the fitting of a single Gaussian distribution is not successful, consideration of a second, well-defined ion temperature may become appropriate. This leads to the application of a double Gauss model with some continuum $C(\lambda)$.

$$I(\lambda) \;\; = \;\; A_0 \cdot \exp\left(-\frac{(\lambda - A_1)^2}{2A_2{}^2}\right) + A_3 \cdot \exp\left(-\frac{(\lambda - A_4)^2}{2A_5{}^2}\right) + C(\lambda) \;\; (4.11)$$

Temperatures can then be determined separately for both Gaussian widths, but the interpretation is difficult. Since the background with its high intensity can not be completely removed despite the chopping, one width often just resembles an average temperature of the incompletely removed passive component.

- The double Gauss model can also be combined with the iterative approach to minimize distortion by background light. Using the two temperature model as above, the same iterative minimization of the correlation between remainder and passive signal is possible. Due to the large number of fit parameters, some numerical issues with the fit and the exact implementation of the fitting procedure, the routine doesn't improve upon the other methods. Since there are no constraints on the fit parameters, numerically there is always the possibility of introducing a second Gaussian with low intensity, which improves the quality of the fit numerically but doesn't reveal any realistic physics. A plasma with a distribution compatible with two Maxwellian ion velocity distributions, the temperatures of which are both

different from the average background signal temperature, has not been seen.

All fits are done using the IDL® "curvefit" procedure, which uses a gradient-expansion algorithm to compute a non-linear least squares fit to a user-supplied function with an arbitrary number of parameters. Since the first method does not need many parameters which simplifies the comparison of different scenarios and at the same time reliably produces adequate fits, it was the preferred method for all evaluations. The iterative approach generally produced the same results with marginally reduced fit errors but considerably more time and effort, so it was only used for consistency checks. The same is true for the multi-gauss fits. An example for the fit to raw data is shown in Figure 4.5.

4.3.3 Correction of systematic errors

The measured spectral line shape is affected by non-thermal broadening for multiple reasons. The main influence comes from the instrument itself, i.e. mainly from the spectrometer entrance slit. This has been investigated using spectral lines from Hg and Ne light sources, for which the natural line width was assumed to be a delta function. The measured instrumental response resembles a Gaussian profile. Interpreting this profile as a temperature with the wavelength dependence of the spectrometer and the element's mass taken into account, it equals a characteristic "instrument temperature" of about 23 eV for He (He II at 468.5 nm) and 54 eV for C (C VI at 529.0 nm) for a slit width of 100 μm (calculated using equation (4.5)). Thus, the influence of the instrument can be approximated by a convolution of the source with a Gaussian profile. Since the source is also well described by a Gaussian shape, this convolution results in another Gaussian, whose width is just the quadratic sum of the two initial widths (σ_1 and σ_2).

$$f, g \;=\; \frac{1}{\sigma_{1,2}\sqrt{2\pi}} \exp\left(-\frac{(\lambda - \lambda_0)^2}{2\sigma_{1,2}^2}\right) \tag{4.12}$$

$$f \star g \;=\; \int_{-\infty}^{\infty} f(\tau)g(t - \tau)d\tau$$

$$=\; \frac{1}{\sqrt{2\pi(\sigma_1^2 + \sigma_2^2)}} \exp\left(-\frac{(\lambda - \lambda_0)^2}{2(\sigma_1^2 + \sigma_2^2)}\right) \tag{4.13}$$

The deconvolution of a Gaussian instrument function from such a Gaussian spectrum simplifies to subtracting the predetermined "instrument temperature" from the measured apparent temperature.
Further broadening effects occur naturally due to the sub-structure of the atomic levels and have to be accounted for as well. Due to the coupling of magnetic moments (orbital and spin angular momentum) to each other (**LS**-coupling) or to an external field

(Paschen-Back), electron states at identical principal quantum number but different angular momentum quantum number have different energy levels and therefore transitions from different electron states (distinguished by their sub-state quantum numbers **L** and **J** ($\vec{J} = \vec{L} + \vec{S}$)) emit light at different wavelengths. If all charge exchange electrons radiated from a single state, the line broadening were only thermal. In case of collisional redistribution of states before the spontaneous emission, the observed spectral line is broader due to the overlap of radiation from several sub-states.

Since the charge exchange process has different cross-sections for different sub-states, the relevant configuration for calculating a total line emission is not easily determined, but depends on the physics of the charge exchange process. The amount of redistribution (**L**-level mixing) depends on plasma parameters like temperature and density, while the magnetic field influences the magnitude of the applicable wavelength shift for the different sub-states (Zeeman-broadening). Since both effects occur simultaneously, it is difficult to separate them. Instead, an integrated approach using parts of the Atomic Data and Analysis Structure (ADAS) package is applied.
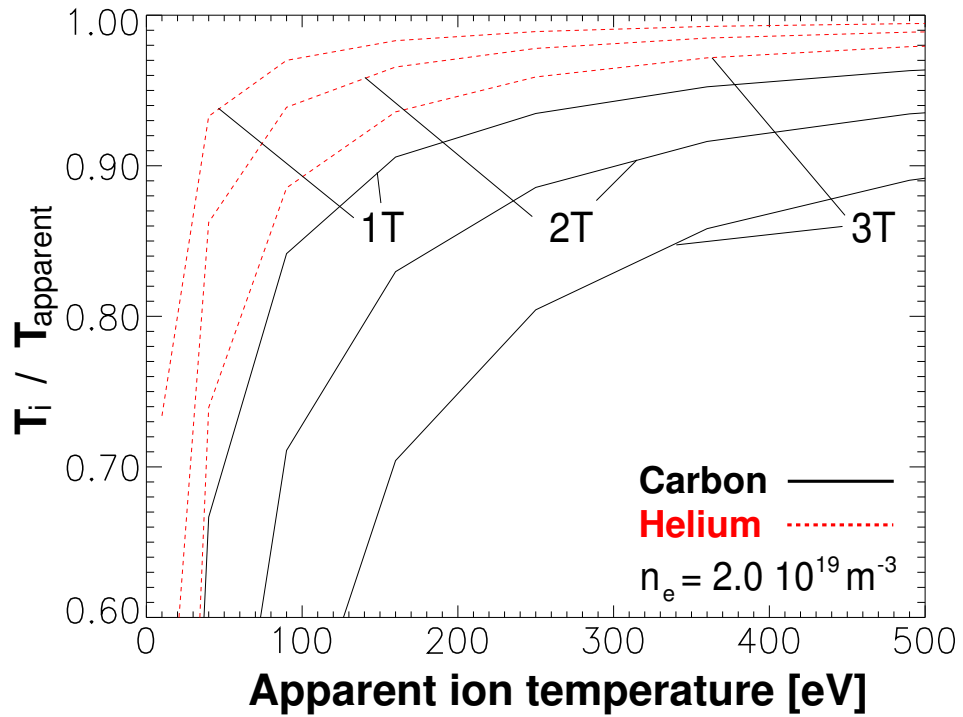

Figure 4.6: A survey, with synthetic input data for the ADAS calculations used to accurately determine non-thermal broadening effects (Zeeman and **L**-level mixing), shows that helium ($\lambda = 468.5\ nm$, $4 \rightarrow 3$ transition) is much less affected than carbon ($\lambda = 529.0\ nm$, $8 \rightarrow 7$ transition). Plotted are the relative magnitudes of the actual ion temperature divided by the apparent temperature for both impurities at several different magnetic fields over the apparent temperature (as calculated from an uncorrected spectrum).

The ADAS package is a collection of programs and data for modeling the radiative properties of ions and electrons in plasmas, which assists in the interpretation of spectral measurements (http://adas.phys.strath.ac.uk/) [43]. Among others, there is a package for calculating **LJ**-resolved[2] emission coefficients and electron populations after charge exchange from neutral beams (ADAS306) and a package for spectral analysis (ADAS603), which contains a subroutine that calculates absolute line strengths including the influence of the magnetic field. The algorithm for calculating these line strengths was developed by Hey (see e.g. [46, 47]).

Plasma properties, defined by the magnetic field, electron density, electron temperature and a first estimate for the ion temperature as well as the appropriate lithium beam parameters (energy, beam ion) are entered into ADAS306 which returns **LJ**-resolved emission coefficients and electron populations for the individual states. These are used as weights for the results of the ADAS603 subroutine, which calculates the line strength of the individual transitions including information about the angle between observation direction and magnetic field line. After weighting, each individual component is assigned the estimated ion temperature and folded with the instrument function. Finally, all components are summed to form the resulting spectral line. By measuring this complete spectrum in the same way (i.e. by fitting a Gaussian model function) as done with the experimental data, one can calculate an apparent temperature from the ion temperature that enters the model as a guess. By iterating the estimate, any experimental spectrum can be matched with a best guess for the actual ion temperature.

Figure 4.6 shows a comparison of resulting "reduction factors" (i.e. the necessary multiplicative correction for the apparent temperature) for carbon and helium for a range of conditions relevant in the experiment. They are most significant for carbon at the plasma edge, where the reduction factor can become lower than 0.7, effectively reducing the uncorrected ion temperature by more than 30%.

4.4 Differences of helium and carbon charge-exchange

The main differences between C and He lie in the positions of their radial shell structure relative to the beam penetration and to the ion temperature profile.

In general the C^{6+} concentration drops significantly at the plasma edge due to relatively high ionization energies. On the other hand, the penetration depth of the lithium beam is limited, so that a sufficiently high charge exchange rate ($S_{CX} \propto n_{Li} \cdot n_{X^{z+}}$), can only be achieved in a narrow overlap region. A typical net signal intensity profile of carbon thus has a peaked maximum somewhere along the beam axis. From this maximum towards the plasma center the beam attenuation is predominant; towards the outside, the amount of charge exchange is limited by the low C^{6+} density.

For helium the situation is generally similar, but quantitatively rather different. It is

---

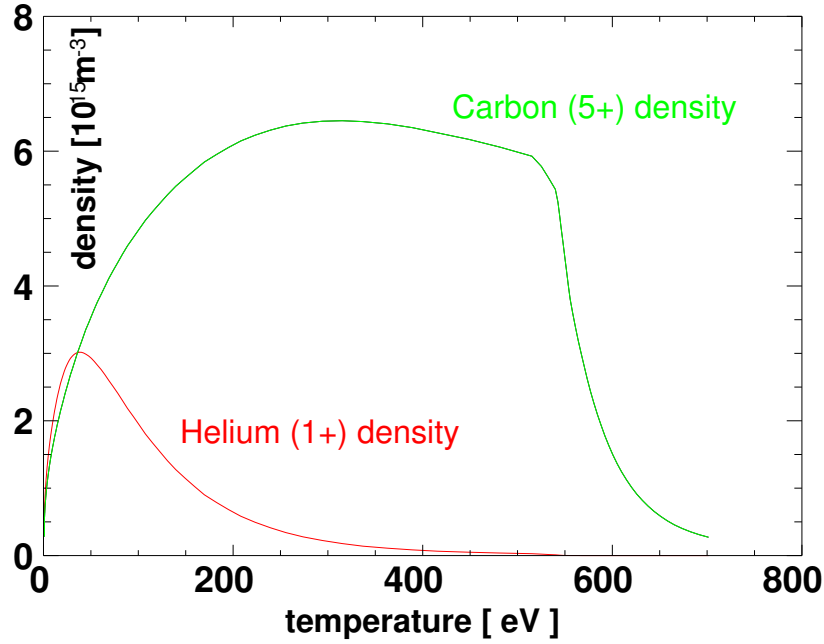[2]Emission coefficients for each state (**LJ**) listed separately.

Figure 4.7: Results of a STRAHL (impurity code) calculation, modeling an L-mode plasma with equal impurity sources for the He and C case show: The C^{5+} shell is broader than the He^+ shell both spatially and in temperature range. In the pedestal region the more abundant C^{5+} radiates with similar temperatures as the charge-exchange component. The helium background strongly peaks at about 50 eV, thus being much less prohibitive for accurate net signal determination at temperatures over 50 eV.

usually fully ionized already at rather low (50 eV) electron temperatures and therefore He^{2+} is present even in the SOL. Thus, in principle, measurements using helium are possible in a much wider spatial region than carbon. Moreover, the background line radiation is affecting a smaller spectral range. This is found to be the main reason why helium temperatures are usually determined with less uncertainty than those of carbon, while both agree on the actual temperature value within their respective uncertainties (see also section 4.4.1). The different shell structure is important for the passive background signal originating from the hydrogen-like impurity shell. Figure 4.7 shows the equilibrated results of a STRAHL [48] simulation with temperature and density profiles taken from an L-mode discharge. The local C^{5+} density profile spans a much broader and hotter temperature range than the He^+ profile. The differences are related to the observed background radiation. The dominant processes responsible for this radiation are electron excitation of C^{5+} (and He^+, respectively) and recombination of C^{6+} (and He^{2+}) with free electrons or, more likely, by charge exchange with neutrals coming from the SOL. While the C^{5+} density maximum is usually well inside the separatrix, the narrower He^+ shell appears close to it or even outside. The passive spectrum, formed by a line-of-sight integral through several flux surfaces, usually deviates from a Gaussian (compare
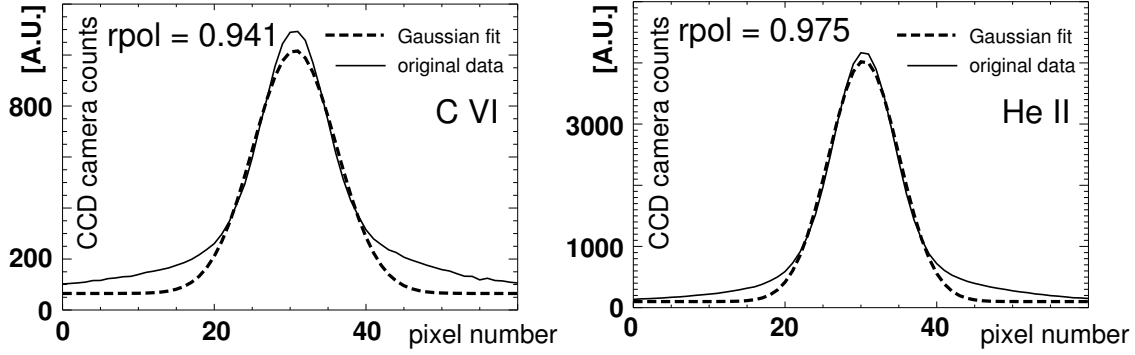
Figure 4.8: The averaged passive signal of neither carbon (left) nor helium (right) have a clear Gaussian shape. It is rather a mix of several components along the whole line-of-sight. Using a Gaussian fit, the appropriate mass and the right wavelength for the element to determine the temperature, results in average background temperatures of about 300-400 eV for C VI and about 20-50 eV for He II.

with Figure 4.8) and a simple fit to it results in an average temperature along the respective line-of-sight. Typical values range from 300-400 eV for carbon and 20-50 eV for helium. This large difference has a direct consequence for the local measurement.

For instance, selecting a line-of-sight inside the separatrix which is roughly tangential to the C^{5+} shell maximum, the spectral line shapes of the active and passive components of C^{5+} radiation (C VI, $\lambda = 529.0 \ nm$) may be rather similar, i.e. the local temperature just about equals the average line-of-sight temperature. In this case an accurate extraction of the active component requires an exact absolute determination of the signals with and without beam. This leads to long integration times (> 2 s) in order to be able to distinguish between average background temperature and local ion temperature.

Using helium in the same scenario and radial channel position, the background photon flux from the He^+ shell (He II, $\lambda = 468.5 \ nm$) compared to the active component is typically higher, but its spectral line width is much narrower than that of the active signal determined by the higher local temperature well inside the separatrix. Ideally, the desired broad spectral line width and hence the local ion temperature can be extracted simply by fitting a Gaussian to the line wings in the measured spectrum, even if the SNR in the line center is of order unity.

Although helium is in this respect always favorable to carbon, carbon can be superior, when there is a higher than average carbon content in the plasma, e.g. with plasma discharges in configurations not used regularly, where additional carbon is eroded from otherwise cold surfaces. Then the higher charge exchange cross section combined with relatively high carbon concentrations is sufficient to overcome these disadvantages.

In cases where both species can be measured in similar conditions (i.e. by repeating a discharge with different spectrometer settings), the helium and carbon temperature profiles coincide in the limit of short collisional relaxation times compared to transport times (see section 2.3.2). In the next section, this is demonstrated for an L-mode discharge.
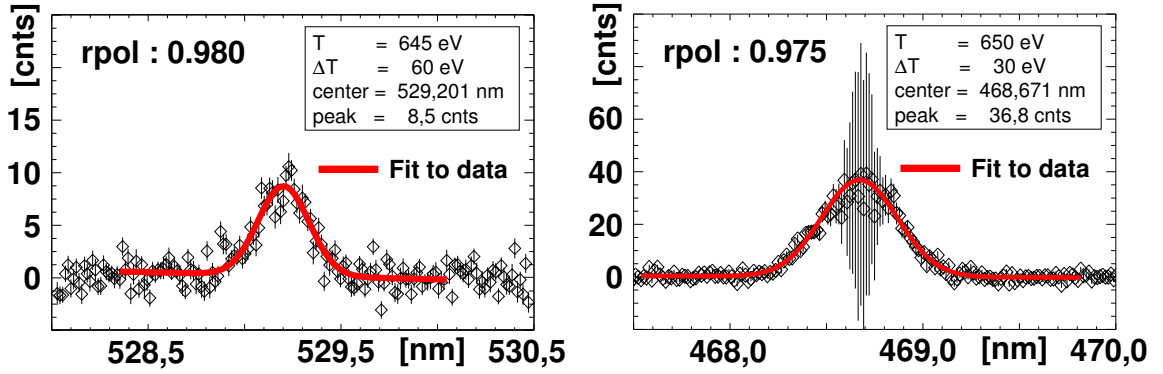
Figure 4.9: H-mode net spectra (active - passive signal) of carbon (left) and helium (right). Helium background radiation is much stronger due to ELMs and recycling from the vessel walls but restricted to a narrow spectral range. Thus, error bars (including correlated noise; see Section 4.3.1) are large in the central wavelength region. Compared to carbon, He II temperatures still have less uncertainty because influence from the line's central region is suppressed by weighting the data and the net signal temperature is mostly determined from the wings, where influence from the He background radiation is at a minimum. Since C^{5+} background radiation affects a much wider spectral range, the carbon background radiation impacts the whole line width, which is reflected in the higher pixel-to-pixel scatter and consequently larger uncertainties.

4.4.1 Comparison of He and C temperatures

A series of identical NBI-heated L-mode plasma discharges featured impurity gas puffs of heavy methane (CD_4) in different strengths. The plasma is kept in a long plateau phase, where parameters such as density, electron and core ion temperature and stored energy change only within a narrow range of about 10% despite the increasing impurity influx.

Since these L-mode discharges are stationary for about 4 seconds, accurate temperatures can be determined both for C (#16891) and for He (#16892). Therefore, the discharges are well suited for a comparison between the impurities and discussion of the ADAS corrections (compare Section 4.3.3) applied to both species. Figure 4.10 shows the temperature profiles of both discharges with different levels of corrections applied. Profiles without any corrections (Figure 4.10a) show the largest discrepancy because of the large difference in "instrumental temperature", which has high impact at low temperatures. Deconvolution of the instrument function already brings the profiles within range of the error bar from fitting (Figure 4.10b). The detailed calculations, which also include experimental electron density (from LID) for each spatial channel, result in agreement of the determined temperatures of carbon and helium within a few percent (Figure 4.10c).

4.4.2 Increasing the signal-to-noise ratio (SNR) by impurity puffing

The impurity content may be changed as a free parameter as long as its concentration is low enough that the impurity can be considered to be in the trace limit[3]. Therefore, the possibility of increasing the SNR was investigated by applying impurity gas puffs with helium and CD_4 during stationary phases of L-mode plasmas.

In both discharges (#16891, #16892), it can be seen that a signal intensity increase is correlated with increasing the CD_4 puff rate at 3.5 s and 4.5 s (see Figure 4.11). The effect is seen for both C and He and the relative signal increases ($\approx 5\%$) are comparable for both elements. This suggests that the enhancement of the spectral line radiation is mostly due to increased electron density and the resulting excitation and recombination

---

[3]An impurity is said to be in the trace limit, when its contribution to Z_{eff} is negligible ($Z_{eff} = \sum_i n_i Z_i^2 / \sum_i n_i Z_i$, where i denotes all present ion species).
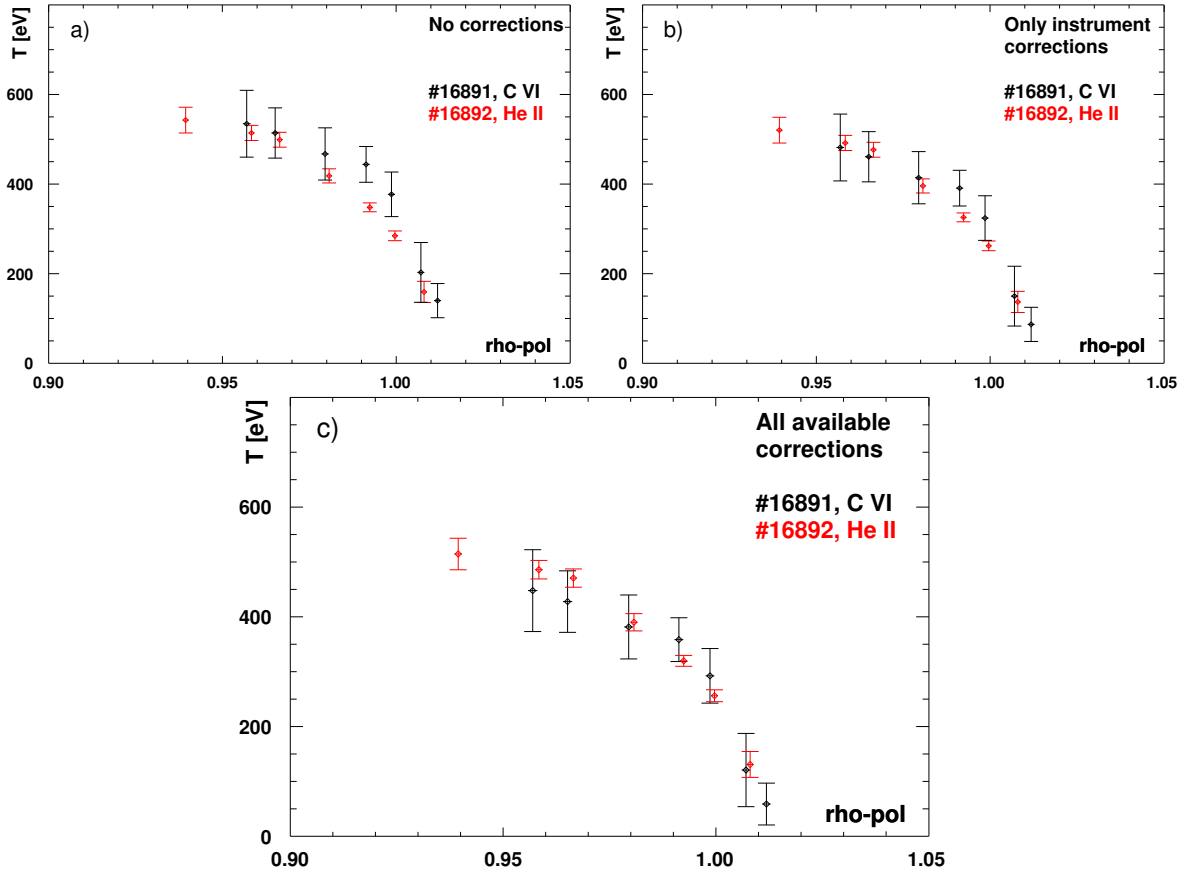

Figure 4.10: An L-mode discharge was repeated to measure both He and C ion temperatures. All three profiles are calculated from the same raw data, but have been corrected for systematic errors with different levels of sophistication. (a) No corrections. (b) Instrument correction only. (c) Fully detailed ADAS corrections including electron density from LID measurements.
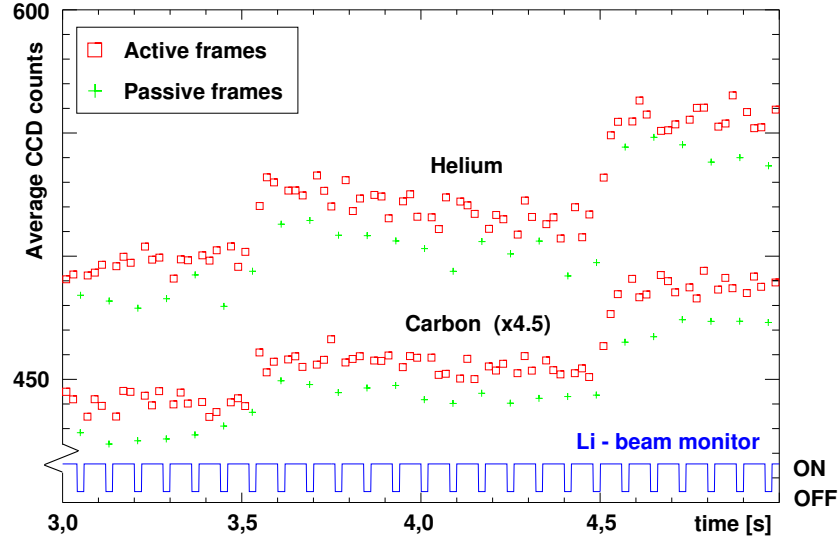
Figure 4.11: L-mode time trace signal (suppressed zero) for C VI (#16891) and He II (#16892) line (C VI multiplied by a factor of 4.5 to be on scale). The intensity increase (with a comparable magnitude) is for both species time-correlated with an increasing methane (CD_4) puff. This indicates a strong dependence of the signal intensity on the electron density change which dominates the effect by the change of carbon content.

processes. Thus, it is concluded that carbon concentration could not be significantly raised.

A similar L-mode with near identical parameters ($I_p = 1$ MA, $\overline{n_e} = 4 \cdot 10^{19}$ m^{-2}, $\delta \approx 0.3$, $B_t = 2.7$ T) was performed shortly after coating the vessel interior with boron. The boronization decreased the residual amount of He in the plasma edge. A pair of discharges (#16979, #16981) then allowed a direct investigation of the effect of additional He on the temperature measurement. A helium puff rate of $2.6 \cdot 10^{21}$ particles/s was applied for about 40 ms in the second discharge. This puff generated a considerable signal quality improvement over the discharge which did not have additional helium. It sufficiently increased the charge-exchange part of the He II radiation to reduce the uncertainty in the temperatures by more than 50% (Figure 4.12).

The main difference between CD_4 and He puffing is the relative magnitude of the change of local electron density. While each He atom brings 2 electrons into the plasma, each CD_4 molecule adds 10 electrons per carbon ion and therefore the increase of background radiation through the local electron density increase is much more meaningful than the change in the carbon density.
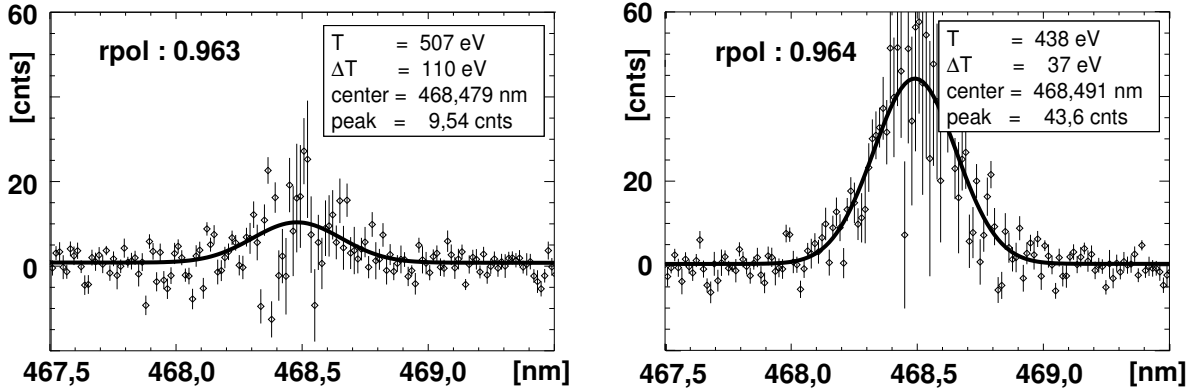
Figure 4.12: He II net spectra with 0.5 seconds integration time of the charge exchange component in identical phases of 2 discharges. The left spectrum is taken from #16979, which has no He puff, the right spectrum is taken from #16981, where a 40 ms duration He-puff with $2.6 \cdot 10^{21}$ He-atoms/s was applied just before the measurement.

4.5 Special problems in the H-mode regime: ELMs

Edge Localized Modes (ELMs) are periodically-appearing instabilities of the plasma edge, that transiently cause a greatly amplified transport of energy and particles across the separatrix on a sub-ms timescale. They appear only in H-mode, where confinement is high and a pedestal-like shape is formed in radial density and temperature profiles (see
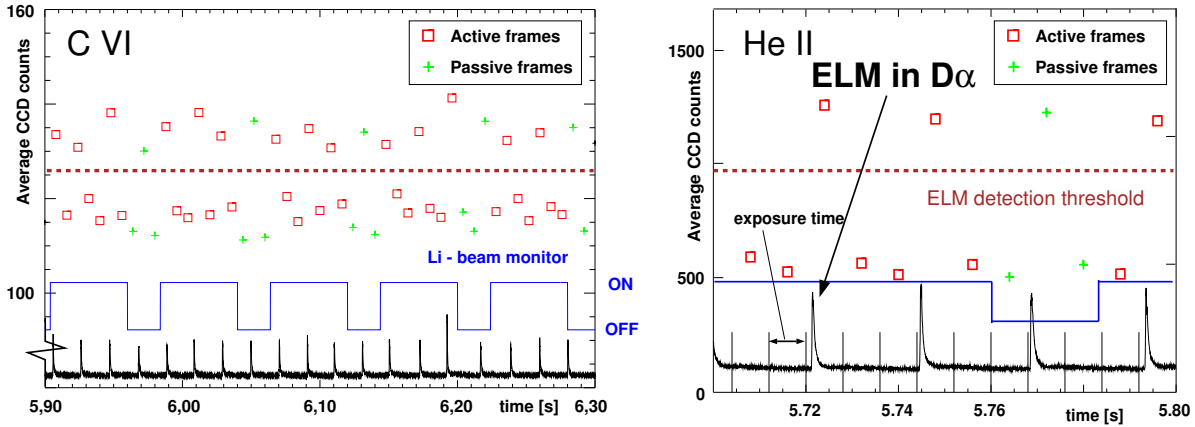

Figure 4.13: Time evolution of average C VI (left) and He II (right) intensity as seen by the CXRS system in H-mode discharges with low frequency ELMs are shown. ELMs increase the background impurity line radiation by orders of magnitude so that even spectrally averaged and time-integrated (exposure time of 8 ms in C case, exposure time of 20 ms in He case) signals are dominated by the 1-3 ms long ELM events. For the temperature evaluation, only frames with an average count rate below the indicated threshold are used.

also Section 2.4.2). The type-I ELM causes a spike of D_α emission, which is most intense in the divertor. Emission is not only increased in the hydrogen lines, but also in those of impurities. This imposes the biggest problem on the ion temperature measurements in this regime. Each ELM is accompanied by a large, nonlinear increase of impurity line intensity which is higher than the amplitude of the charge exchange component of the active frames (Figure 4.13). Despite the relatively short life-time of ELMs ($\lesssim 1$ ms), the effect of a single ELM event on the impurity radiation is typically sufficient to significantly affect several seconds of ELM-free time integration.

Due to the sequential recording of active and passive data and beam switching times of about 0.5 ms, it is not possible to resolve individual ELMs with this diagnostic at present. The irregular behavior of background radiation, probably caused by the 3D-structure of an ELM [49], renders data affected by ELM enhanced radiation extremely difficult to evaluate. Typically, only low ELM frequency discharges having more than 10 ms long ELM free phases can be studied, because enough data must be collected during quiet phases and the minimum camera exposure time is 4 ms with the full wavelength range and channel number. In discharges with low ELM frequencies, it is then possible to remove frames influenced by ELM events from the evaluation and use only ELM-free exposures (Figure 4.13) for an inter-ELM ion temperature profile. Thus, the solution for H-mode temperature profiles is to cut out ELM affected data and to determine an effective inter-ELM temperature profile. For practical application of this technique, the detector frame rate has to exceed the ELM-frequency by at least a factor of 2. Usually a factor of 3 is required, because increased wall recycling shortly after the ELM event affects the background radiation with about the same magnitude as the charge-exchange process and therefore would deteriorate the temperature information with additional noise.

For the purpose of detecting the ELM onset and decay the raw signal of spectrally averaged CCD counts can be processed with a simple threshold algorithm (compare with threshold in Figure 4.13). Alternatively the separately available D_α signal from the divertor can be directly evaluated using a sophisticated ELM-detection algorithm [50]. An empirical safety delay after the ELM is introduced to exclude the repercussions that influence the edge and scrape-off layer density for up to several milliseconds after the ELM peak time. All ELM-free data are then averaged in the previously described manner and temperatures are determined as in the ELM-free case.

5 Results and discussion

While the previous chapter contained detailed discussions about the acquisition and evaluation of raw data, in this chapter, results of the new diagnostic from various plasma scenarios (ohmic plasmas at different densities, L-mode with ECRH and NBI, H-mode and QH-mode) are presented and discussed. The general observation of higher ion separatrix temperatures than electron temperatures combined with a less steep gradient and consequent profile cross-over in electron heated discharges is demonstrated. For the interpretation of measurements in the ohmic plasma regime, the computer programs B2 and ASTRA (also called code packages) were used. Results from these calculations are discussed in the final section of this chapter.

5.1 Ohmic plasmas

5.1.1 Standard ohmic discharge

On each "experimental day", ASDEX Upgrade uses three standardized discharges for diagnostic initialization and long-term monitoring of machine performance. One of the three standard shots is an ohmic plasma with a plasma current flattop time of about 5 seconds and two different density levels. This discharge has a plasma current of 800 kA and a toroidal magnetic field of 2.0 T at the magnetic axis. The line-integrated density is controlled by gas valve feedback via the central DCN[1] interferometer channel to values of $2.5 \cdot 10^{19}$ m^{-2} and $3.5 \cdot 10^{19}$ m^{-2} for 2.5 seconds each.

The following discussion will concentrate on the high density phase of this discharge (t = 4.4 s - 4.9 s). Figure 5.1 shows global profiles of temperatures (T_e from ECE and YAR, central T_i from NPA, edge T_i from LIT, right) and density measurements (combined from LID, YAG/YAR and DCN, left). The discharge has no other heating than ohmic resistivity, which predominantly heats the electrons. This is reflected by a higher electron temperature than ion temperature in the core plasma, where $T_{i,max}$ was estimated by measurements of the neutral particle analyzer (NPA). The core plasma undergoes sawtooth events[2] causing the considerable scatter in the central ECE data.

---

[1] Three letter abbreviations used for diagnostics are explained in Chapter 3.

[2] Sawtooth: periodical MHD instability leading to expulsion of the hot plasma core, observed as a slow rise and subsequent rapid drop in central electron temperature.
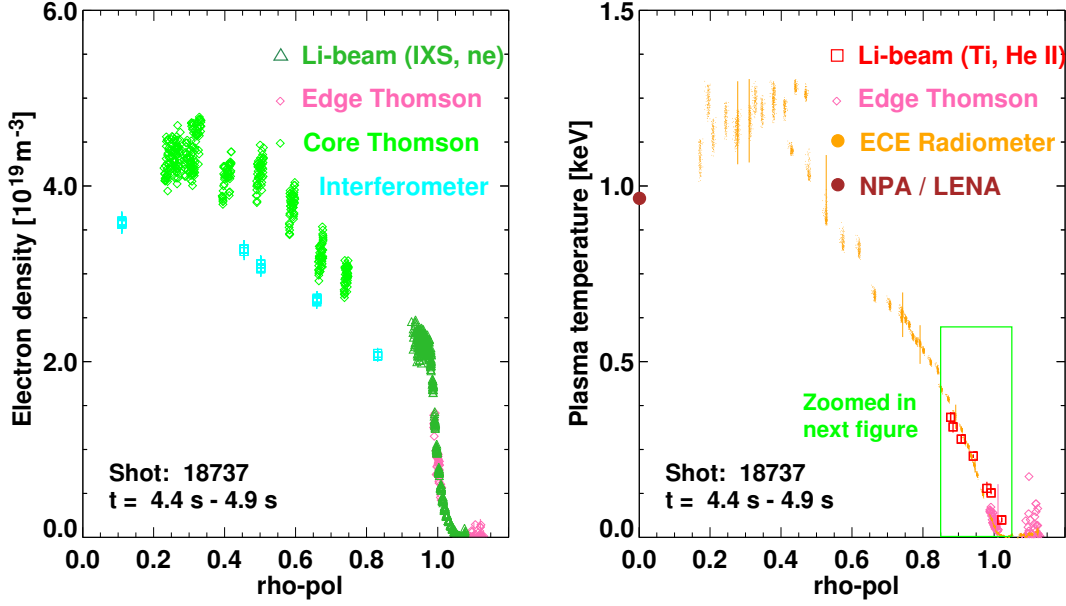
Figure 5.1: Plasma profiles of electron density and ion and electron temperature plotted after mapping to normalized poloidal flux ρ_{pol} for the full radius (magnetic axis at $\rho_{pol} = 0.0$, separatrix at $\rho_{pol} = 1.0$). The framed part of the temperature plot is shown magnified in Figure 5.2.

These phenomena are confirmed by equilibrium reconstruction ($q=1$ surface located at about $\rho_{pol} \approx 0.5$). Frequency spectrum analysis of the ECE channels which yields the signature of a rotating magnetic island at $\rho_{pol} \approx 0.45$ provides a further indication for the appearance of sawteeth in the plasma.

The ion temperature gradient and the local edge ion temperatures, which are measured by Li-beam CXRS, can be compared to the electron data from ECE and YAR. At the separatrix, the ion temperature exceeds the electron temperature by at least a factor of two (see Figure 5.2). In fact, the ion temperature profile crosses the electron temperature profile at a normalized radius of $\rho_{pol} \approx 0.94$.

5.1.2 High density ohmic plasma

In Figure 5.3, the temperature measurements of an ohmic discharge with a current of 800 kA, magnetic field of 2.4 T and central line integrated density of $6.1 \cdot 10^{19}$ m^{-2} are shown. The high density leads to conditions where both the electrons and the ions are in the Pfirsch-Schlüter transport regime for $\rho_{pol} \geq 0.85$. The estimated transport times (see Section 2.3.2) are lower than the electron-ion heat exchange time in the whole gradient region. A naive interpretation would suggest that the temperatures should
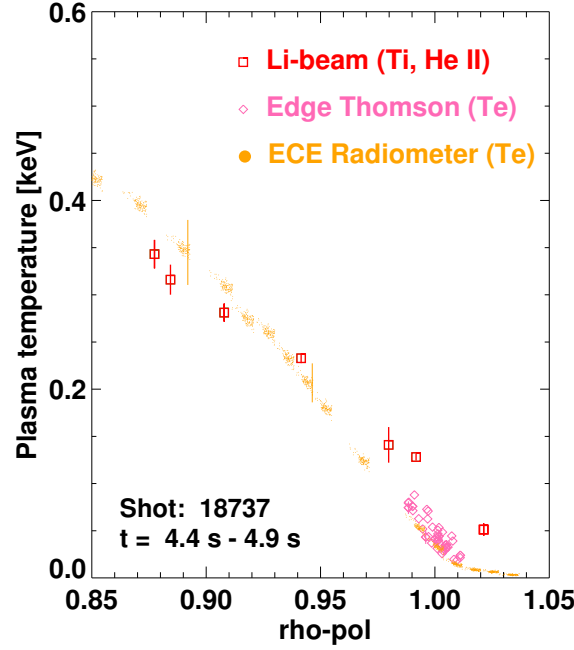
Figure 5.2: Edge temperature profiles of the ohmic standard discharge. Ion temperature as measured by the lithium beam diagnostic, electron temperature from ECE and YAR.

equilibrate, if heat exchange between electrons and ions is much faster than particle transport. The measurements show that the profiles cross at about the same radial position ($\rho_p \approx 0.96$) as seen in other ohmic discharges and ions and electrons appear to be not strongly coupled. Whether this is due to anomalous transport remains to be clarified.

5.1.3 Low current, low density ohmic plasma

The measurements in this case have been obtained in a parasitic way on a discharge dedicated to electron transport studies of the core plasma. The ohmic reference shot of this investigation was run at low triangularity with a plasma current of 600 kA, toroidal magnetic field of 2.5 T (ramped down to 2.25 T during the discharge) and line averaged density of $2 \cdot 10^{19}$ m^{-3} with a mild D_2 gas puff. Due to the low plasma current and without additional heating, the total heating power amounts to only 320 kW. This is the lowest heating power in all analyzed plasmas. An identical magnetic configuration was used in the first ECRH example shown in the following section.

For the ohmic discharge (see Figure 5.4), the ECE electron temperature is 40-60 eV at the separatrix with a constant gradient of ≈ 40 eV/cm towards the plasma center. The edge ion temperatures (from He II) are significantly higher and the gradient of ≈ 20 eV/cm is about half as steep as that of the electrons. The ion separatrix temperature is 135±10 eV, higher than the electron temperatures by at least a factor of two.
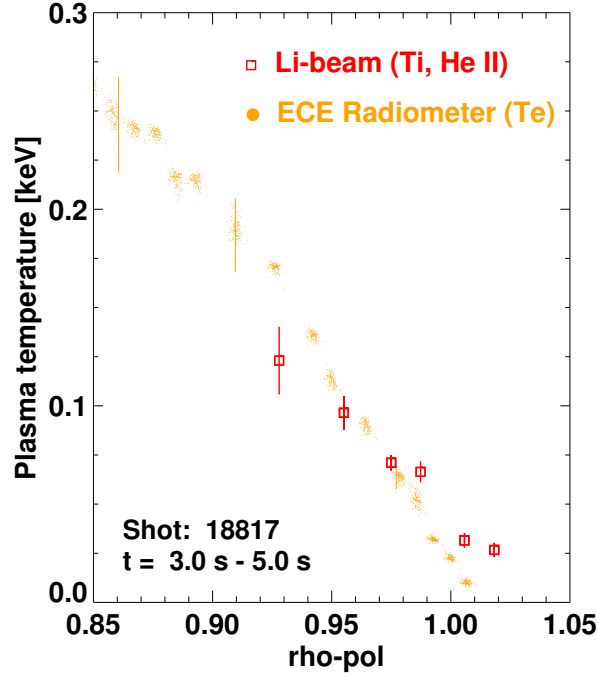
Figure 5.3: Edge temperature comparison (electrons and ions) of high density ohmic discharge, where both electrons and ions reside in the Pfirsch-Schlüter (high collisionality) transport regime. Qualitative agreement (profile crossing) with low density ohmic and ECRH heated L-modes is seen.

5.2 Electron heated L-mode

The measurements described in this section have also been obtained partly parasitically. This includes radial scans of the electron cyclotron heating deposition in the core and stationary L-mode plasmas for investigation of the density response to ECRH heating on and off-axis [51]. Some additional dedicated discharges of a similar type were also performed.

The plasma density in the analyzed discharges varies from low ($\overline{n_e} \approx 2.0 \cdot 10^{19}$ m^{-2} central line averaged density) to relatively high values ($\overline{n_e} \approx 6.0 \cdot 10^{19}$ m^{-2}). The profiles are qualitatively similar to the ohmic cases with steeper electron temperature gradients than ion temperature gradients. Absolute temperature values vary with applied heating power and densities. Moreover, the separatrix temperatures are significantly higher due to the higher total heating power and this increase in temperature is even more pronounced in the ions. Separatrix ion temperatures of up to 250 eV have been observed in a purely electron heated discharge.
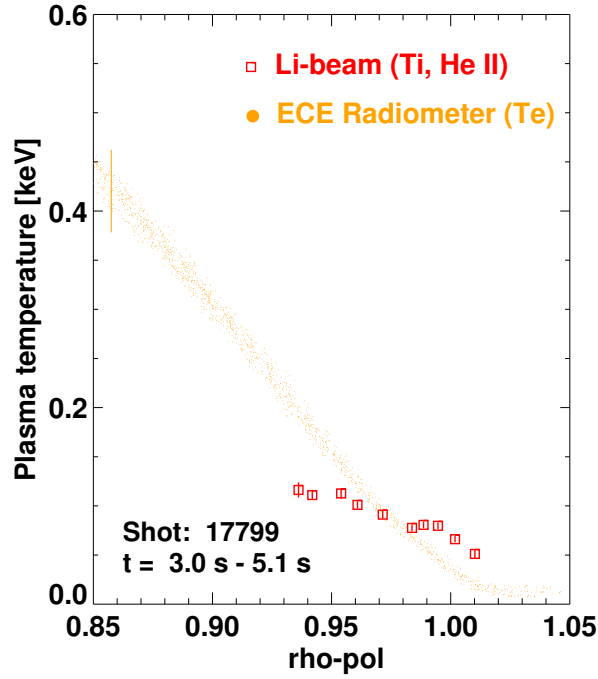
Figure 5.4: Edge temperature comparison of low density, low power ohmic discharge. This plasma has the lowest ion temperature gradient measured with the CXRS diagnostic (about 20 eV/cm).

5.2.1 Low density, high power

The companion shot to #17799 has a slightly faster B-field ramp and 1.2 MW total heating power (about 1.1 MW radially localized ECRH between $\rho_{pol} = 0.26 - 0.34$, #17800). A stationary interval of about 1 s (with ECRH) was analyzed. For a similar discharge (#17801, magnetic field being lower by 0.2 T) the spectrometer was changed to the spectral wavelength of the carbon line. The main difference of discharge #17801 compared to #17800 was that the ECRH power deposition occurred between $\rho_{pol} = 0.47 - 0.58$. Near the plasma edge ($\rho_{pol} \approx 0.9$), the differences in the ECE radiation temperature between these discharges were less than 5%, so the influence on main species ion temperature there should be negligible.

The measured edge T_i profiles and parts of the T_e data are shown in Figure 5.5. The comparison between ion temperatures of different impurities in near identical discharges was already done for NBI heated L-modes (see Section 4.4.1), but could be repeated on this occasion. There is agreement between He^{2+} and C^{6+} temperatures within the experimental error bars except for one outlier in the carbon measurements which is explained by imperfect subtraction of the passive signal, which evaluates to a temperature of almost 1 keV. The reason for this deviation from the mean of about 400 eV for the other channels is not known.
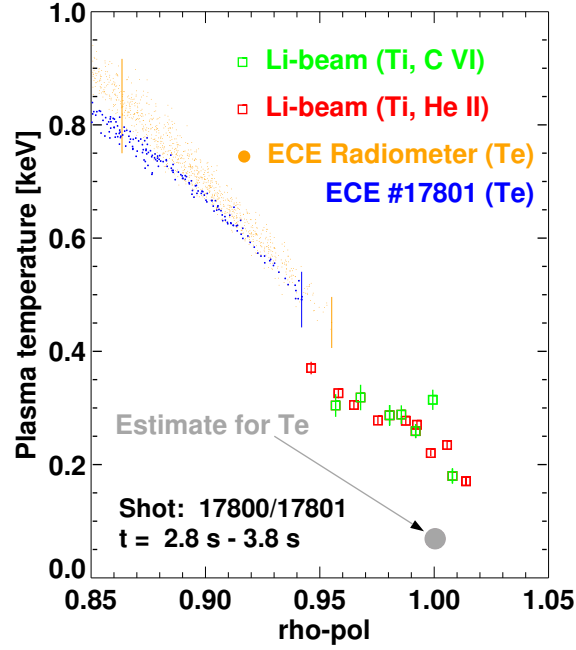
Figure 5.5: Edge temperature profile comparison between electrons and ions. Two discharges, both at low density with 1.1 MW ECRH heating in the plasma core are plotted. He and C edge temperatures agree, electron separatrix temperature was estimated by comparison with similar discharge. The outlier in the carbon profile is explained by imperfect background subtraction, which had an unusually high passive temperature (900 eV) for this particular channel only.

Since ECE did not measure near the separatrix due to the changed magnetic field, the electron separatrix temperature $T_{e,sep}$ was estimated from a comparable discharge (#15428, identical plasma current and density, similar magnetic field and YAR). $T_{e,sep}$ assumes a value between 60 and 80 eV, the ions in #17800, however, reach temperatures as high as 240 ± 10 eV at $\rho_{pol} = 1.0$. This is more than a factor of three above the electron temperature despite strong electron heating in the core. The temperature profiles therefore cross each other inside the last closed flux surface.

5.2.2 Density scan of electron heated plasmas

After looking at data from a number of similar discharges with dominant electron heating, it became apparent that ion temperatures always exceed the electron temperatures near the separatrix and exhibit smaller gradients towards the central plasma, so that a profile crossing occurs somewhere between $\rho_{pol} \approx 0.93 - 0.96$. This behavior is independent of collisionality as can be seen from Figure 5.6. Plotted are interpolated values of ion and electron temperature at different plasma positions ($\rho_{pol} = 0.9$, $\rho_{pol} = 0.95$, $\rho_{pol} = 1.0$) in several L-mode discharges. Varying the collisionality over a broad range

by changing density and input power (via plasma current or ECRH) does not indicate any changes in this behavior. The indicated transport regime transitions which depend on collisionality are calculated using Equation (2.13) with a representative magnetic safety factor $q \approx 4$. The density range is sufficient to include all transport regimes distinguished by neoclassical theory. No change in the observed behavior takes place. Since absolute temperatures and gradients also depend on the amount of applied external heating, which was different from discharge to discharge, particular trends cannot be inferred from this study because the data set is too small.
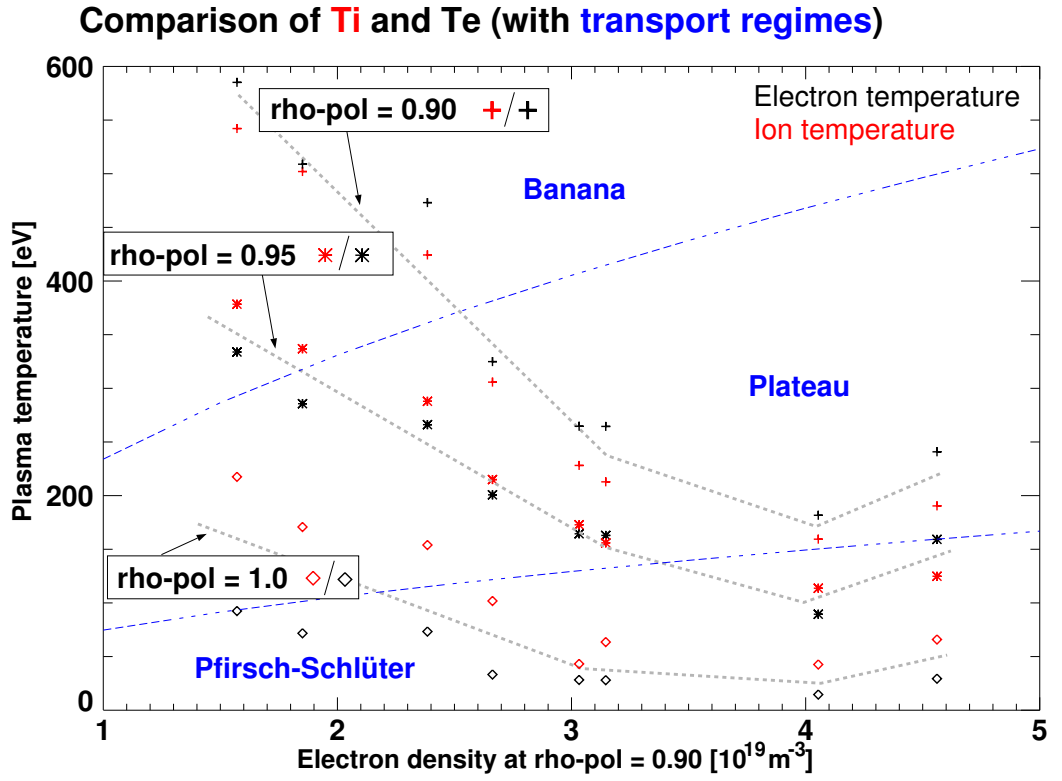
Figure 5.6: Electron and ion temperatures for 3 different locations of several electron heated plasma discharges. A clear trend is the higher electron temperatures compared to ions in the core ($\rho_{pol} \leqq 0.9$) which reverses somewhere near the edge $0.93 \lesssim \rho_{pol} \lesssim 0.96$. The separatrix temperatures confirm that the profiles indeed cross. The transport regime transitions were calculated using Equation 2.13 with a magnetic safety factor $q \approx 4$.

5.3 NBI heated plasmas

5.3.1 Improved L-mode

In order to study another heating mechanism, NBI-heated L-mode discharges specifically addressing T_i-measurements were performed. Reducing the acceleration voltage of the neutral beams from 60 kV to 44 kV while increasing the magnetic field to 2.6 T permitted operation below the L-H power threshold. The combined heating power of 1.3 MW by neutral beams and about 0.5 MW by ohmic heating still puts the plasma close to the H-mode threshold, creating some intermittent edge behavior. The plasma ($I_p = 1$ MA, $\overline{n_e} = 4 \cdot 10^{19}$ m^{-2}) was shape-optimized for edge diagnostics. A series of identical discharges featured an impurity gas puff of heavy methane (CD_4) in different strengths for the experiment described in Section 4.4.1.

The plasma is kept in a long plateau phase, where properties such as electron density, electron and ion temperature as well as stored energy change only within a narrow range of about 10% despite the increasing impurity gas puff. This permits time integration

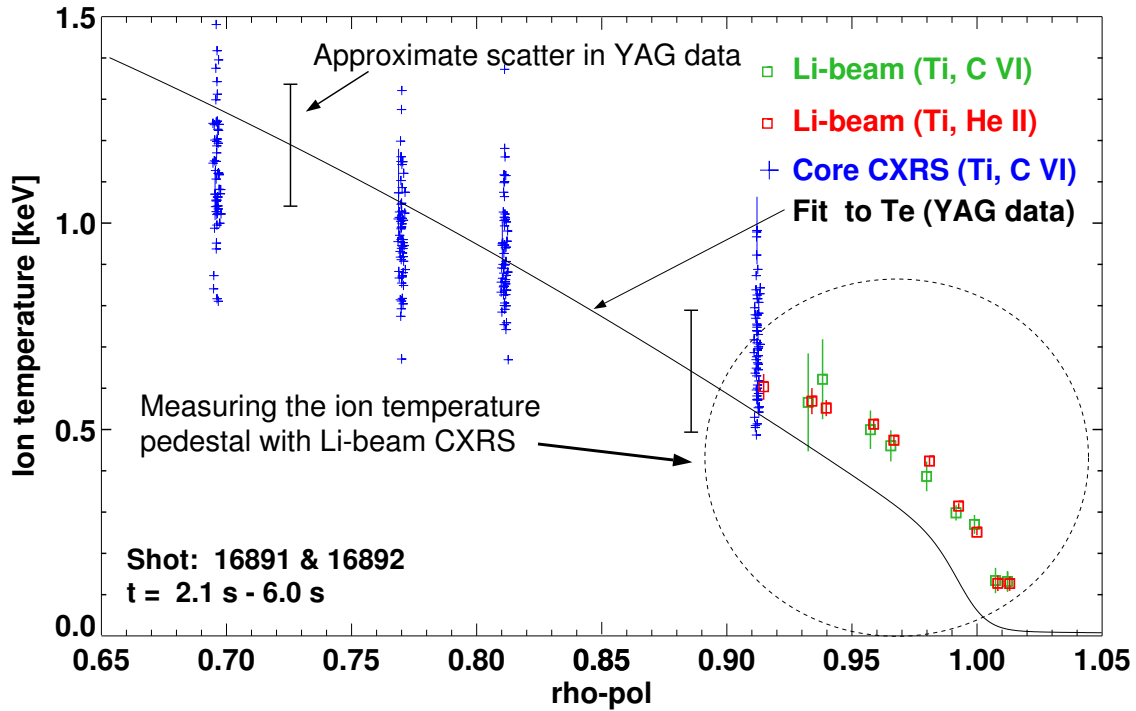**Figure 5.7:** Ion temperatures from the improved L-mode show a pedestal as do the electron temperatures. Carbon and helium temperatures agree within their experimental error bars and connect seamlessly to the core measurements. Electron temperature data was subject to large scatter (see "scatter" bars). Thus the direct comparison to ion temperatures is difficult, but there is indication for higher ion temperatures at the separatrix.

over more than 3 s for increased accuracy of the measured edge ion temperatures. The discharge does not have typical H-mode character, i.e. there are no ELMs. Since it has a pedestal in electron density and temperature and also in the ion temperatures at approximately the same radial position, this regime is called an "improved L-mode". Figure 5.7 shows the ion temperature profile around the overlap region of CXRS and core CES channels which combine well to form an ion temperature profile for the full plasma radius. Electron temperature data was subject to large scatter and needs to be interpreted with caution. However, a tendency of higher ion temperatures near the separatrix is again seen in the NBI heated improved L-mode.

5.3.2 Quiescent H-mode (QH-Mode)

From the diagnostic point of view, an H-mode without ELMs is the best possible candidate for accurate edge measurements. The QH-mode is such an ELM-free, high confinement regime. It is accessible in plasma configurations with high wall clearance and counter NBI-injection [52]. One of this regime's features is a high pedestal pressure with ion temperatures well in excess of 1 keV [53].

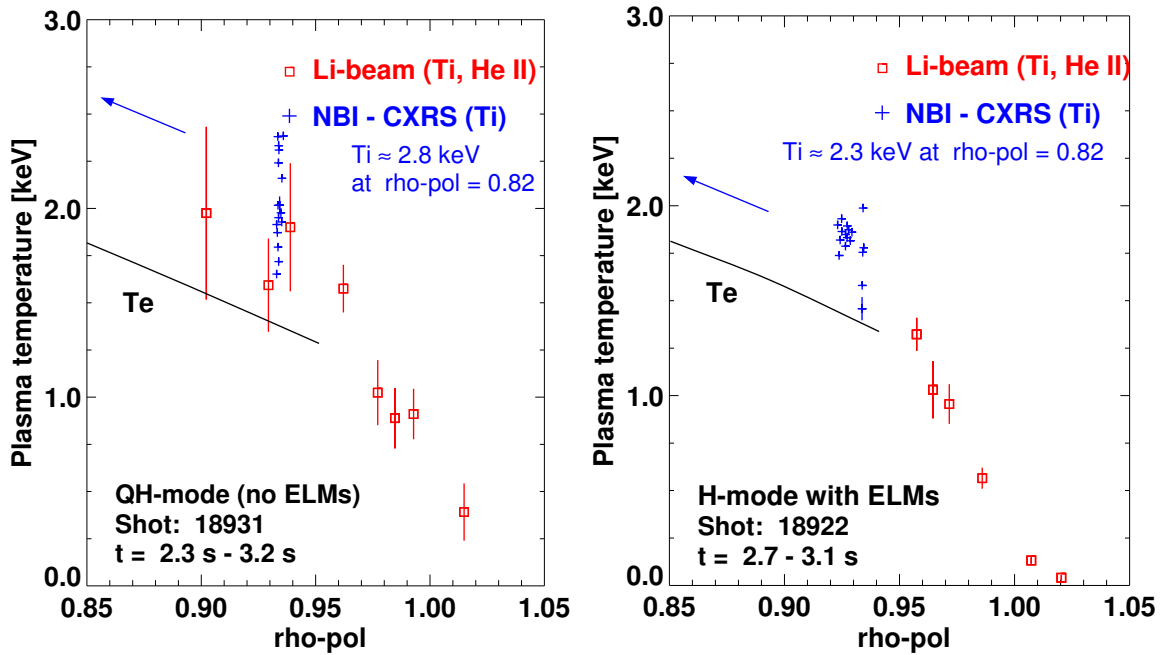**Figure 5.8:** Edge ion temperature versus normalized radius for a QH-mode configuration with reversed field and low edge density. The QH-phase of #18931 is shown left, an H-mode profile of #18922, where ELMs are present, on the right. In both cases, at the overlap/switchover of Li beam and core CES measurements, agreement is found. Knowledge of the full profile allows to measure, e.g. the ion temperature pedestal width.

While the core CES system of ASDEX Upgrade covers the bulk of the plasma, the lithium beam is needed to provide information about the actual pedestal position and gradient length for the edge ion temperatures and thus the width of the H-mode barrier. The typical duration of quiescent phases is about 1-3 s. Stationary edge parameters during that time allow long signal integration. The edge measurements in this regime show excellent agreement with the core temperatures, where core CES and lithium beam CXRS overlap (Figure 5.8, left). The measured ion temperature gradient exceeds 600 eV/cm in this regime.

Since the QH-regime is a relatively new field of research, the covered parameter range is still narrow. Edge electron temperatures are not yet available in sufficient accuracy (no YAR measurements to date) to perform a more detailed comparison to the measured ion temperatures (the temperature fit in Figure 5.8 is from data measured by ECE).

5.3.3 Conventional H-mode (with ELMs)

5.3.3.1 Low density H-mode

In one of the discharges in QH-configuration (see above), the quiescent regime was not established and the plasma reverted to an H-mode with ELMs. Because of an average ELM frequency of less than 80 Hz, an inter-ELM ion temperature profile at low density (central line averaged density $\overline{n_e} = 4{\cdot}10^{19}$ m^{-2}) could be determined with CCD operation at 4 ms exposure time. The ELMy plasma[3] also has high pedestal ion temperatures (Figure 5.8, right) but stays below the values obtained in QH-mode by about 10-20%. Electron temperatures are indicated for the core by a fit to ECE data only.

5.3.3.2 Medium density H-mode

The H-mode discharges at medium density required a delicate balance between NBI power and plasma shape in order to both keep the ELM frequency low enough to allow inter-ELM measurements and at the same time keep the plasma stationary, which is necessary for long (> 2 s) signal integration.

The discharges shown had a magnetic field of 2.0 T and a plasma current of 800 kA. The line averaged density of $\overline{n_e} \approx 6 \cdot 10^{19}$ m^{-2} in the first discharge dropped to about $\overline{n_e} \approx 5.4{\cdot}10^{19}$ m^{-2} due to a conditioning effect of the machine, which prohibits a detailed comparison of these discharges. The results, together with the electron temperature (as a fit to the raw data) for the case where Thomson edge measurements were available, are shown in Figure 5.9.

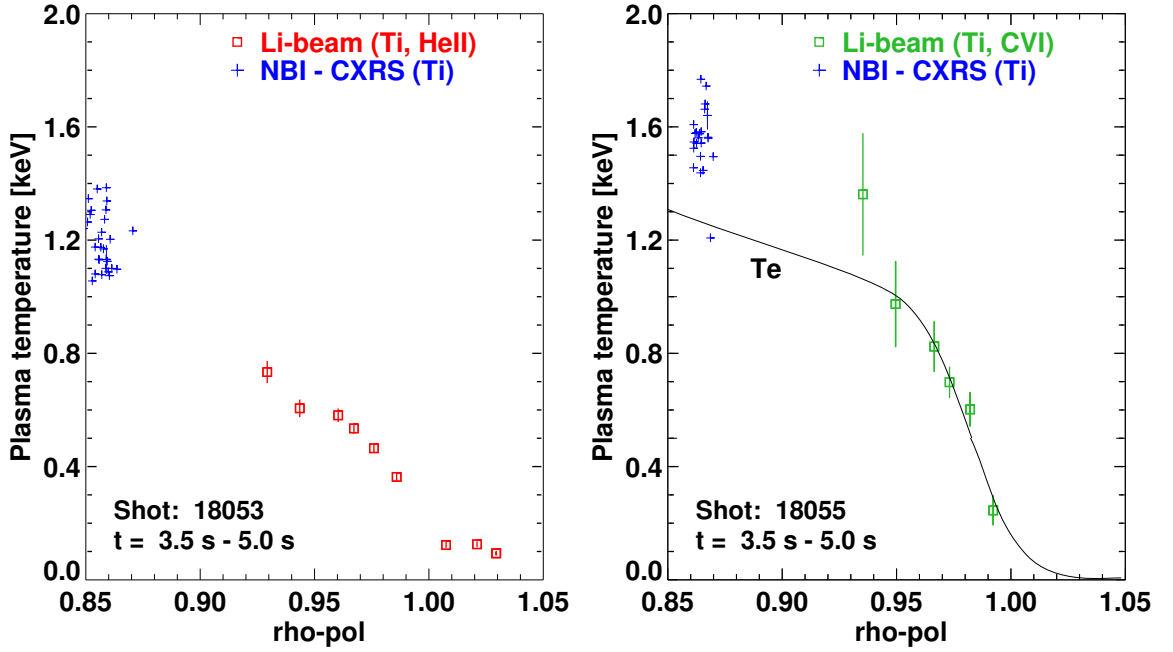[3]ELMy plasma: Plasma where ELMs are present

Figure 5.9: Edge ion temperatures versus normalized radius for medium density ELMy H-mode discharges. Left: #18053 on He II, line averaged density of $\overline{n_e} \approx 6 \cdot 10^{19}$ m^{-2}, Right: #18055 on C VI, line averaged density of $\overline{n_e} \approx 5.4 \cdot 10^{19}$ m^{-2} and T_e-fit using available YAR.

5.3.3.3 Moderate to high density H-mode

The discharges at moderate to high density ($B_t = 2.4$ T, $I_p = 1$ MA, $\overline{n_e} = 6.4 \cdot 10^{19}$ m^{-3}) were fueled by a feed-forward D$_2$ gas puff. The applied external heating was pure NBI with a power of 5 MW. The discharge was repeated in order to measure both helium and carbon temperatures.

The measured temperatures of both impurities agree within experimental errors and seamlessly connect to the ion temperature profile from the core system after mapping to flux coordinates is done (Figure 5.10). Electron temperatures are available from ECE and Thomson scattering measurements and a fit to that data (central ECE and edge Thomson scattering), is plotted together with the ion temperatures. Due to high enough core densities and collisionality, it was expected that electron and ion temperatures are closely coupled in the pedestal region. The measurements confirm this and show maybe a factor of 2 higher separatrix ion temperature over the electron temperature there.

Outside the separatrix the constant recycling processes together with ELMs prohibit measurements, also because the expected temperatures are low enough to be similar to the He$^+$ temperature and therefore the scatter in the data is too high (see also discussion in Section 4.3.1).
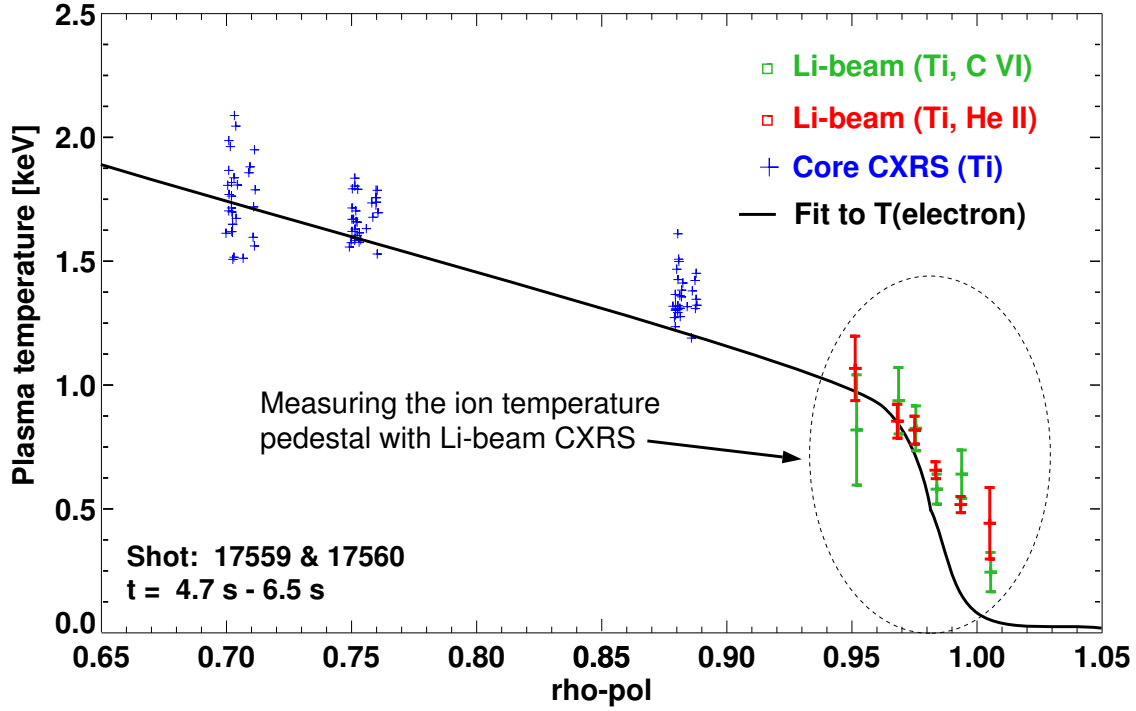
Figure 5.10: Ion temperatures versus normalized poloidal magnetic flux for a medium to high density H-mode discharge with a line averaged density $\overline{n}_e = 6.4 \cdot 10^{19}$ m^{-3}. Both He and C temperatures are plotted together with fit to electron temperature measurements (YAG, YAR, ECE).

5.4 Modeling the standard ohmic plasma

With ion temperature measurements to compare to, the determination of transport coefficients and the check of theoretical models becomes feasible. This was attempted by using two standard code packages at ASDEX Upgrade, the one-dimensional (radial) core transport code ASTRA [54, 55] and the two dimensional (radial-poloidal) edge transport code B2 [28]. ASTRA models the core plasma in some detail, assuming strictly constant plasma properties on closed flux surfaces. This behavior fails near the separatrix due to the importance of poloidally varying particle sources and the reduced parallel conductivity due to lower temperatures and becomes impossible outside the separatrix, where strong gradients also appear parallel to the magnetic field due to wall intersection of field lines. B2 has a comprehensive model for the edge and SOL region and the possibility to integrate the Monte-Carlo code EIRENE [35] for inclusion of realistic neutral particle physics. The necessary extensive computing power for correct resolution of relevant time scales when extending the B2 calculations towards the core make its usage for the core plasma impractical. Ideally, a self-consistent coupling of B2 and ASTRA would be desirable, but is not yet available.

In this case, B2 has been run for the edge region with a guess for the input fluxes from the core, while ASTRA has been used to cross-check these assumptions for their compatibility with core plasma transport. Given all the necessary input in terms of diagnostic information as described in Chapter 3, the actual code runs were done by G. Tardini (ASTRA) and C. Konz (B2) respectively.

In order to run the edge code (B2) with ions and electrons individually, as is essential for this investigation, boundary conditions for the heat flux for the electrons and the ions are needed separately. While the total heat flux can be estimated from total heating and radiated power measurements (i.e. $Q_e + Q_i = P_{heat} - P_{rad.}$), the ratio between Q_e and Q_i is not known experimentally. Thus, an assumption of equal heat flux in the electron and the ion channels was made at the core boundary of the simulated region ($\rho_{pol} \approx 0.85$). Particle and heat transport coefficients were assumed to be constant across the entire computational region. Their values were adjusted to obtain the best match with the experimental profiles. A match to the experimental data (Figure 5.11) has been found for:

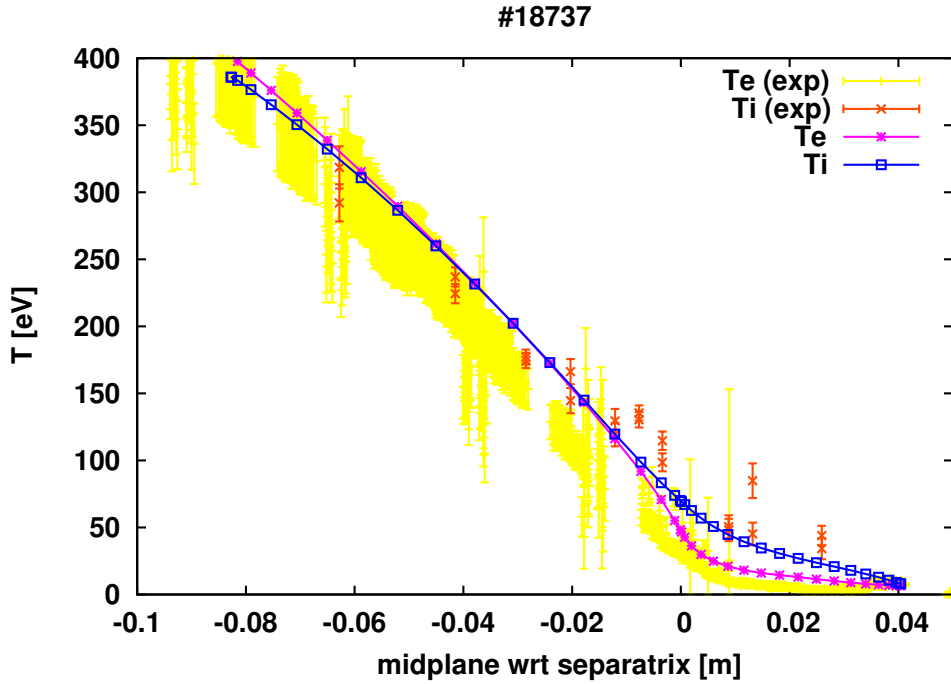|			
Particle:	D	$=$	$0.280 \ m^2 s^{-1}$
Ion heat:	χ_i	$=$	$0.516 \ m^2 s^{-1}$
Electron heat:	χ_e	$=$	$0.435 \ m^2 s^{-1}$

Figure 5.11: Results of the edge profile modeling with B2 using independent energy transport equations for ions and electrons. Plotted are the raw temperature data (indicated as exp) and the respective fits as calculated by the B2 program.

A separate calculation by post-processing the resulting profiles provides an estimate for the transport solely due to neoclassical theory. This was done using an implementation of the NEOART code [56]. The calculation results in ion heat transport with $\chi_{i,neocl.} \lesssim 0.1$ m^{2}s^{-1}. Since the assumption of $Q_e \approx Q_i$ is arbitrary, it is necessary to interpret this result carefully. At first glance, ion transport seems to be anomalous, but the level is not far above the prediction by neoclassical theory. An adjustment in the power fluxes (in order to reduce χ_i by a factor of 5, a boundary condition of $Q_e/Q_i \approx 9$ would be needed because reducing Q_i will approximately linearly reduce χ_i and $Q_e + Q_i = 2Q_0 = const.$) could in principle reduce the ion heat transport coefficient χ_i to the neoclassical value. For a compatibility check with core physics, ASTRA was run in an interpretative and a predictive mode. The interpretative run calculates heat transport and power flux profiles by using experimental plasma profiles of density and temperature. A study of the sensitivity of edge power fluxes on the ion temperature profile in the core (energy transfer between ions and electrons depends on $n_e(T_e - T_i)\mathbf{dV}$) was done by choosing two strongly varying T_i-profiles, each compatible with NPA and edge CXRS measurements. It becomes clear that a prediction of the heat flux ratio at $\rho_{pol} \approx 0.85$ with ASTRA is not precise enough to help much with the edge calculation. Any ratio of Q_e/Q_i between 0.4 and 2 can be forced by changing the ion temperature profile within its uncertainty. Considering the extra uncertainty regarding the radial profiles (because of sawteeth), higher ratios are also possible, but $Q_e/Q_i = 9$ is unlikely.

A predictive run of ASTRA was used to calculate the ion temperature profile while keeping electron properties constant and calculating the ion transport from the radial profiles using the built-in neoclassical transport model (Chang-Hinton formula [57, 58] with finite orbit width corrections [59]). With the boundary condition of the measured edge ion temperatures, the central ion temperature is predicted correctly. At $\rho_{pol} = 0.85$, a ratio of $Q_e/Q_i \approx 1.2$ is predicted for this case. Increasing the prescribed ion heat transport artificially above the neoclassical level in ASTRA would reduce the power flux in the electrons and therefore a contradiction with the B2 calculations results where the computational domains overlap.

As there are no obvious reasons why the ion transport should change drastically at the edge, a globally consistent model of this plasma would only be possible if the codes are coupled and both the edge model of B2 and the core calculations of ASTRA are used in combination. This is desirable for the future, but is beyond the scope of this work.

6 Summary

Magnetic confinement fusion research has progressed to a point where the addressing of specific reactor-relevant issues receives a high attention. The ITER device will demonstrate a burning plasma and provide a stepping stone to the first demonstration power plant based on controlled nuclear fusion. This relies on accessing the so-called H-mode regime which has enhanced edge confinement properties.

Although empirical scalings predict that this is possible, the physical understanding of the plasma edge in divertor tokamaks is not yet comprehensive. It is still unclear what exactly triggers and maintains the characteristic edge transport barrier that leads to steep radial gradients of density and temperature at the plasma edge. Local ion temperatures and ion temperature gradients are candidates for playing an important role for the H-mode access criterion and the overall stability of the edge barrier. In order to validate and understand the scaling of the edge transport barrier, it is crucial to do high resolution measurements of all key parameters that determine the physics there.

The issue of radial edge ion temperature profiles for ASDEX Upgrade has been addressed in this work. A neutral lithium beam is injected into the plasma and used for charge exchange recombination spectroscopy on fully ionized helium and carbon impurities. The equilibration of impurities with the main plasma is fast enough that the assumption of nearly identical temperatures as the main plasma is justified. The ion temperature is calculated from fits to the line radiation of C VI (529.0 nm) and He II (468.5 nm). Systematic line broadening effects from collisional mixing and Zeeman broadening are taken care of by detailed ADAS calculations on a case-to-case basis. Chopping of the beam is necessary to remove the background and extract the small charge exchange contribution to the intensity of the utilized spectral line.

L-mode plasmas with and without additional heating can be reliably diagnosed with a time resolution depending on the chopping frequency and lithium beam intensity, in best cases down to 100 ms. Time resolution is still not sufficient to resolve ELM events which take place at sub-ms timescale. ELMs furthermore lead to irregular and high background radiation (partly due to recycling) and must be cut out before evaluating the data. Inter-ELM measurements in ELMy H-mode plasmas are possible as long as the ELM frequency is low enough, i.e. lower than half the maximum acquisition rate. The detection system consisting of Czerny-Turner spectrometers with high-speed frame transfer CCD cameras operates at up to 250 Hz frame rate by reducing spectral coverage and number of concurrent channels. In L-mode plasmas, it was shown that diagnostic He puffing can be used to enhance the signal-to-noise ratio.

Due to the toroidal symmetry and fast redistribution processes on the magnetic surfaces of a tokamak, the measurements can be compared to other diagnostic data (like electron temperature and core ion temperature measurements) by applying a mapping to magnetic flux coordinates. At ASDEX Upgrade, the tool AUGPED is used to combine data of multiple diagnostics into radial profile measurements. It allows the correction of radial misalignments of diagnostics and thus helps in constructing best possible radial profiles of temperatures, densities and, eventually, plasma pressure.

Results from different-density L-mode plasmas with electron heating (pure ohmic and ECRH) show that ion temperatures can be considerably higher than electron temperatures, and gradient lengths differ significantly. Independent of density and heating power, all dominantly electron heated L-mode regimes have the common characteristic of a cross-over between electron and ion temperatures about 3-5 cm inside the separatrix. The ion temperature profile extends almost linearly towards the scrape-off layer. For strong electron heating below the L-H threshold, separatrix ion temperatures of up to 240 eV have been measured.

Transport coefficients have been determined by interpretative modeling for an ohmic case. The results are not fully conclusive, but indicate that edge ion heat transport is anomalous, although the level is not by a large factor above the neoclassical limit.

In NBI-heated L-mode plasmas, in ELMy H-mode plasmas with different densities and in quiescent, ELM-free QH-modes, edge ion temperatures were measured as well. The data agrees with core charge exchange spectroscopy measurements (different diagnostic) in the overlap region and combine with those to form a complete ion temperature profile over the whole plasma radius. In QH-mode, extremely high edge gradients of more than 600 eV/cm were found, while low power ohmic discharges show only 20 eV/cm for comparison. Absolute ion temperatures were successfully measured in a range from 50-2500 eV. This large covered range of edge parameters shows that the diagnostic system has reached a stage where it can provide the desired edge ion temperature information.

A ASDEX Upgrade

The experiment ASDEX Upgrade, where this work was conducted, is a mid-size toka-mak compared to other international tokamaks. Its operation was started 1990 as the successor of ASDEX (Axial Symetric Divertor EXperiment) where by means of addi-tional coils a poloidal divertor was firstly studied. The divertor acts to remove the outer boundary layer of the plasma (scrape-off layer) away from the hot plasma and deposits it on collector target plates. This process rids the plasma of disturbing impurities and simultaneously safeguards the wall of the plasma vessel. It achieves good thermal insu-lation of the fuel. The divertor operation enabled access to a new plasma regime, called high confinement mode (H-mode), which has better energy confinement than previously possible plasmas (now called L-mode).

ASDEX Upgrade was designed to make experiments under reactor-like conditions possi-ble. Its plasma cross-section is very similar to the shape of ITER, which is the next step
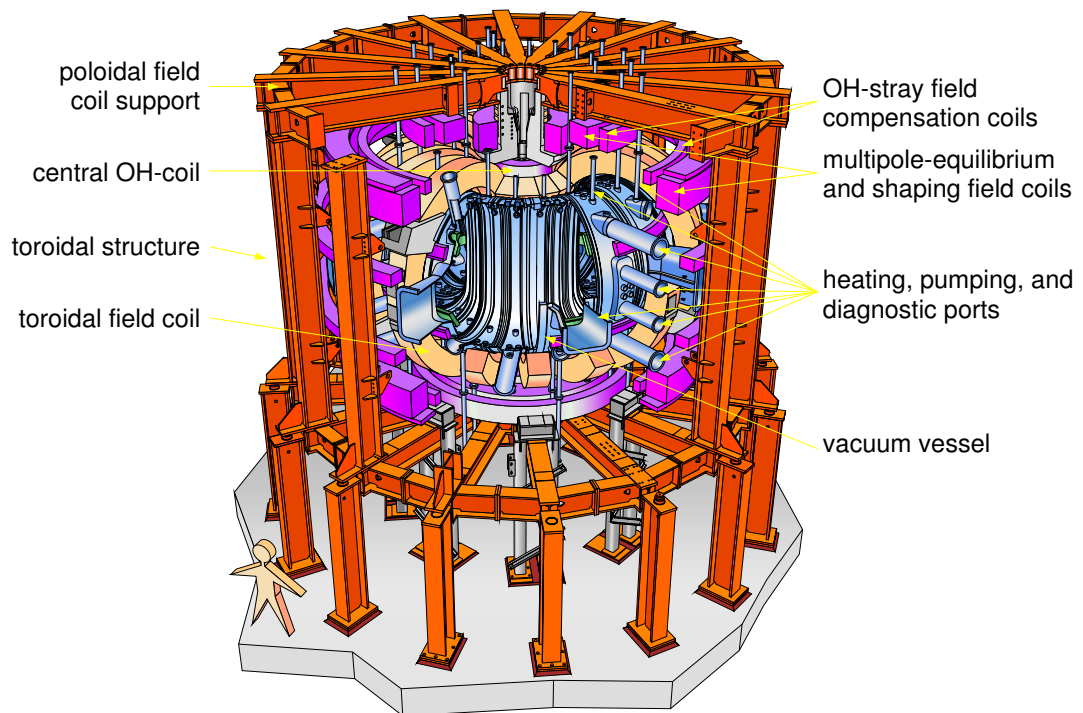
Figure A.1: 3-dimensional picture of ASDEX Upgrade displaying the structure and the most important magnetic field coils in correct proportions.

fusion experiment about to be realized by an international endeavor. Essential plasma properties, particularly the plasma density and pressure and the wall load, have been adapted in ASDEX Upgrade to the conditions that will be present in a future fusion reactor. This experiment is thus providing essential know-how for the ITER device, which is to produce the first energy-yielding plasma.

The technical specifications of the ASDEX Upgrade experiment are [6, 60]:

Total height of the experiment	9 m
Total radius over all	5 m
Weight of the experiment	800 t
First wall material	Carbon $\rightarrow$ Tungsten
Number of toroidal field coils	16
Number of poloidal field coils	12
Major/minor plasma radius	1.65 m/0.5 m
Plasma volume/surface	14 m^3/42 m^2
Plasma current	0.4 MA - 1.4 MA
Maximum magnetic field	3.9 T
Discharge duration	< 10 s
Time between pulses	15 - 20 min
Amount of data / pulse approx.	0.5 GByte
Plasma heating:	up to 27 MW
Ohmical heating	1 MW
Neutral beam injection heating	20 MW (with D)
Injection energy	60 keV and 93 keV
Ion-Cyclotron heating	6 MW (30 MHz - 120 MHz)
Electron-Cyclotron heating	4 x 0.5 MW (140 GHz)

B Abbreviations

Symbols:

a	Total minor radius of the torus, often $a = r_{separatrix}$
$a_0, \ldots, a_9$	Coefficients for the modified hyperbolic tangent fit representing T_e and n_e profiles
$A, B, C(x)$	Constants used for different purposes
A_{ij}	Transport matrix in the neoclassical transport theory
$B, \vec{B}$	Magnetic field
B_p	Poloidal magnetic field component
B_t	Toroidal magnetic field component
c	Speed of light, $c = 299\,792\,458$ m/s
D	Diffusion coefficient, used to describe the magnitude of diffusive transport
δ_{ij}	Kronecker-Delta: $\delta_{ii} = 1$, $\delta_{ij} = 0$, $\forall i \neq j$
e	Elementary charge, $e = 1.60217653 \cdot 10^{-19}$ C
$E, \vec{E}$	Electric field
ε_0	Vacuum permittivity, $\varepsilon_0 = 8.854187817 \cdot 10^{-12}$ F/m
$F(x)$	Model function for the modified hyperbolic tangent fit (in AUG-PED)
$\vec{F_L}$	Lorentz force
ζ	Electric resistivity
$\zeta_\parallel$	electric resistivity parallel to the magnetic field
$\zeta_\perp$	electric resistivity perpendicular to the magnetic field
η_i	Ratio of density gradient length and ion temperature gradient length, $\eta_i = L_n / L_{T_i}$
G_{ij}	Coefficients for excitation processes in the plasma
Γ	Particle flux (usually perpendicular to the magnetic field)
H_{ij}	Coefficients for de-excitation processes in the plasma

$I(\lambda)$	Theoretical intensity distribution in the spectrometer
I_p	Plasma current
I_{pol}	Poloidal current
$j, \vec{j}$	Current density
$\vec{J}, \mathbf{J}$	Total angular momentum of a quantum state, $\vec{J} = \vec{L} + \vec{S}$
k	Wave vector of Thomson scattering radiation
k_B	Boltzmann constant, $k_B = 1.386505 \cdot 10^{-23}$ J/K.
κ	Heat conductivity
$\kappa_\parallel$	Heat conductivity parallel to the magnetic field
$\kappa_\perp$	Heat conductivity perpendicular to the magnetic field $\kappa_\perp = n\chi$
$\vec{L}, \mathbf{L}$	Electron orbital angular momentum
L_n	Density gradient length, $L_n = \frac{n}{\nabla n}$
L_T	Temperature gradient length, $L_T = \frac{T}{\nabla T}$
$\ln \Lambda$	Coulomb-logarithm, correction factor to account for the dominant small-angle collisions in a magnetized plasmas
λ	Wavelength
λ_0	Central wavelength of a spectral line
λ_D	Debye shielding length; the plasma outside a Debye sphere ($r = \lambda_D$) appears quasi-neutral to a particle.
λ_{mfp}	Particle mean free path, distance traveled between collisions
λ_p	Penetration depth of neutral particles
m	Particle mass
m_e	Electron mass, $m_e = 9.1093826 \cdot 10^{-31}$ kg
m_i	Ion mass
μ_0	Vacuum permeability, $\mu_0 = 4\pi \cdot 10^{-7}$ N/A^2
n	Particle density (per volume)
$\overline{n}$	Line-integrated particle density (per area)
n_{cutoff}	Electron density where microwaves are reflected
n_e	Electron density
n_i	Ion density
n_{sep}	Electron density at the separatrix
ν^*	Dimensionless collisionality parameter, $\nu^* = \frac{Rq}{\tau_e v_{th}}$
p	Plasma pressure
p_e	Electron plasma pressure, $p_e = n_e T_e$
p_i	Ion plasma pressure, $p_i = n_i T_i$

P	Heating power or loss power
P_i	Incident power in Thomson scattering (YAG/YAR)
P_{heat}	Total heating power of the plasma
P_{OH}	Ohmic heating power by plasma current
$P_{rad.}$	Power lost from the plasma by radiation
P_s	Scattered power in Thomson scattering (YAG/YAR)
q	Safety factor, important for plasma stability in MHD theory
Q	Fusion gain, $Q = \frac{P_{fusion}}{P_{heat}}$
Q_e	Heat flux in the electron channel (only electron collisions)
Q_i	Heat flux in the ion channel (only ion collisions)
R	Coordinate for the major radius of the torus
r	Coordinate for the minor radius of the torus
r_e	Classical electron radius
ρ	Larmor or gyro-radius, radius of the gyrating motion of a charged particle along magnetic field line
ρ_e	Electron Larmor radius
ρ_i	Ion Larmor radius
ρ_{pol}	Normalized poloidal magnetic flux coordinate $\rho_{pol} = \sqrt{\frac{\Psi - \Psi_0}{\Psi_s - \Psi_0}}$
S	Rate coefficient for electron impact ionization
$\vec{S}, \mathbf{S}$	Electron spin angular momentum
σ	Standard deviation of an averaging process
$\sigma_{Coulomb}$	Cross section for elastic collisions
σ_{fusion}	Cross section for fusion reactions
ς	Fitted line-width of a spectral line
T	Temperature, in plasma physics usually expressed as an energy (T = E/k_B).
T_e	Electron temperature
T_i	Ion temperature
τ_c	Collision time
τ_E	Global energy confinement time
τ_e	Electron collision time
τ_{ei}	Electron-ion collision time
τ_{EX}	Heat exchange time, characteristic time scale for equilibration of two species with different temperature
τ_i	Ion collision time

τ_{ion}	Ionization time, characteristic time scale for ionization of atoms
τ_{transp}	Transport time, characteristic timescale for transport processes
Φ	Toroidal angle
χ_e	Electron heat transport coefficient ($\perp \vec{B}$)
χ_i	Ion heat transport coefficient ($\perp \vec{B}$)
U_{loop}	Toroidal voltage drop per turn due to transformer action
v_{th}	Thermal velocity of a particle: $v_{th} \propto \sqrt{T/m}$
W	Plasma stored energy
w_b	Width of the banana orbit of trapped particles
Ψ	Poloidal magnetic flux per radian
Ψ_0	Poloidal magnetic flux at the magnetic axis
Ψ_s	Poloidal magnetic flux at the separatrix
z	Vertical coordinate in cylindrical coordinate system often used for torus, height from reference plane
Z	Atomic number
Z	Charge state of ion (equal to atomic number Z for fully ionized atoms)
Z_{eff}	Effective charge of the plasma; pure hydrogen plasma: $Z_{eff} = 1$
ω_c	Electron cyclotron frequency

Chemical symbols:

C	carbon
C^{6+}	fully ionized carbon
CD_4	heavy methane
D	deuterium, a hydrogen isotope
H	hydrogen
He	helium
He^{2+}	fully ionized helium
Hg	mercury
Li	lithium
Ne	neon

Acronyms, etc.:

#	abbreviation for "shot" or discharge; every plasma discharge gets a serial number
ADAS	Atomic Data Analysis Structure, collection of programs to model plasma relevant atomic properties
ASDEX	Axial Symmetric Divertor EXperiment
ASTRA	computer code for modeling and analyzing the plasma transport in the core with a 1-dimensional fluid model
AUGPED	program for combining and fitting pedestal profiles at ASDEX Upgrade
B2	computer code for modeling the plasma edge with a 2-dimensional fluid model
CCD	Charge Coupled Device (optical detection system)
CES	Charge Exchange recombination Spectroscopy using the heating beam of NBI
CXRS	Charge eXchange Recombination Spectroscopy using a lithium beam
DCN	used as abbreviation for interferometry diagnostic (measuring line integrated electron density) using a DCN laser
ECE	Electron Cyclotron Emission, also used as an abbreviation for diagnostic measuring T_e
ECRH	Electron Cyclotron Resonance Heating
EIRENE	Monte-Carlo computer code to simulate neutral particle behavior at the plasma edge
ELM	Edge Localized Mode, burst-like edge plasma instability
ICRH	ion cyclotron resonance heating
IDL	Interactive Data Language, programming language by RSI Inc.
ITER	International Thermonuclear Experimental Reactor
JET	Joint European Torus (tokamak experiment in Culham, UK)
H-mode	plasma state with high energy confinement due to an edge transport barrier
L-mode	plasma state with reduced energy confinement due to external heating
LENA	Low Energy Neutrals Analyzer, part of diagnostic NPA
Li-IXS	Lithium beam Impact eXcitation Spectroscopy, method of measuring electron density

LID	used as an abbreviation for Li-IXS diagnostic measuring electron density
LIT	used as an abbreviation for lithium beam CXRS measuring ion temperature
MHD	magneto-hydrodynamic (theory), theory which describes a plasma as a conducting fluid
NBI	Neutral Beam Injection (plasma heating method)
NEOART	Computer code for calculation of neoclassical transport coefficients
NPA	Neutral Particle Analyzer, also used as abbreviation for diagnostic determining T_i profile from charge exchange neutrals
NUITD	Not Used In This Dissertation
QH-mode	Quiescent H-mode, high confinement plasma regime without ELMs
REF	used as an abbreviation for reflectometry diagnostic (measuring electron density)
SNR	Signal-to-Noise Ratio
SOL	Scrape-Off Layer, region of wall-intersected field lines outside the separatrix
YAG	used as abbreviation for the Thomson scattering diagnostic in the plasma center
YAR	used as abbreviation for the Thomson scattering diagnostic at the plasma edge

Diagnostic	shortcut	measuring	typical resolution
Core Charge Exchange Spec.	CES	T_i	4-5 cm, 50 ms
Core Thomson scattering	YAG	T_e, n_e	3-4 cm, 15 ns, 125 Hz
Edge Thomson scattering	YAR	T_e, n_e	< 5 mm, 15 ns, 125 Hz
Interferometry	DCN	$\overline{n_e}$	(n/a), 10 μs
Li-beam Charge eXchange	CXRS, LIT	T_i	6 mm, 200-500 ms
Li-beam Impact eXcitation spec.	IXS, LID	n_e	6 mm, 20 ms
Neutral Particle Analyzer	NPA	T_i	(full profile), 200-500 ms
Radiometry	ECE	T_e	< 5 mm, < 5 μs

Bibliography

[1] ITER-HomePage. http://www.iter.org/.

[2] J. Raeder et al. *Kontrollierte Kernfusion*. Teubner Studienbücher, Stuttgart, 1981.

[3] J. A. Wesson. *Tokamaks, 2nd Edition*. Clarendon Press, Oxford, 1997.

[4] J. Sapper and H. Renner. Stellarator Wendelstein VII-AS: physics and engineering design. *Fusion Science and Technology*, 17(Z):62–75, Jan 1990.

[5] L. Jr. Spitzer. *Physics of Fully Ionized Gases*. Interscience Publishers, New York, 1956.

[6] B. Streibl, P. T. Lang, F. Leuterer, J.-M. Noterdaeme, and A. Stäbler. Chapter 2: Machine design, fueling, and heating in ASDEX Upgrade. *Fusion Science and Technology*, 44(3):578–592, Nov 2003.

[7] J. Neuhauser, H.-S. Bosch, D. Coster, A. Herrmann, and A. Kallenbach. Chapter 8: Edge and divertor physics in ASDEX Upgrade. *Fusion Science and Technology*, 44(3):659–681, Nov 2003.

[8] F. Wagner, G. Becker, K. Behringer, D. Campbell, A. Eberhagen, W. Engelhardt, G. Fussmann, O. Gehre, J. Gernhardt, G. v. Gierke, G. Haas, M. Huang, F. Karger, M. Keilhacker, O. Klüber, M. Kornherr, K. Lackner, G. Lisitano, G. G. Lister, H. M. Mayer, D. Meisel, E. R. Müller, H. Murmann, H. Niedermeyer, W. Poschenrieder, H. Rapp, H. Röhr, F. Schneider, G. Siller, E. Speth, A. Stäbler, K. H. Steuer, G. Venus, O. Vollmer, and Z. Yü. Regime of improved confinement and high beta in neutral-beam-heated divertor discharges of the ASDEX tokamak. *Physical Review Letters*, 49(19):1408–1412, 1982.

[9] ITER Physics Basis Editors, ITER Physics Expert Group Chairs, Co-Chairs, ITER Joint Central Team, and Physics Integration Unit. Chapter 1: Overview and summary. *Nuclear Fusion*, 39(12):2137–2174, 1999.

[10] G. V. Pereverzev and O. V. Zolotukhin. Predictive simulation of ITER performance with theory-based transport models. In *Europhysics Conference Abstracts (CD-ROM, Proc. of the 30th EPS Conference on Controlled Fusion and Plasma Physics, St. Petersburg, 2003)*, volume 27B, Geneva, 2003. EPS.

[11] J. W. Connor and H. R. Wilson. A review of theories of the L-H transition. *Plasma Physics and Controlled Fusion*, 42(1):R1–R74, 2000.

[12] B. Kurzan, H. Murmann, H. Salzmann, and ASDEX Upgrade Team. Improvements in the evaluation of Thomson scattering data on ASDEX Upgrade. *Review of Scientific Instruments*, 72:1111–1114, 2001.

[13] B. B. Kadomtsev. Tokamaks and dimensional analysis. *Sov. Journal of Plasma Physics*, 1(4):295–297, 1975.

[14] ITER Physics Expert Group on Confinement, Transport, ITER Physics Expert Group on Confinement Modelling, Database, and ITER Physics Basis Editors. Chapter 2: Plasma confinement and transport. *Nuclear Fusion*, 39(12):2175–2249, 1999.

[15] G. M. Staebler. Theory of internal and edge transport barriers. *Plasma Physics and Controlled Fusion*, 40(5):569–580, 1998.

[16] J. Neuhauser, D. Coster, H. U. Fahrbach, J. C. Fuchs, G. Haas, A. Herrmann, L. Horton, M. Jakobi, A. Kallenbach, M. Laux, J. W. Kim, B. Kurzan, H. W. Müller, H. Murmann, R. Neu, V. Rohde, W. Sandmann, W. Suttrop, E. Wolfrum, and ASDEX Upgrade Team. Transport into and across the scrape-off layer in the ASDEX Upgrade divertor tokamak. *Plasma Physics and Controlled Fusion*, 44(6):855–870, 2002.

[17] A.A. Galeev and R.Z. Sagdeev. Transport phenomena in a collisionless plasma in a toroidal magnetic system. *Sov. Phys. JETP*, 26(1):233–240, 1968.

[18] R. D. Hazeltine and F. L. Hinton. Collision-dominated plasma transport in toroidal confinement systems. *Physics of Fluids*, 16(11):1883–1889, 1973.

[19] M.N. Rosenbluth, R.D. Hazeltine, and F.L. Hinton. Plasma transport in toroidal confinement devices. *Physics of Fluids*, 15(1):116–140, Jan 1972.

[20] W. Horton. Drift waves and transport. *Reviews of Modern Physics*, 71(3):735–778, April 1999.

[21] G. Tardini, A. G. Peeters, G. V. Pereverzev, F. Ryter, J. Stober, and ASDEX Upgrade Team. Comparison of theory based transport models with ASDEX Upgrade data. *Nuclear Fusion*, 42(3):258–264, 2002.

[22] K. C. Shaing and E. C. Crume. Bifurcation theory of poloidal rotation in tokamaks: A model for the L-H transition. *Physical Review Letters*, 63(21):2369–2372, 1989.

[23] Y. Andrew, N. C. Hawkes, M. G. O'Mullane, R. Sartori, M. N. A. Beurskens, I. Coffey, E. Joffrin, A. Loarte, D. C. McDonald, R. Prentice, G. Saibene, W. Suttrop, K.-D. Zastrow, and JET EFDA Contributors. Edge ion parameters at the L-H transition on JET. *Plasma Physics and Controlled Fusion*, 46(2):337–347, 2004.

[24] J. Schirmer, G.D. Conway, W. Suttrop, H. Zohm, and ASDEX Upgrade Team. Radial electric field shear and correlation length measurements in ASDEX Upgrade using correlation doppler reflectometry. In *Europhysics Conference Abstracts (Proc. of the 31st EPS Conference on Controlled Fusion and Plasma Physics, London, 2004)*, volume 28G, pages P–4.127, Imperial College, London, 2004. EPS.

[25] J. W. Connor, R. J. Hastie, H. R. Wilson, and R. L. Miller. Magnetohydrodynamic stability of tokamak edge plasmas. *Physics of Plasmas*, 5(7):2687–2700, 1998.

[26] G. Federici, A. Loarte, and G. Strohmayer. Assessment of erosion of the ITER divertor targets during type i ELMs. *Plasma Physics and Controlled Fusion*, 45(9):1523–1547, 2003.

[27] M.H. Redi, S.A. Cohen, and E.J. Synakowski. Transport simulations of helium exhaust in ITER using recent data from TFTR, TEXTOR and JT-60. *Nuclear Fusion*, 31(9):1689–1694, 1991.

[28] D. P. Coster, J.W. Kim, G. Haas, B. Kurzan, H. Murmann, J. Neuhauser, H. Salzmann, W. Schneider R. Schneider 2, J. Schweinzer, and ASDEX Upgrade Team 1. Automatic evaluation of edge transport coefficients with B2-SOLPS5.0. *Contributions to Plasma Physics*, 40(3-4):334–339, 2000.

[29] J. W. Connor and H. R. Wilson. A review of theories of the L-H transition. *Plasma Physics and Controlled Fusion*, 42(1):R1–R74, 20008.

[30] H. Murmann, S. Gotsch, H. Rohr, H. Salzmann, and K. H. Steuer. The thomson scattering systems of the ASDEX Upgrade tokamak. In *Review of Scientific Instruments*, volume 63, pages 4941–4943. AIP, 1992.

[31] W. Suttrop, A. G. Peeters, ASDEX Upgrade Team, and NBI Group. Practical limitations to plasma edge electron temperature measurements by radiometry of electron cyclotron emission. Technical Report 1/306, IPP, Garching, Germany, December 1996.

[32] I. H. Hutchinson. *Principles of Plasma Diagnostics: Second Edition*. Cambridge Universtiy Press, Cambridge, 2002.

[33] J. Schweinzer, E. Wolfrum, F. Aumayr, M. Pockl, H. Winter, R. P. Schorn, E. Hintz, and A. Unterreiter. Reconstruction of plasma edge density profiles from Li I (2s-2p) emission profiles. *Plasma Physics and Controlled Fusion*, 34(7):1173–1183, 1992.

[34] H. Verbeek. A low-energy neutral particle analyser for plasma experiments. *Journal of Physics E: Scientific Instruments*, 19(11):964–970, 1986.

[35] Reiter D. et al. The EIRENE code. see http://www.eirene.de/, 1992.

[36] J. Stober, D. P. Coster, H.-U. Fahrbach, G. Haas, W. Herrmann, O. Kardaun, A. Khutoretsky, S. de Peña Hempel, D. Reiter, R. Schneider, H. Verbeek, ASDEX Upgrade Team, and NBI Team. Profiles of ion temperature and neutral density from the simulation of charge exchange measurements and additional experimental data. In D. Gresillon, A. Sitenko, and A. Zagorodony, editors, *Europhysics Conference Abstracts (Proc. of the 23rd EPS Conference on Controlled Fusion and Plasma Physics, Kiev, 1996)*, volume 20C, part III, pages 1023–1026, Geneva, 1996. EPS.

[37] P. J. Mc Carthy. Analytical solutions to the grad–shafranov equation for tokamak equilibrium with dissimilar source functions. *Physics of Plasmas*, 6(9):3554–3560, 1999.

[38] R.J. Groebner, D.R. Baker, K.H. Burrell, T.N. Carlstrom, J.R. Ferron, P. Gohil, L.L. Lao, T.H. Osborne, D.M. Thomas, W.P. West, J.A. Boedo, R.A. Moyer, G.R. McKee, R.D. Deranian, E.J. Doyle, C.L. Rettig, T.L. Rhodes, and J.C. Rost. Progress in quantifying the edge physics of the H-mode regime in DIII-D. *Nuclear Fusion*, 41(12):1789–1802, 2001.

[39] R.C. Isler. An overview of charge-exchange spectroscopy as a plasma diagnostic. *Plasma Physics and Controlled Fusion*, 36:171–208, 1994.

[40] R. Neu, R. Pugno, V. Rohde, R. Dux, T. Eich, Fahrbach H. U., A. Geier, A. Herrmann, D. Hildebrandt, A. Kallenbach, P. Lang, C. Maggi, T. Pütterich, F. Ryter, W. Schneider, U. Seidel, and ASDEX Upgrade Team. Assessment of intrinsic impurity behaviour in ASDEX Upgrade. In *Europhysics Conference Abstracts (CD-ROM, Proc. of the 30th EPS Conference on Controlled Fusion and Plasma Physics, St. Petersburg, 2003)*, volume 27B, Geneva, 2003. EPS.

[41] J. Schweinzer, D. Wutte, and H. P. Winter. A study of electron capture and excitation processes in collisions of multiply charged ions with lithium atoms. *Journal of Physics B: Atomic, Molecular and Optical Physics*, 27(1):137–153, 1994.

[42] R. Dux. Chapter 11: Impurity transport in ASDEX Upgrade. *Fusion Science and Technology*, 44(3):708–715, Nov 2003.

[43] H. P. Summers. Atomic data and analysis structure users manual. *Atomic data and analysis structure users manual, JET-IR(93) 07 (Abingdon: JET Joint Undertaking)*, 1993.

[44] S. Fiedler, R. Brandenburg, J. Baldzuhn, K. McCormick, F. Aumayr, J. Schweinzer, H. P. Winter, W7-AS Team, and ASDEX Upgrade Team. Edge plasma diagnostics on W7-AS and ASDEX Upgrade using fast Li-beams. *Journal of Nuclear Materials*, 266–269:1279–1284, 1999.

[45] H. Ehmler, J. Baldzuhn, K. McCormick, A. Kreter, T. Klinger, and W7-AS Team. Charge-exchange spectroscopy at the W7-AS stellarator employing a high-energy Li beam. *Plasma Physics and Controlled Fusion*, 45:53–62, 2003.

[46] J. D. Hey, Y. T. Lie, D. Rusbüldt, and E. Hintz. Doppler broadening and magnetic field effects on some ion impurity spectra in the boundary layer of a tokamak plasma. *Contrib. Plasma Phys.*, 34(6):725–747, 1994.

[47] J. D. Hey, C. C. Chu, and Ph. Mertens. Zeeman spectroscopy as a tool for studying atomic processes in edge plasmas. *Contrib. Plasma Physics*, 42:635–644, 2002.

[48] R. Dux and A. G. Peeters. Neoclassical impurity transport in the core of an ignited tokamak plasma. *Nuclear Fusion*, 40(10):1721–1729, 2000.

[49] T. Eich, A. Herrmann, and J. Neuhauser ASDEX Upgrade Team. Nonaxisymmetric energy deposition pattern on ASDEX Upgrade divertor target plates during type-I Edge-Localized Modes. *Physical Review Letters*, 91(19):195003, 2003.

[50] H. Urano, W. Suttrop, L.D. Horton, A. Herrmann, J.C. Fuchs, and ASDEX Upgrade Team. Energy and particle losses during type-I ELMy H-mode in ASDEX Upgrade. *Plasma Physics and Controlled Fusion*, 45:1571–1596, 2003.

[51] C. Angioni, A.G. Peeters, X. Garbet, A. Manini, F. Ryter, and ASDEX Upgrade Team. Density response to central electron heating: theoretical investigations and experimental observations in ASDEX Upgrade. *Nuclear Fusion*, 44(8):827–845, 2004.

[52] K. H. Burrell, M. E. Austin, D. P. Brennan, J. C. DeBoo, E. J. Doyle, P. Gohil, C. M. Greenfield, R. J. Groebner, L. L. Lao, T. C. Luce, M. A. Makowski, G. R. McKee, R. A. Moyer, T. H. Osborne, M. Porkolab, T. L. Rhodes, J. C. Rost, M. J. Schaffer, B. W. Stallard, E. J. Strait, M. R. Wade, G. Wang, J. G. Watkins, W. P. West, and L. Zeng. Quiescent H-mode plasmas in the DIII-D tokamak. *Plasma Physics and Controlled Fusion*, 44(5A):A253–A263, 2002.

[53] W. Suttrop, M. Maraschek, G. D. Conway, H.-U. Fahrbach, G. Haas, L. D. Horton, T. Kurki-Suonio, C. J. Lasnier, A. W. Leonard, C. F. Maggi, H. Meister,

A. Mück, R. Neu, I. Nunes, Th. Pütterich, M. Reich, A. C. C. Sips, and ASDEX Upgrade Team. ELM-free stationary h-mode plasma in the ASDEX Upgrade tokamak. *Plasma Physics and Controlled Fusion*, 45(8):1399–1416, 2003.

[54] G. Pereverzev and P. N. Yushmanov. ASTRA automated system for TRansport analysis in a tokamak. IPP Report Nr. 5/98, Max-Planck-Institut für Plasmaphysik, February 2002.

[55] G. V. Pereverzev, S. Günter, A. G. Peeters, R. C. Wolf, and ASDEX Upgrade Team. Transport modelling of ASDEX Upgrade plasma with internal transport barrier. In K. Szegö, T. N. Todd, and S. Zoletnik, editors, *Europhysics Conference Abstracts (CD-ROM), Proc. of the 27th EPS Conference on Controlled Fusion and Plasma Physics, Budapest, 2000*, volume 24B, pages 1020–1023, Geneva, 2001. EPS.

[56] R. Dux and A.G. Peeters. Neoclassical impurity transport in the core of an ignited tokamak plasma. *Nuclear Fusion*, 40(10):1721–1729, 2000.

[57] C. S. Chang and F. L. Hinton. Effect of finite aspect ratio on the neoclassical ion thermal conductivity in the banana regime. *Physics of Fluids*, 25(9):1493–1494, 1982.

[58] C. S. Chang and F. L. Hinton. Effect of impurity particles on the finite-aspect ratio neoclassical ion thermal conductivity in a tokamak. *Physics of Fluids*, 29(10):3314–3316, 1986.

[59] A. Bergmann, A. G. Peeters, and S. D. Pinches. Monte carlo delta-f simulation of wide-orbit neoclassical transport. In K. Szegö, T. N. Todd, and S. Zoletnik, editors, *Europhysics Conference Abstracts (CD-ROM, Proc. of the 27th EPS Conference on Controlled Fusion and Plasma Physics, Budapest, 2000)*, volume 24B, pages 1140–1143, Geneva, 2001. EPS.

[60] IPP-Homepage. http://www.ipp.mpg.de/eng/for/projekte/asdex/.

Danksagung

An dieser Stelle möchte ich allen Leuten, die mir im Verlauf dieser Arbeit auf verschiedenste Weise geholfen haben, meinen Dank aussprechen. Die Arbeit an einem Großforschungsprojekt mit so einem tollen Team macht sehr viel Spaß und ich danke allen, die zu der sehr kollegialen Atmosphäre in Garching beigetragen haben und immer noch beitragen.

Zum Team „ASDEX Upgrade" gehören auch mein Doktorvater, Prof. H. Zohm, sowie mein Bereichsleiter, Prof. M. Kaufmann, denen ich an dieser Stelle für die Ermöglichung dieser Promotion ganz herzlich danken möchte. H. Zohm half mir insbesondere bei der Organisation wissenschaftlicher Präsentationen inklusive dieser Dissertation mit stets nützlichen Anregungen und Hinweisen.

Ebenfalls herzlicher Dank gebührt meiner Betreuerin Dr. E. Wolfrum, die im Hintergrund stets für optimale Arbeitsbedingungen in der Lithiumstrahl-Gruppe sorgte. Ihr großes Vertrauen, das sie mir entgegenbrachte, ermöglichte es mir, die vorliegende Arbeit über weite Teile eigenverantwortlich wissenschaftlich zu gestalten. Trotz zweier Schwangerschaften während der dreijährigen Arbeit war sie dennoch jederzeit erreichbar und hatte bei Fragen oder Problemen immer eine Lösung parat.

Ohne die zahlreichen anregenden Diskussionen mit meinem Gruppenleiter Dr. J. Neuhauser, die dank gelegentlichen Ausschweifens teamweit berühmt sind, wäre mein physikalisches Verständnis für die Plasmaphysik nur mit deutlich höherem Aufwand so weit gediehen. Ich bin ihm für diese Bereicherung zu außerordentlich großem Dank verpflichtet. Ferner war sein intensives Korrekturlesen der Arbeit als Ganzem und in Detailaspekten sehr zuträglich.

Vielen Dank auch Dr. J. Schweinzer, der mir als Experte für Fragen bezüglich der Lithiumstrahl-Diagnostik jederzeit ein offenes Ohr schenkte. Seine große Erfahrung auch bei physikalischen Fragen half sehr dabei, Probleme rasch zu beseitigen und die Ionentemperaturmessungen nicht durch technische Unzulänglichkeiten unnötig zu behindern.

Für die fruchtbaren Diskussionen über die physikalischen und technischen Aspekte der Diagnostik möchte ich — neben allen bereits erwähnten Personen — auch besonders Dr. L. Horton meinen Dank aussprechen, der sowohl durch sein Programm (AUGPED) als

Lebenslauf

Persönliche Daten

Matthias Reich

Geb. am 09. 06. 1975 in Hirschau
Ledig, deutsch

Tel.: (0178) 5 01 07 09
E-Mail: email@matthias-reich.de

Schulbildung

08/1981–07/1985   Grundschule in Kümmersbruck

08/1985–06/1994   Gymnasium in Amberg (Leistungskurse Mathematik und Physik)

Wehrdienst

07/1994–06/1995   Kraftfahrer des Pionierbataillon in Bogen

Studium

10/1995–10/2001   Studium der Physik an der Universität Regensburg mit Abschluss Diplom

08/1998–09/1999   Integriertes Auslandsstudium und „Academic training" an der UIUC in Champaign-Urbana, Illinois, USA

11/2000–10/2001   Diplomarbeit am Max-Planck-Institut für Plasmaphysik in Garching bei München

Berufserfahrung

seit 01/2002   Max-Planck-Institut für Plasmaphysik, Garching bei München

Promotion mit dem Thema „A new diagnostic for ASDEX Upgrade edge ion temperatures by lithium-beam charge exchange recombination spectroscopy".

Sonstiges

09/2001–10/2001   Mitarbeit beim geophysikalischen Forschungsprojekt Hi-CLIMB („An Integrated Study of the Himalayan-Tibetan Continental Lithosphere during Mountain Building") in Nepal

München, 22. Dezember 2004